

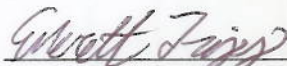
# Interferometric Optical Readout System For a MEMS Infrared Imaging Detector

A Thesis  
submitted to the faculty of the

**Worcester Polytechnic Institute**

as a partial fulfillment of the requirements for the  
Degree of Master of Science  
in  
Mechanical Engineering

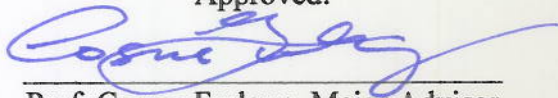
By



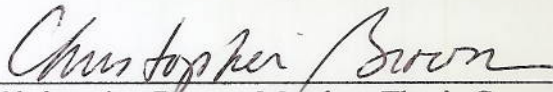
Everett R. Tripp

5 April 2012

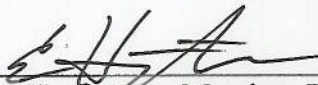
Approved:



Prof. Cosme Furlong, Major Advisor



Prof. Christopher Brown, Member, Thesis Committee



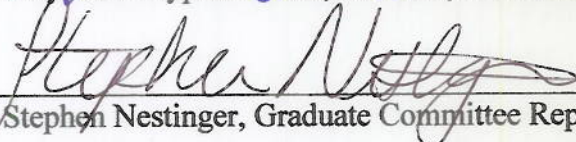
Ellery Harrington, Member, Thesis Committee



Dr. Francis Pantuso, Agiltron, Inc., Woburn, MA, Member, Thesis Committee



Prof. Ryszard Pryputniewicz, Member, Thesis Committee



Prof. Stephen Nestinger, Graduate Committee Representative

# **Interferometric Optical Readout System For a MEMS Infrared Imaging Detector**

A Thesis  
submitted to the faculty of the

**Worcester Polytechnic Institute**

as a partial fulfillment of the requirements for the  
Degree of Master of Science  
in  
Mechanical Engineering

By

---

Everett R. Tripp

5 April 2012

Approved:

---

Prof. Cosme Furlong, Major Advisor

---

Prof. Christopher Brown, Member, Thesis Committee

---

Ellery Harrington, Member, Thesis Committee

---

Dr. Francis Pantuso, Agiltron, Inc., Woburn, MA, Member, Thesis Committee

---

Prof. Ryszard Pryputniewicz, Member, Thesis Committee

---

Prof. Stephen Nestinger, Graduate Committee Representative

Copyright © 2012

By

NEST – NanoEngineering, Science and Technology

CHSLT – Center for Holographic Studies and Laser micro-mechaTronics

Mechanical Engineering Department

Worcester Polytechnic Institute

Worcester, MA 01609-2280

All rights reserved

## **Abstract**

MEMS technology has led to the development of new uncooled infrared imaging detectors. One type of these MEMS detectors consist of arrays of bi-metallic photomechanical pixels that tilt as a function of temperature associated with infrared radiation from the scene. The main advantage of these detectors is the optical readout system that measures the tilt of the beams based on the intensity of the reflected light. This removes the need for electronic readout at each of the sensing elements and reduces the fabrication cost and complexity of sensor design, as well as eliminates the electronic noise at the detector. The optical readout accuracy is sensitive to the uniformity of individual pixels on the array. The hypothesis of the present research is that direct measurements of the height change corresponding to tilt through holographic interferometry will reduce the need for high pixel uniformity. Measurements of displacements for a vacuum packaged detector with nominal responsivity of 2.4nm/K are made with a Linnik interferometer employing the four phase step technique. The interferometer can measure real-time, full-field height variations across the array. In double-exposure mode, the current height map is subtracted from a reference image so that the change in deflection is measured. A software algorithm locates each mirror on the array, extracts the measured deflection at the tip of a mirror, and uses that measurement to form a pixel of a thermogram in real-time. A blackbody target projector with temperature controllable to 0.001K is used to test the thermal resolution of the imaging system. The achieved minimum temperature resolution is better than 0.25K. The double exposure technique removes mirror non-uniformity as a source of noise. A lower

than nominal measured responsivity of around 1.5nm/K combined with noise from the measurements made with the interferometric optical readout system limit the potential minimum temperature resolution. Improvements need to be made both in the holographic setup and in the MEMS detector to achieve the target temperature resolution of 0.10K.

## **Acknowledgments**

I would like to thank my advisor Professor Cosme Furlong for giving me the opportunity to do my thesis on such an exciting area of research and for the guidance he has provided along the way. The project would not have made it as far as it did without the help of all the members of the Center for Holographic Studies and Laser micro-Mechatronics. I would like to particularly thank Ellery Harrington for his software development that has proven critical for the success of this project and Peter Hefti for his assistance with the optical systems. Both of them provided help and guidance at every step of my work. Finally, I would also like to thank Dr. Frank Pantuso and Dr. Lei Zhang of Agiltron Incorporated not only for sponsoring this project, but for also providing valuable feedback and ideas throughout the process.

# Table of Contents

Abstract .....	i
Acknowledgments.....	iii
Table of Contents .....	iv
List of Figures .....	viii
List of Tables .....	xv
Nomenclature .....	xvii
1 Infrared Imaging Technology .....	1
1.1 Principles of Infrared Imaging .....	1
1.2 Applications and Markets for Infrared Imaging.....	6
1.3 Infrared Imager Principles of Operation .....	7
1.4 Evaluation of Infrared Imaging Systems.....	8
1.5 Lenses.....	9
1.6 Types of Infrared Detectors.....	10
1.6.1 Photonic Infrared Detectors .....	10
1.6.2 Photothermal Infrared Detectors .....	12
1.6.3 Optomechanical Infrared Detectors .....	13
2 Optomechanical Infrared Detectors with Interferometric Optical Readout.....	21
2.1 Interferometry.....	24
2.1.1 Principles of Michelson Interferometry .....	25
2.1.2 Phase Stepping to Improve Interferometry .....	31

2.2	Vacuum Seal and Compensation.....	35
2.3	Previous Work.....	36
2.4	Goals.....	37
3	Verification of Compensation Window Effectiveness .....	38
3.1	Experimental Setup for Verification of the Compensation Window .....	38
3.2	Results for Compensation Window Effectiveness .....	40
3.3	Conclusions of Tests for Compensation Window Effectiveness .....	42
4	Demonstration of Accuracy and Repeatability in PSI .....	43
4.1	Parameters Affecting Accuracy and Repeatability in PSI .....	43
4.1.1	Image Acquisition .....	43
4.1.2	Phase-Step Calibration .....	47
4.1.3	Illumination Characteristics .....	50
4.1.4	Consistency of Illumination and Observation Conditions .....	50
4.2	Detector Noise.....	51
4.3	Experimental Procedure for Verification of Accuracy in PSI.....	51
4.4	Accuracy Results.....	54
4.5	Repeatability Results.....	56
4.6	Conclusions of the accuracy and repeatability measurements .....	61
5	The Interferometric Optical Readout System .....	63
5.1	Experimental Setup Constraints .....	64
5.2	Interferometer.....	65

5.2.1	Microscope Objectives .....	66
5.2.2	Illumination Source .....	66
5.2.3	Piezo-Electric Transducer .....	66
5.2.4	Compensation Window .....	67
5.2.5	Cameras .....	68
5.3	Assembled Infrared Imaging System .....	68
5.4	LaserView Software .....	69
5.5	Demonstration of Real-Time Displacement Measurements .....	75
6	Algorithm for Real-Time Infrared Imaging .....	77
6.1	Algorithm Description .....	77
6.2	Demonstration of Real-Time Infrared Imaging Abilities .....	85
6.3	Conclusions of the Real-Time Imaging Demonstrations .....	92
7	Evaluation of System Performance .....	93
7.1	The Blackbody Target Projector .....	93
7.2	Procedure for Calculating Noise and NEDT .....	97
7.3	Noise Results from Optical Flat Measurements .....	100
7.4	Noise Results for Measurements without Thermal Loading .....	102
7.5	NEDT Results .....	106
7.6	Conclusions from Noise and NEDT Characterizations of the System..	109
8	Alternative Imaging Algorithm .....	111
8.1	Description of the Alternative Imaging Algorithm .....	111

8.2	Alternative Algorithm Results .....	112
8.3	Alternative Algorithm Conclusions .....	119
9	Conclusions and Recommendations for Future Work .....	121
10	References .....	126
	Appendix A: MATLAB code for Infrared Imaging Algorithm .....	129
	Appendix B: 3D Noise Calculations .....	130
	Appendix C: Alternative Algorithm MATLAB Code .....	135

## List of Figures

Figure 1.1. The electromagnetic spectrum.....	2
Figure 1.2. Plot of Planck’s Law of Blackbody Radiation. ....	4
Figure 1.3. Example of a thermogram. ....	5
Figure 1.4. Diagram of the components in an infrared imaging system.....	7
Figure 1.5. MEMS bimetallic cantilever manufacturing process (Dobrev et al., 2009)...	15
Figure 1.6. Bi-metallic photomechanical pixel with thermal isolator (Erdtmann et al., 2010). ....	18
Figure 2.1. Deviations from the ideal pixels impact the uniformity of the intensity of reflected light; this lowers the spatial consistency of the measurements of the array (Erdtmann et al., 2010). ....	21
Figure 2.2. The packaged MEMS device.....	22
Figure 2.3. Microscopic view of individual mirror components. ....	23
Figure 2.4. Interference of wavefronts: (a) out-of phase waves interfering destructively; and (b) in-phase waves interfering constructively .....	25
Figure 2.5. Michelson interferometer. ....	26
Figure 2.6. Relationship between optical phase and fringe intensity .....	28
Figure 2.7. Parallel illumination and observation conditions. ....	30
Figure 2.8. Synchronization in time between (a) camera shutter signal and (b) piezo- electric positioner signal. ....	34
Figure 2.9. Phase-stepping interferometry system.....	35
Figure 3.1. Michelson interferometer with compensation window. ....	39

Figure 3.2. Compensation window and reference mirror. ....	40
Figure 3.3. Interferogram of a $10 \times 8 \text{mm}^2$ section of the array. ....	40
Figure 3.4. Height map of detector substrate showing the saddle-like shape .....	41
Figure 4.1. Spatial median filtering on a $3 \times 3$ kernel, before and after the application of a low-pass filter.....	45
Figure 4.2. Three frame temporal averaging of pixel intensities in an image region; the resultant values for each pixel are the arithmetic averages of each of the corresponding pixels. ....	46
Figure 4.3. Hysteresis error in the positioner as shown by the difference between the ideal and actual response in the displacement versus signal curve. ....	48
Figure 4.4. NIST traceable calibration standard as used to verify the accuracy and uncertainty of measurements made with PSI .....	52
Figure 4.5. Microscope modified for phase-stepping interferometry. ....	53
Figure 4.6. Height map of the 100nm calibration standard step with out-of-plane height in nm. ....	55
Figure 4.7. Histogram of the height map of the 100nm calibration standard showing a step height of $98.8 \text{nm} \pm 1.2 \text{nm}$ . ....	56
Figure 4.8. Results of a height measurement of a flat section of the calibration standard with no averaging (a) height map; and (b) the image histogram with standard deviation of $1.22 \text{nm}$ . ....	57

Figure 4.9. Results of a height measurement of a flat section of the calibration standard with 5 averages per phase step (a) height map; and (b) the image histogram with standard deviation of 1.19nm.....	58
Figure 4.10. Results of a height measurement of a flat section of the calibration standard with 5 averages per phase step and the shape of the surface filtered out; (a) height map; and (b) the image histogram with standard deviation of 0.16nm. ....	59
Figure 5.1. MEMS detector installed in a custom LWIR lens.....	63
Figure 5.2. The Linnik interferometer used in the optical readout system. ....	65
Figure 5.3. The compensation window mount: (a) the custom machined mount; and (b) the mount inserted between the objective and reference mirror. ....	67
Figure 5.4. The complete infrared imaging system showing the configuration of the individual components. ....	69
Figure 5.5. View selection window in LaserView.....	70
Figure 5.6. Interferogram of a 1.9×1.9mm <sup>2</sup> section of the MEMS array as displayed in LaserView with a close-up view to show the formation of fringes only on the mirror surfaces. ....	70
Figure 5.7. Modulation image of a 1.9×1.9mm <sup>2</sup> section of the MEMS array as displayed in LaserView with a close-up view to show the peak modulation occurring only on the mirror surfaces. ....	71
Figure 5.8. Phase map of a 1.9×1.9mm <sup>2</sup> section of the MEMS array as displayed in LaserView with the deformation of the substrate visible. The close-up shown the optical phase patterns across individual mirrors.....	72

Figure 5.9. Double exposed phase map of a $1.9 \times 1.9 \text{mm}^2$ section of the MEMS array as displayed in LaserView with a reference phase map and no loading. The close-up shows the flat phase of the mirrors and the random phase on sections with no modulation .....	73
Figure 5.10. Image export in LaserView with RTI as the selected image format. ....	74
Figure 5.11. LaserView camera and phase-shifter control. ....	75
Figure 5.12. Double exposed phase map showing mirror displacements from soldering iron heat input. ....	76
Figure 6.1. Response of a single mirror: (a) Optical phase map of a single mirror from a change in thermal load corresponding to approximately 15K; and (b) a plot of the optical phase values of a cross-section of the phase map showing the tilt of the mirror. The base of the mirror is on the right and the tip of the mirror is on the left where maximum displacement is observed .....	78
Figure 6.2. Flow diagram of image processing starting with image acquisition of 4 phase-stepped interferograms, to the calculation of the phase map and modulation image through LaserView and finally through the creation of real-time infrared images based on data calculated in LaserView. ....	79
Figure 6.3. Automatic mirror detection with algorithm: (a) modulation of the mirror array as calculated by LaserView; (b) the modulation threshold parameters as set in LaserView; and (c) the location of the mirrors as determined by the algorithm. .	80
Figure 6.4. Measurements of a mirror with $17 \times 6$ pixels; the value associated with the mirror is the median value of a $3 \times 3$ section located a distance of 7 pixels to the	

right of the centroid. The number of pixels used in the measurement is set by the optical magnification of the system .....	81
Figure 6.5. The single median value calculated for each mirror is placed at a position corresponding to that mirror's calculated centroid. ....	82
Figure 6.6. A representative thermogram of a finger as produced by the imaging algorithm with the total number of pixels reduced to remove the gaps between known pixels. ....	83
Figure 6.7. A representative thermogram of a finger as produced by the imaging algorithm that has been filtered to remove all gaps. ....	83
Figure 6.8. The complete LaserView infrared imaging user interface; the thermogram displays at the center of the window. ....	85
Figure 6.9. Real-time thermograms of an arm showing similar relative temperature distributions (a) as produced by the interferometric readout; and (b) the FLIR camera with a temperature difference of around 20K between the skin and sleeve as measured by the FLIR camera. ....	87
Figure 6.10. Real-time thermograms of a shirt (a) as produced by the interferometric readout and (b) the FLIR camera with temperature difference of 5K between the shirt and the hand prints. ....	88
Figure 6.11. Real-time thermograms of portraits (a) as produced by the interferometric readout; and (b) the FLIR Camera with temperature difference of around 0.6K between the skin and eyes as measured by the FLIR. ....	89

Figure 6.12. Thermogram of wrist watch as produced by the interferometric readout system demonstrating its ability to show small details through measured temperature distributions .....	90
Figure 6.13. Thermogram of three fingers and fingernails with temperature differential of on the order of 0.4K between the skin and nails.....	91
Figure 7.1. Diagram of the blackbody projector components (Santa Barbara Infrared, 1999). .....	94
Figure 7.2. The imaging system focused on the blackbody target.....	94
Figure 7.3. The blackbody target at 25.00°C as viewed with the FLIR A325 showing consistency between the value measured by the FLIR and the blackbody controller. ....	95
Figure 7.4. Thermograms of blackbody target at known temperature differentials to characterize the measurement resolution: (a) the target is well defined with temperature change of 1K; and (b) the target is visible but more difficult to discern from the background with a temperature change of 0.3K.....	96
Figure 7.5. Image data cube with vertical and horizontal spatial dimensions and a temporal dimension.....	97
Figure 7.6. Temporal noise as calculated from a data cube by taking the standard deviation at each spatial location across time. ....	98
Figure 7.7. Spatial noise as calculated from a data cube by taking the standard deviation of each spatially uniform frame in time.....	99

Figure 7.8. Readout system with optical flat in place of the MEMS detector for characterization of temporal and spatial noise of the optical readout system.....	101
Figure 8.1. The linear fit of the measured double exposed optical phase values across a tilted mirror with a slope of 0.011 rad/pixel and a correlation coefficient of 0.97 demonstrating the linearity .....	113
Figure 8.2. Histogram showing the distribution of correlation coefficients for linear regressions of slope of each mirror in the array demonstrating that the slope of the mirrors is consistently linear. ....	113
Figure 8.3. Linear fit to measured phase across a mirror with outlier phase values that skew the linear regression so that the slope is 0.010 rad/pixel instead of 0.011rad/pixel .....	114
Figure 8.4. The optical phase across a single pixel for uniform scene temperature of 25°C with a slope of 0.0047rad/pixel.....	117
Figure 8.5. The optical phase across a single mirror for uniform scene temperature of 35°C with a slope of 0.0136rad/pixel. ....	117

## List of Tables

Table 4.1. Cameras utilized for verification of accuracy and uncertainty in PSI.....	54
Table 4.2. Uncertainty results from PSI measurements with PLA741 camera. ....	60
Table 4.3. Uncertainty results from PSI measurements with F100B camera. ....	60
Table 4.4. Uncertainty results from PSI measurements with F505B camera. ....	60
Table 4.5. Uncertainty results for PSI measurements with the F033B camera. ....	61
Table 6.1. Comparison of the FLIR A325 to the imaging system with Pike F100. ....	86
Table 7.1. 3D noise components of a data cube used to identify potential sources of noise. .....	100
Table 7.2. 3D noise components of the optical readout system as calculated from holographic measurements of an optical flat. ....	102
Table 7.3. 3D noise measurements as calculated from a data cube of thermograms produced by the algorithm with a single value offset 6 pixels from the centroid representing each mirror and no thermal-loading after the capture of the reference phase map.....	103
Table 7.4. 3D noise measurements as calculated from a data cube of thermograms produced by the imaging algorithm with the median value of a 3×3 region offset 6 pixels from the centroid representing each mirror and no thermal loading after the capture of the reference phase map.....	104
Table 7.5. 3D noise measurements as calculated from a data cube of thermograms produced by the imaging algorithm with the median of a 5×5 region offset 6	

pixels from the centroid representing each mirror in the array and no thermal loading after the capture of the reference image.....	105
Table 7.6. NEDT results as calculated from data cubes of thermograms produced by the imaging algorithm for uniform thermal loading of 20°C, 21°C and 22°C. ....	106
Table 7.7. NEDT results as calculated from data cubes of thermograms produced by imaging algorithm for uniform thermal loading of 25°C, 30°C and 35°C. ....	108
Table 8.1. 3D noise results as calculated from a data cube of thermograms of a uniform scene of a human hand using the mirror slope algorithm .....	115
Table 8.2. 3D noise results as calculated from a data cube of thermograms of a uniform scene at room temperature using the mirror slope algorithm. ....	116
Table 8.3. NEDT results for data cubes of thermograms of uniform scenes at 25°C, 30°C, and 35°C using the mirror slope algorithm and no temporal averaging. ....	118
Table 8.4. NEDT results for data cubes of thermograms of uniform scenes at 25°C, 30°C, and 35°C using the mirror slope algorithm and 4 frames average per phase step. ....	119

## Nomenclature

IR	Infrared
$d\Omega$	Solid Angle
$\Phi$	Radiant Flux
L	Radiance
$da$	Surface area from which radiation is emitted
$\lambda$	Wavelength of radiation
$T$	Temperature
$h$	Universal Planck constant
$k$	Universal Boltzmann constant
$c_o$	Speed of light in a vacuum
FPA	Focal Plane Array
NEDT	Noise Equivalent Differential Temperature
$\beta$	Thermal multiplier
$F$	Focal ratio of lens
$B_\lambda$	Spectral band factor
$R_{thr}$	Thermal radiation resistance
$R_c$	Thermal resistance of detector
$U_r$	Displacement of reference wavefront
$A_r$	Amplitude of the reference wavefront
$\phi_1$	Phase of the reference wavefront
$\omega$	Angular frequency of wavefronts
$U_o$	Displacement of object wavefront
$A_o$	Amplitude of the object wavefront
$\phi_1$	Phase of the object wavefront
$U$	Displacement of superimposed wavefronts
$I$	Resultant intensity of superimposed wavefronts

$I_r$	Intensity of reference wavefront
$I_o$	Intensity of object wavefront
$V$	Fringe Contrast
$\Omega$	Fringe-Locus Function
$\mathbf{K}$	Sensitivity vector
$\mathbf{K}_2$	Observation vector
$\mathbf{K}_1$	Illumination vector
$K$	Wavenumber
$\mathbf{D}$	Displacement vector
$i, j, k$	Unit vectors
$D_x, D_y, D_z$	Magnitudes of displacement
$I_1, I_2, I_3, I_4$	Resultant intensities at known phase steps
PSI	Phase-Stepping Interferometry
$\gamma$	Modulation
$\alpha$	Calibration phase step

# **1 Infrared Imaging Technology**

The ability to form images from infrared radiation (IR) has applications ranging from military and security to astronomy and geology. Infrared imaging systems provide accurate, non-contact temperature measurements. Numerous detector types exist for meeting the needs of these varied applications. Detectors can be grouped into two broad categories: photonic and thermal. Each has its own set of advantages and disadvantages. The development of new detector types is a response to these disadvantages. The optomechanical MEMS detector is a relatively new technology that has the potential to overcome some of the cost and noise limitations of current detectors for high resolution thermal imaging. This type of detector consists of an array of bimetallic beams that deflect as a function of temperature associated with infrared radiation at the scene. The intensity of light reflected off of tilting mirrors attached to the beams corresponds to the amount of deflection. This light intensity is measured by a single CCD camera. Limitations in manufacturing quality, however, lead to nonuniformity and inconsistent reflections across the array. The goal of the present research is to overcome these limitations through the use of an interferometric optical readout system that holographically measures the height change associated with the mirror tilt.

## **1.1 Principles of Infrared Imaging**

James Maxwell brought together Gauss's Law for Electric Fields, Gauss's Law for Magnetic Fields, Ampere's Law relating magnetic fields to electric currents and

Faraday's Law of induction into what has become known as Maxwell's equations. Maxwell concluded that when either an electric or a magnetic field is changing with time, a field of the other type is also induced. Because the electric and magnetic fields are time-varying, the disturbances exhibit wave-like behavior. Such waves will have the same properties as mechanical waves including amplitude, wavelength, and frequency. These disturbances radiate away from the source and are known as electromagnetic radiation. Electromagnetic waves are comprised of small packets of energy called photons (Young and Freedman, 2008). Electromagnetic waves can have many different wavelengths across the Electromagnetic Spectrum as shown in Figure 1.1.

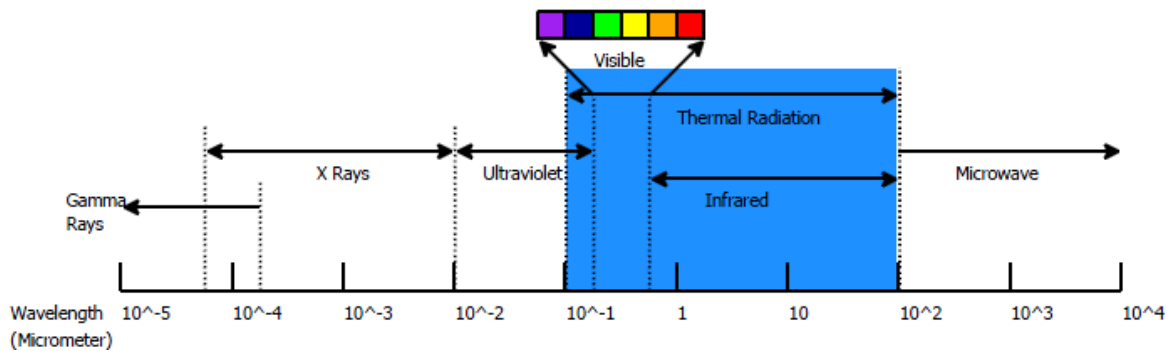


Figure 1.1. The electromagnetic spectrum.

A photographic camera forms images from captured light with wavelengths ranging from 450nm and 750nm. This range of radiation is within the visible portion of the electromagnetic spectrum and can be detected by the human eye. In the absence of sufficient visible light intensity, the human eye and photographic cameras cannot form

useful images. Thermographic cameras operate on similar principles as photographic cameras, but capture electromagnetic radiation in the infrared portion of the electromagnetic spectrum which includes wavelengths ranging from around 750nm to 3000nm.

All matter emits energy as thermal radiation. From the Second Law of Thermodynamics, Matter that is cooler than its surroundings will absorb energy from its surroundings until thermal equilibrium is achieved. Matter will radiate energy to its surroundings if the opposite is true. Because radiation emits in all directions from a source, spherical coordinate systems are used in mathematical descriptions of radiation. The solid angle  $d\Omega$  is the ratio of the area on a sphere's surface to the square of the sphere's radius. The radiant flux  $\Phi$  is a measure of the energy radiated from a source per unit time, or the power. Radiance  $L$  is then a measure of the amount of radiation emitted from an area or

$$L = \frac{\Phi}{da d\Omega}, \quad (1.1)$$

where  $da$  is the surface area from which radiation is emitted (Dushkina, 2009).

Emissivity is a measure of a material's relative ability to emit radiation. Emissivity values range from 0.0 for completely non-emissive to 1.0 for completely emissive. A blackbody is a theoretical standard with an emissivity of 1.0 used to compare the radiative properties of surfaces. It is a diffuse emitter that absorbs all surrounding radiation and emits it back with no energy loss (Incropera et al., 2007).

Planck's Law of Blackbody Radiation is the fundamental principle behind infrared imaging. Planck determined that the blackbody radiance can be calculated as a function of wavelength  $\lambda$  and temperature  $T$  as (Incropera et. al., 2007)

$$L(\lambda, T) = \frac{2hc_o^2}{\lambda^5 \left[ \exp\left(\frac{hc_o}{\lambda kT}\right) - 1 \right]}, \quad (1.2)$$

where  $h$  is the universal Planck constant,  $k$  is the universal Boltzmann constant, and  $c_o$  is the speed of light in a vacuum. The plot of this equation, shown in Figure 1.2, leads to the observations that emitted radiation varies continuously with wavelength and at any wavelength the amount of emitted radiation increases with temperature (Incropera et al., 2007).

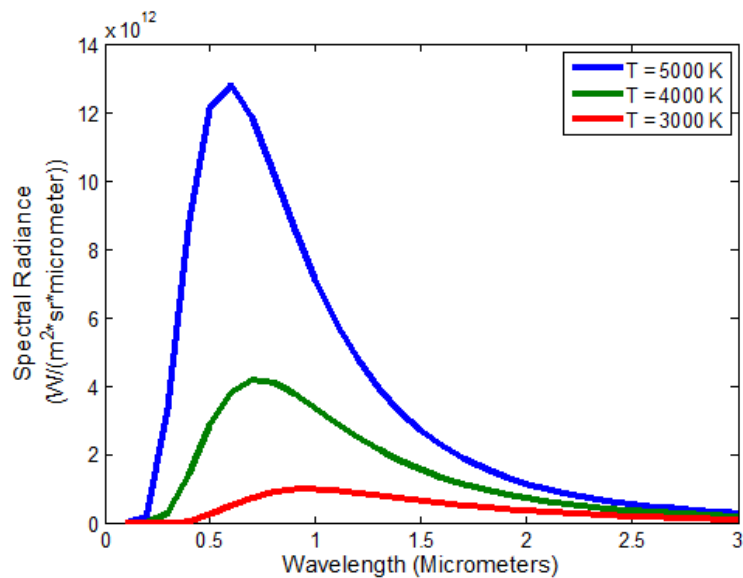


Figure 1.2. Plot of Planck's Law of Blackbody Radiation.

Because of this phenomenon, thermographic imagers can form images based on the relative amount of detected infrared radiation emitted by objects in the field-of-view. This corresponds to the relative temperature of the objects.

From Plank's distribution follows Wein's displacement Law. This Law shows that the maximum radiance occurs at higher temperatures for shorter wavelengths. Significant radiance will occur over a large spectrum of wavelengths. A single thermal imaging system will not be appropriate for all wavelengths and thus the wavelength of radiation for a particular application is a significant design consideration for thermal cameras.

Thermographic cameras produce thermograms. Figure 1.3 is an example of a thermogram.

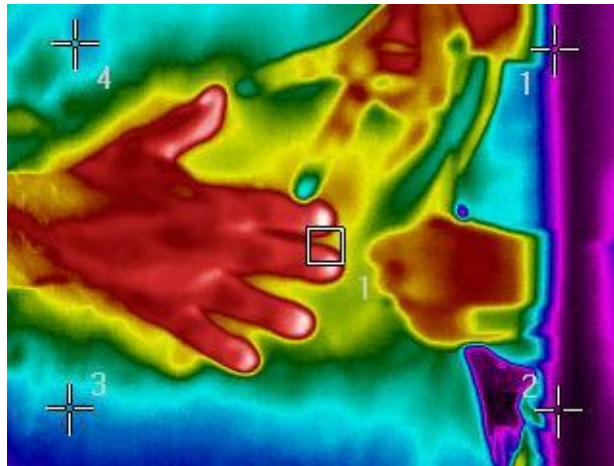


Figure 1.3. Example of a thermogram.

Unlike a photographic camera, the colormap of the image correspond to the relative temperature of the image and not to visible colors. In this case, the coolest sections of the image are one, typically dark, shade and the warmest are a different, typically light, shade with a full spectrum representing the intermediate temperatures. If a true blackbody is measured with a thermographic camera, the temperature will match the temperature of a contact measurement. Since true blackbodies do not exist, thermal cameras will undervalue temperature of an object unless the emissivity value of the object is used as a correction factor.

## **1.2 Applications and Markets for Infrared Imaging**

The ability to form images in the infrared spectrum has many applications. Infrared images can provide accurate and useful information from a scene in situations that a visible spectrum camera will fail such as low-light or hazy conditions. Military applications for infrared imaging devices include target acquisition and reconnaissance. Many civil applications also exist. Thermal imaging helps firefighters and other rescue personnel find victims at night or in smoky buildings. For medical applications, heat distributions through the human body assist doctors in finding areas of swelling or in diagnosing arterial constriction (Miller, 1994).

Infrared imaging can be used for numerous industrial applications. Thermal imaging can detect the amount of heat loss through systems that act as thermal envelopes such as boilers, turbines and engines. Thus, infrared cameras are used for power plant monitoring and non-contact, non-destructive testing of systems. Contractors evaluate

building envelopes in the same way to determine locations of high heat loss. The contractors can then determine the benefits for energy conservation that improved insulation will provide. Infrared imaging is also used for scientific applications including astronomy and geology (Miller, 1994). The needed quality and characteristics of the infrared imaging system are dependent on the application with military operations typically demanding the highest thermal resolution and accuracy.

### 1.3 Infrared Imager Principles of Operation

Although the specifics of infrared imaging systems can vary based on quality and application, all infrared imaging systems share certain primary components. Figure 1.4 provides a diagram of the components of an infrared imaging system.

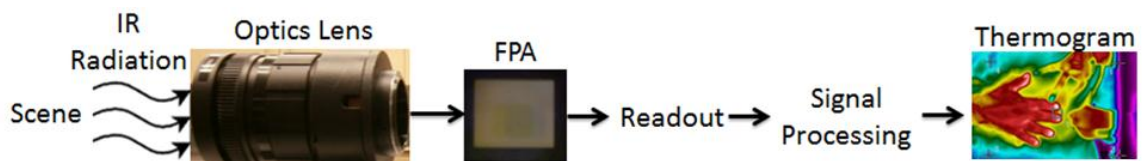


Figure 1.4. Diagram of the components in an infrared imaging system.

An optics system captures and focuses photons from incident radiation across the focal plane array of an infrared detector in a configuration that matches the scene. The detector contains an array of light sensing pixels, or a focal plane array (FPA). A readout system measures the response due to the amount of radiation at each pixel in the array. A signal

processing system analyzes the readout signal. The signal from each pixel in the array corresponds to a single pixel of the thermogram.

## **1.4 Evaluation of Infrared Imaging Systems**

A thermal imager's performance is driven by a number of factors. The quality of the optics determines the field-of-view, depth of focus, and the wavelengths of radiation passed on to the detector. The detector configuration determines the responsivity and range. Responsivity is the ratio of the change in measurement signal to the change in temperature. The units of responsivity vary with readout system. Most detectors function with electrical readouts and so responsivity is measured as Volts/Kelvin. The detector and optical readout quality determine the system level noise and will have the same unit as the measurement signal. The measurement is reliable only when the measurement signal is greater than the noise. The readout also determines the frame rate of the imager. Faster readout and processing allow for a greater number of frames displayed per second.

The Noise Equivalent Differential Temperature (NEDT) is a system level figure of merit for infrared imaging cameras. It is a measure of the incremental temperature that produces a signal equivalent to the noise and thus demonstrates the temperature resolution of the measurement system (Erdtmann et al., 2010). In general NEDT is equal to the ratio of system level noise to responsivity. A low NEDT value facilitates the imaging device's abilities to identify a target with a temperature that varies from the background (Miller, 1994). The NEDT is the primary figure of merit for evaluating the thermal imaging system developed in this Thesis.

## 1.5 Lenses

The lens in an infrared imaging system serves the same purpose as a lens in a photographic imaging system. It focuses incident radiation onto the focal plane of the array. A number of constraints define the optics design. The focal plane array of the detector needs to be located at the focal point of the optics. The field-of-view is the viewable area at the scene. The minimum and maximum working distances define distance from the lens to the object. The depth of field is a range of distances from the lens at which objects will be in focus. The focal ratio, or  $f$ -number, is the ratio of focal length of the lens to its aperture size. A lower  $f$ -number allows more radiation to reach the detector in a period of time. Rays of light are traced through the optical system. Each component has an index of refraction that changes the direction of the array as it passes through the component. The rays of radiation emitted from the object are focused at the focal point (Hall, 2009).

The lens materials provide spectral filtering by limiting the wavelengths of radiation that pass through to the detector. The filter is located near the focal plane array and allows for radiation transmission defined by the response of the detector. Dielectric filters are comprised of layers with alternating high and low refractive indices. The interference from this stack can be designed so that only a specific range of wavelengths can pass through. The range of wavelengths has a sharp cut-on and cutoff. The refractive elements of the optics system can also act as spectral filters. Germanium is often used for infrared imaging applications because of its opaqueness in the visible spectrum and high

transparency from 2000-12000nm of the infrared spectrum. This opaqueness changes with temperature (Miller, 1994).

## **1.6 Types of Infrared Detectors**

The infrared detector is at the heart of an infrared imaging system. The metrics of responsivity, image resolution, cost, wavelength, NEDT, and frame rate are all determined directly by the detector. Many detector types exist with advantages and disadvantages for each of these metrics. Research in infrared imaging involves the development of newer detectors that improve upon the disadvantages present in previous designs.

### **1.6.1 Photonic Infrared Detectors**

To convert radiation into an electronic signal, photonic infrared sensors convert photons into electrons so that electric current can be measured. Infrared photonic detectors take advantage of either photoconductive or photovoltaic effects. The photovoltaic effect occurs in semiconducting materials with a positive and negative layer facing each other and a depletion layer in between. This is a p-n junction. Photons are absorbed by the semiconducting material. In a solid material, low energy electrons will be in the valence band for that material. High energy electrons are in the conduction band. In semiconducting materials, a band gap, where no electron states can exist, is located between the valence band and conduction band. The band gap is thus the energy

needed to move an electron from the valence band to the conduction band. Electrons are excited by the photons to the conduction band, leaving a hole in the valence band.

Electrons then drift towards the p-n junction and reach the n-type region. The holes reach the p-type region. An electric current is produced as a result (Suyama, 2009). The current produced will be directly related to the photon absorption and is measured by a readout circuit.

The photoconductive effect also involves the creation of electron-hole pairs in a semi-conducting material. The charges change the resistance of the material. A voltage is applied across an area and the resulting variation in current due to resistance change is measured by the readout circuit (Suyama, 2009).

The energy  $E$  of a photon is defined as

$$E = \frac{hc}{\lambda}, \quad (1.3)$$

where  $c$  is the speed of light,  $\lambda$  is the wavelength of the photon, and  $h$  is Planck's constant (Young and Freedman, 2008). Electromagnetic radiation with higher wavelengths will have lower energy. A semiconducting material is chosen based on the wavelength of the radiation so that the band gap is appropriate for the photon energy levels. Indium gallium arsenide is a photoconductive and photovoltaic semiconducting material with a band gap appropriate for shortwave infrared radiation with 1400 to 3000 nm wavelengths. Lead salts are a photoconductive material appropriate for short wave and medium wave infrared radiation with wavelengths of 3000 to 5000 nm. Mercury cadmium telluride is a photoconductive and photovoltaic semiconductor appropriate for medium wave into long

wave infrared radiation (Miller, 1994). Other detector types are needed for wavelengths above 25000nm.

Thermal imaging systems with photonic detectors can achieve NEDT values as low as 5-10 mK. Even at operating temperatures, however, these detectors are very susceptible to thermal noise. Noise increases exponentially with temperature. As a result, expensive cryogenic cooling systems are needed to keep noise low and NEDT high. The cooling systems negatively impact weight, mobility, and stability (Miller, 1994). Research has moved towards uncooled detector types.

### **1.6.2 Photothermal Infrared Detectors**

Photothermal infrared detectors respond to the thermal effects of infrared radiation with several types of temperature dependent phenomenon. Microbolometers and pyroelectric sensors are two photothermal infrared detector types. Superconducting materials have allowed for the development of these detectors. Superconducting materials exhibit a sharp decrease in resistance as a response to decreases in temperature until resistance reaches zeros at the material's critical temperature (Young and Freedman, 2008). These changes can be several orders of magnitude in only a few Kelvin near the critical temperature. Microbolometers take advantage of this effect. The microbolometer heats up as it absorbs power from photons. The change in temperature produces a change in resistance in the material which is measured by the readout circuit. Micromachining techniques divide the superconductor into the unit cells of a focal plane array and provide the electrical connections for the readout. Because of the sensitivity of the

superconducting material, the detector needs to be thermally isolated from the environment (Miller, 1994).

Pyroelectric detectors rely on the magnetic properties of superconductors. A superconductor will change the properties of a surrounding magnetic field based on temperature changes (Young and Freedman, 2008). This produces a current in the material as energy is absorbed and the material is heated. Because the effect is only produced by a change, a shutter intermittently allows radiation to be absorbed by the array (Miller, 1994).

Photothermal infrared detectors have the advantage of sensitivities independent of wavelength. Additionally, noise does not increase exponentially with temperature. As a result, these detectors can operate uncooled at room temperature with little consequence. Because an electric signal response is measured at each element of the array, the fabrication is expensive and complex. Electronic noise from the readout circuit and thermal effects of the circuit limit the NEDT of photothermal detectors (Miller, 1994).

### **1.6.3 Optomechanical Infrared Detectors**

The removal of electronic readout systems from the detector array can lower the cost and improve the performance of uncooled infrared imaging systems. Microelectrical mechanical systems (MEMS) provide a solution with optically-read, thermally-deforming micro mechanical detectors. The arrays of such detectors are comprised of bi-material photomechanical pixels. The theory of bending for a bi-metal strip subjected to uniform heating developed by Stephen Timoshenko (Timoshenko, 1925) describes the response of

the sensing elements in the detector. The two metallic layers have different coefficients of thermal expansion. From Timoshenko's analytical model, it becomes possible to predict the amount of deflection as a function of temperature. A larger difference in the coefficients of thermal expansion will lead to a larger deflection per change in temperature (Timoshenko, 1925). The temperature of the beams increases as incident infrared radiation is absorbed. Two materials can be chosen so that the deflection of the sensing element is linear with temperature for an appropriate range of temperatures.

The simplest arrays consist of micro cantilever beams constrained to a substrate. Surface micromachining is the process that creates the cantilevered beam structures. Figure 1.5 illustrates these steps (Dobrev et al., 2009). The process begins with a partially masked silicon wafer. The silicon wafer is the substrate of the detector. The mask blocks the etchant from removing material at particular locations. Wet etching removes the unmasked wafer material as shown in Step 1 of Figure 1.5. A sacrificial layer typically comprised of silica is deposited on to the silicon substrate as shown in Step 2 of Figure 1.5. The sacrificial layer can be more quickly etched away than the materials that comprise the finished component. Chemical polishing removes the mask and a portion of the sacrificial layer until it is flush with the silicon wafer as shown in Step 3 of Figure 1.5. The sacrificial layer sets the gap thickness between the structure and the substrate. The structural bimetallic layers are deposited on top of the sacrificial layer and attached to the silicon substrate at one end as shown in Step 4 of Figure 1.5. Wet etching removes the sacrificial material. The bimetallic cantilever is formed as shown in Step 5 of Figure

1.5. The layers can be 1-2000  $\mu\text{m}$  long and 0.1-5  $\mu\text{m}$  thick (Hsu, 2008). The manufacturing process becomes more complex with the complexity of the array design.

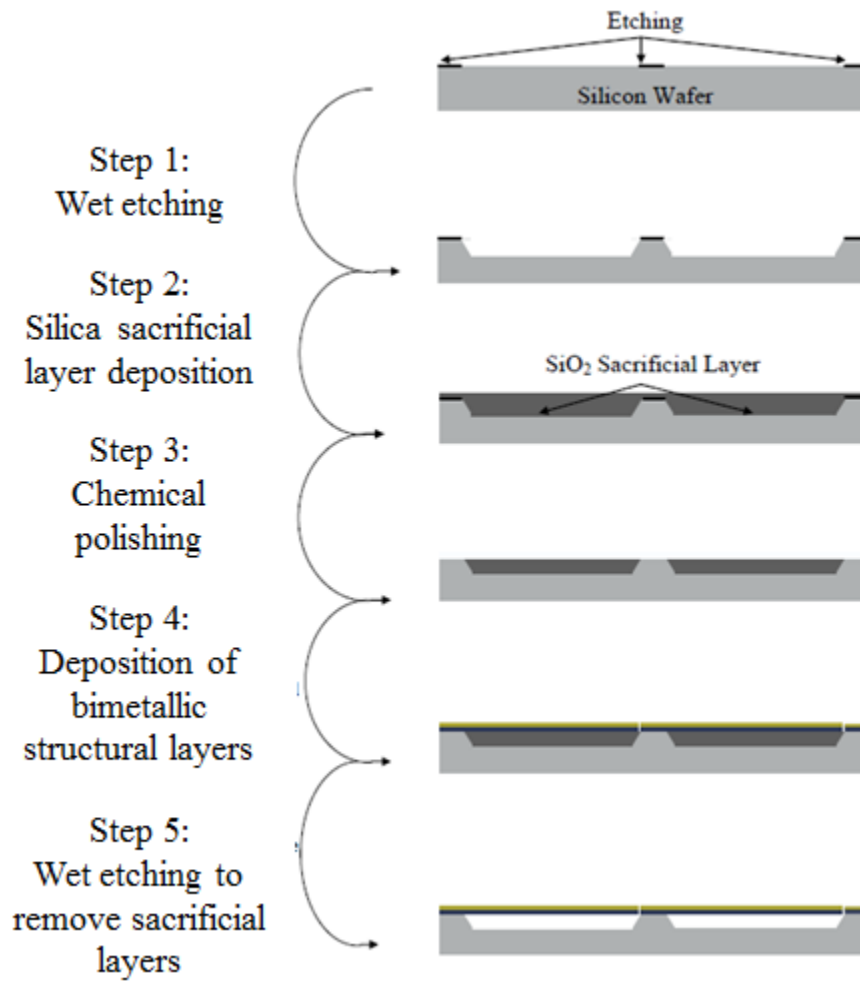


Figure 1.5. MEMS bimetallic cantilever manufacturing process (Dobrev et al., 2009).

Several issues can occur in surface micromachining that can potentially impact the performance of the detector. Delamination of the two layers of the bimetallic beam can occur as a result of excessive thermal or mechanical stress. Stiction can occur when the sacrificial layer is etched away. The cantilever can potentially collapse onto the substrate and the two surfaces can stick (Hsu, 2008). Such manufacturing errors will lead to unresponsive pixels in the array.

Material selection is critical. One material of the bimetallic photomechanical pixel needs to be an efficient absorber of infrared radiation at the appropriate wavelength for the application. The other material needs to be an efficient reflector of visible light so that reflected light intensity can be measured by the optical readout system. Finally the difference in thermal conductivity between the two bimetallic strips needs to be as large as possible to maximize pixel responsivity. Silicon nitride is frequently used as the infrared absorber with an Infrared absorption peak from 8000-14000 nm. Silicon Nitride also has a very low thermal expansion coefficient. Gold and aluminum are frequently used as the reflector because of their high reflectivity in the visible spectrum and also because of their high coefficients of thermal expansion (Li et al., 2007).

Several electronic readout methods have been demonstrated for use with photomechanical arrays. One involves measuring the change in electron tunneling current between electrodes as the tip of the pixel moves (Nezhadian et al., 2008). Independently, a US company launched a thermal imager that measures deflection from changes in capacitance between the tip of the photomechanical pixel and a reference on the substrate as the beam deflects. The NEDT of this system is 50mK (Bogue, 2003). Although

effective, these systems suffer from the same complicated and costly fabrication as microbolometers and pyroelectrics due to the electronic readouts at each pixel.

Optical readout systems have also been combined with photomechanical pixels. The electric readout is removed from the infrared detector. Instead, light is reflected off of the reflective surfaces of the photomechanical array. Light intensity across the array is measured by a CCD camera. The camera digitizes the intensity into discrete gray scale levels. The electric signal at the detector is replaced by the electric signal of the camera. The signal from the camera can be processed further to form a thermogram. Variations in intensity correspond to the amount of tilt on the beams. The tilt is then associated with the temperature change. With the photomechanical array discussed previously and this optical readout method, one group reported an NEDT of 10K (Duan et al., 2003).

Because of the removal of electronic readout in the detector array, shot noise from the optical readout potentially becomes the primary noise contributor in the system. Although noise from thermal effects does not increase exponentially with temperature, thermal noise still needs to be kept below the shot noise of the camera in order to achieve very low NEDT values. A heat shield consisting of a copper cylinder and thermally conductive, transparent sapphire plate can be used to thermally isolate focal plane array (Choi et al., 2003).

An additional arm with a low coefficient of thermal expansion on each photomechanical pixel can also act as a thermal isolator. Two sets of arms connect and isolate the pixel from the substrate. The sensor arm deflects at the same rate as the bimetallic pixel. The deflection of both is proportional to detected radiation from the

scene plus the temperature of the substrate. The compensation arm deflects at a rate proportional to only the substrate temperature. The two arms are situated so that the rotation of the compensation arm opposes the deflection of the sensor arm. As a result, the net deflection of the pixel is proportional only to absorbed scene temperature and is immune to other thermal effects. Figure 1.6 is a diagram of this design (Erdtmann et al., 2010).

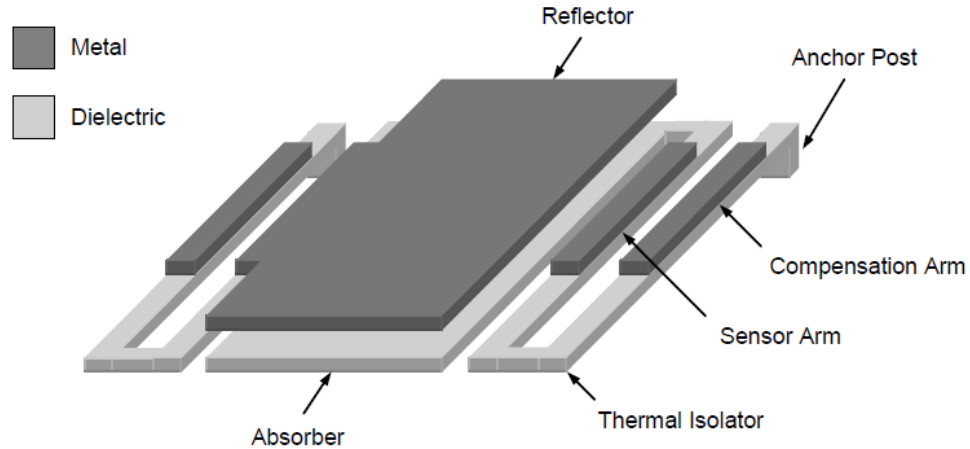


Figure 1.6. Bi-metallic photomechanical pixel with thermal isolator (Erdtmann et al., 2010).

An NEDT of 200mK has been demonstrated with an array with the thermal isolator arms and optical readout (Li et al., 2007). An NEDT below 100mK has also been demonstrated (Erdtmann et al., 2010). The isolator arms are needed in the focal plane array in order to minimize the NEDT.

Many MEMS devices, including the focal plane arrays, are packaged and vacuum sealed for several reasons. The packaging protects the delicate components of the array from contaminants in the environment. It also acts as a thermal isolator and constraint for the detector (Hsu, 2008). To allow for optical readout, two windows are placed on the vacuum sealed package. One window allows infrared radiation to pass through to the absorbing materials of the array. The other allows visible light to be reflected off of the reflective side of the array. The windows need to be transmissive at the correct wavelengths and optically flat to allow for accurate optical readout (Marinis et al., 2008). The optical readout needs to operate correctly within the constraints established by the detector packaging.

The air gap between the substrate and bimetallic structure can provide unwanted air resistance (Dong et al., 2007). Additionally, convection from air currents can impact the response of the device. If the silicon substrate is removed, the air gap is also removed and the array can be in atmosphere (Dong et al., 2007). The removal of the substrate has additional benefits. Reflection and absorption by the substrate can cause 40% of the infrared radiation from the scene to not reach the absorbers in the array. The radiation will reach the array directly if the substrate is removed. Additionally, without the substrate, stiction will not occur and fabrication is simplified (Li et al., 2007). Another method of enhancing absorption is the addition of an optical cavity between the absorber layer and the reflector layer of the bimetallic beam. Optimization of pixel pitch, arm layout and bimetallic pixel geometry among other factors are needed (Erdtmann et al., 2010). These are just a few of the additional design considerations.

The temperature at the detector array is a fraction of the temperature at the scene. A unit less thermal multiplier  $\beta$  relates the scene temperature to the detector temperature as follows

$$\beta = 4F^2 B_\lambda \left(1 + \frac{R_{thr}}{R_c}\right), \quad (1.4)$$

where  $F$  is the focal ratio of the lens,  $B_\lambda$  is the spectral band factor that accounts for the partial acceptance of blackbody radiation by the system,  $R_{thr}$  is the thermal radiation resistance, and  $R_c$  is the thermal resistance of the detector. If the thermal multiplier is equal to 65, a change at the scene of 65K will cause a 1K temperature change at the detector.

## 2 Optomechanical Infrared Detectors with Interferometric Optical Readout

Ideally all of the pixels in the array are flat at room temperature. As shown in Figure 2.1, pixels can be rotated or curved in relation to the ideal geometry as a result of errors in the deposition and etching away of the thin bimetallic layers.

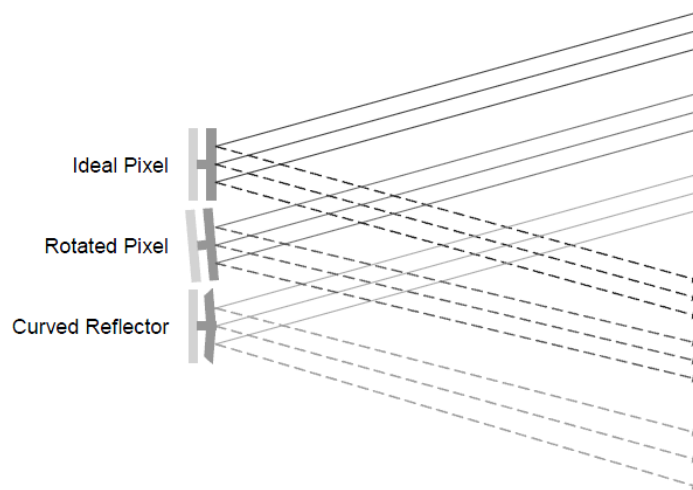


Figure 2.1. Deviations from the ideal pixels impact the uniformity of the intensity of reflected light; this lowers the spatial consistency of the measurements of the array (Erdtmann et al., 2010).

Reflection off of these pixels will have poor contrast in comparison to the ideal pixels. The uniformity issues reduce system level responsivity (Erdtmann et al., 2010). The hypothesis of the present research is that direct measurements of mirror height change across a MEMS IR detector with a holographic optical readout system will

compensate for sensor nonuniformity and improve system level NEDT. If corrections are made through the optical readout system, improved NEDT levels can be achieved without tightening manufacturing tolerances.

The hypothesis is tested on a MEMS infrared detector like those discussed in Section 1.6.3. The MEMS infrared detector is an optimized and vacuum sealed optomechanical array of photomechanical pixels with thermal isolators. The packaged MEMS device is shown in Figure 2.2. The reflective side of the focal plane array can be seen through the optical window. The active sensor area is  $15 \times 13 \text{mm}^2$ . The sealed vent hole for the removal of gases is visible at the top of the image.



Figure 2.2. The packaged MEMS device.

A microscopic view of the individual MEMS components is shown in Figure 2.3. Each micro-mirror is  $45 \times 20 \mu\text{m}^2$ . A release hole left from the manufacturing process is

located at the center of each mirror. The detector consists of an array of  $540 \times 460$  components for a total of 248400. In addition to the mirror, the sensor arm and compensation arm are both visible in the image. These create a gap between rows of mirrors so that less than half of the array area consists of mirrors. A low NEDT will facilitate the imaging devices ability to distinguish a target from the scene. The rate of tilt at the tip of a mirror is 2.4 nm per change in K at the scene. The desired NEDT is 100mK. This corresponds to a change in tip height of 0.24nm for a temperature change of 100mK. The optical system, therefore, needs to make low-noise, full-field, real-time holographic measurements with resolution below 0.24nm. Phase stepping interferometry, a technique often used for the non-destructive evaluation of MEMS components, can meet these criteria (Dobrev et al., 2011, Furlong and Pryputniewicz, 2003, and Rodgers, 2006).

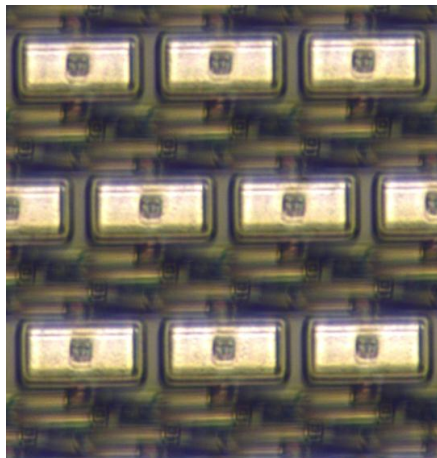


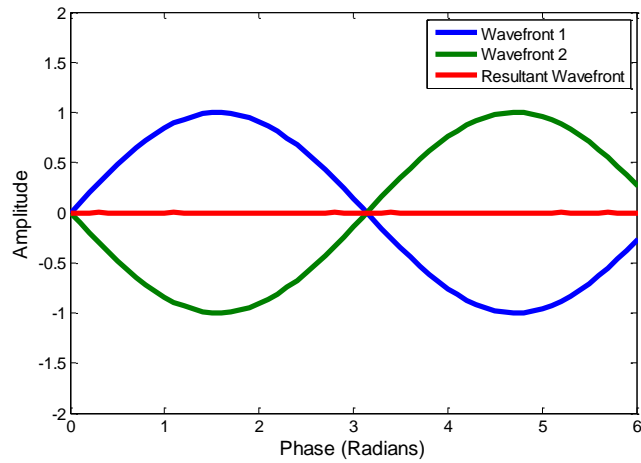
Figure 2.3. Microscopic view of individual mirror components.

## 2.1 Interferometry

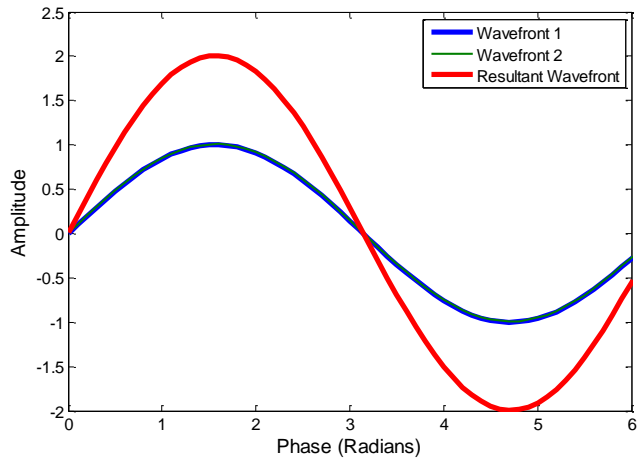
Interferometry is a family of techniques that use the superposition of two or more electromagnetic wavefronts to extract information about the wavefronts. In the correct configuration, this can be used to measure the relative heights across a surface.

Superposition of wavefronts occurs between two overlapping coherent light sources. The waves are coherent if they have a constant relative phase in space (spatial coherence) or a constant relative phase in time (temporal coherence). The coherence length is equal to the maximum optical path length difference between two waves at which they will remain temporally coherent.

When two waves are coherent and monochromatic (one dominant wavelength) the amplitudes of the two wavefronts are added together to form a resulting wavefront with amplitude equal to the summation. If the two wave fronts of the same amplitude have phase offset by  $\pi$  radians, then the interference is completely destructive and the amplitude of the resultant is zero as shown in Figure 2.4a. If two wavefronts have the same phase, interference is completely constructive and the amplitude of the resultant is double that of the original wavefronts as seen in Figure 2.4b (Page, 2009). The phase difference can range from 0 to  $\pi$  radians with the resultant somewhere in between complete constructive and complete destructive interference. Interferometry techniques rely on this interference to extract the phase difference of the waves.



(a)



(b)

Figure 2.4. Interference of wavefronts: (a) out-of phase waves interfering destructively; and (b) in-phase waves interfering constructively

### 2.1.1 Principles of Michelson Interferometry

Michelson Interferometers measure temporal coherence to extract the phase difference of two wavefronts. Figure 2.5 is a diagram of a Michelson Interferometer.

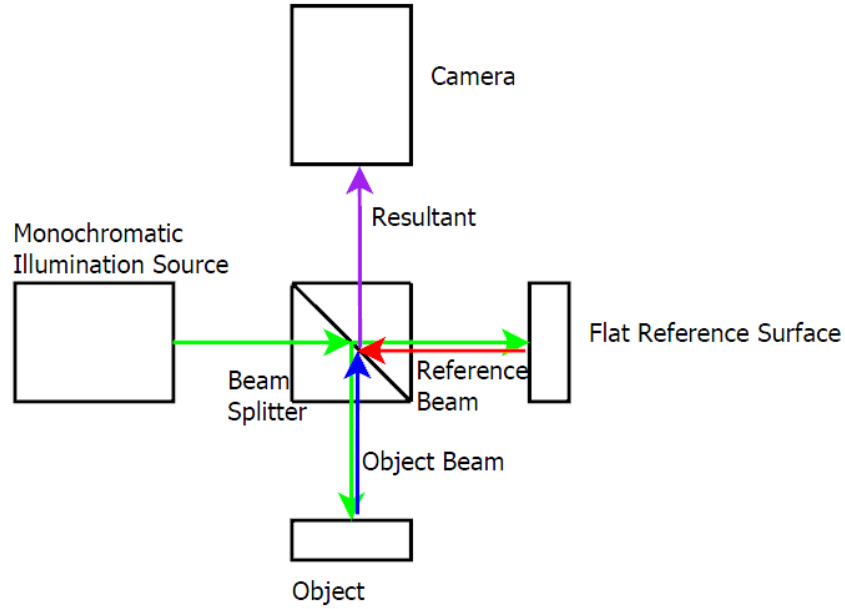


Figure 2.5. Michelson interferometer.

In a Michelson interferometer, a monochromatic beam of light is split into two by a beam splitter. This creates an object beam and a reference beam. The reference beam is reflected off of a flat reference surface. The object beam is reflected off of the object of interest.

At a single equivalent 2-dimensional position  $(x,y)$  on each path, the current displacements of the reference wave  $U_r$  and the object wave  $U_o$  at time  $t$  are given by

$$U_r(x, y, t) = A_r(x, y)e^{i[\phi_1(x,y)-\omega(x,y)t]}, \quad (2.1)$$

and

$$U_o(x, y, t) = A_o(x, y)e^{i[\phi_2(x,y)-\omega(x,y)t]}, \quad (2.2)$$

where  $A$  is the amplitude of the waves,  $\phi_1$  is the phase of the reference wave,  $\phi_2$  is the phase of the object wave and  $\omega$  is the angular frequency of each wave. The two beams

then recombine back at the beam splitter. If the optical path length difference of the object and reference paths is less than the coherence length of the light source, the wavefronts of the two beams interfere as they recombine. The result is the sum of the individual wave displacements, or

$$U(x, y, t) = U_o(x, y, t) + U_r(x, y, t). \quad (2.3)$$

The intensity  $I$  of the recombined beams at point  $(x,y)$  is then equal to the integral of  $U$  multiplied by its complex conjugate, or

$$\begin{aligned} I(x, y) &= \int U(x, y, t)U^*(x, y, t)dt \\ &= A_r^2(x, y) + A_o^2(x, y) \\ &\quad + 2A_r(x, y)A_o(x, y) \cos[\phi_2(x, y) - \phi_1(x, y)]. \end{aligned} \quad (2.4)$$

The amplitude and intensities of the individual wavefronts are related as

$$I_r(x, y) = A_r(x, y)^2, \quad (2.5)$$

and

$$I_o(x, y) = A_o(x, y)^2. \quad (2.6)$$

Equation 2.4 can then be rewritten as

$$\begin{aligned} I(x, y) &= I_o(x, y) + I_r(x, y) \\ &\quad + 2\sqrt{I_o(x, y)I_r(x, y)} \cos(\phi_2(x, y) - \phi_1(x, y)). \end{aligned} \quad (2.7)$$

If at location  $(x,y)$  the interference is constructive, the intensity of the recombined wavefront will be higher than the intensities of the two split wavefronts and appear bright. If at location  $(x,y)$  the interference is destructive, the intensity of the recombined waves will be low and appear dark. A camera records the intensities at all positions of  $(x,y)$ , discretized by the resolution, for the recombined waves. The camera discretizes intensity into grayscale levels with black for no intensity, and white for the highest intensity before pixel saturation.

The number of these grayscale levels  $n$  is

$$n = 2^{bit\ depth} . \quad (2.8)$$

These regions of light and dark are interference fringes. The relationship between phase difference and fringe appearance is shown in Figure 2.6.

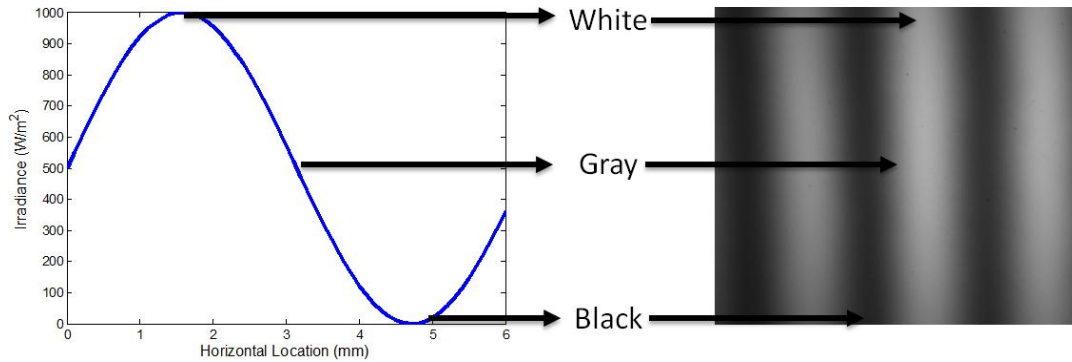


Figure 2.6. Relationship between optical phase and fringe intensity

If amplitude is assumed to be constant for the object and reference beams, then the intensity of the recombined waves at  $(x,y)$  is dependent only on the phase difference between the two waves. An interferogram is a captured image with interference fringes.

Fringes will appear only if the optical path length difference between the two paths is less than the coherence length of the light source. Fringe contrast  $V$  is

$$V = \frac{I_{max} - I_{min}}{I_{max} + I_{min}} , \quad (2.9)$$

where  $I_{max}$  and  $I_{min}$  are the maximum and minimum intensities of an interferogram. Once fringe contrast falls too low the two waves are incoherent (Cloud, 1995). Fringe contrast

should be maximized when interferometric measurements of phase difference are made. When fringes appear, the two path lengths are nearly equal at point  $(x,y)$ . The reference surface of a Michelson interferometer is smooth so that any surface irregularities on the object surface will introduce a measurable phase difference

The fringe-locus  $\Omega$  is equal to the phase difference of the two interfering waves:

$$\Omega = \phi_2 - \phi_1. \quad (2.10)$$

The fringe-locus function can be calculated geometrically. After several assumptions and simplifications (Cloud, 1995), the sensitivity vector  $\mathbf{K}$  is the difference between the observation vector  $\mathbf{K}_2$  and the illumination vector  $\mathbf{K}_1$ , or

$$\mathbf{K}(x, y) = \mathbf{K}_2 - \mathbf{K}_1. \quad (2.11)$$

The wavenumber  $K$  is equal to the magnitude of the wave vectors and is defined as

$$K = |\mathbf{K}_1| = |\mathbf{K}_2| = \frac{2\pi}{\lambda}, \quad (2.12)$$

where  $\lambda$  is the wavelength of the monochromatic light source. The displacement vector  $\mathbf{D}$  defines the distance in 3-dimensional space between the two vectors and is defined as

$$\mathbf{D} = D_x \mathbf{i} + D_y \mathbf{j} + D_z \mathbf{k}, \quad (2.13)$$

where  $\mathbf{i}$ ,  $\mathbf{j}$ , and  $\mathbf{k}$  are unit vectors and  $D_x$ ,  $D_y$ , and  $D_z$  are the respective magnitudes of displacement. The fringe-locus is equal to the scalar product of the sensitivity vector and the displacement vector (Cloud, 1995), or

$$\Omega(x, y) = \mathbf{K} \cdot \mathbf{D}. \quad (2.14)$$

If the illumination and observation conditions are parallel as shown in Figure 2.7, then the problem becomes 1-dimensional.

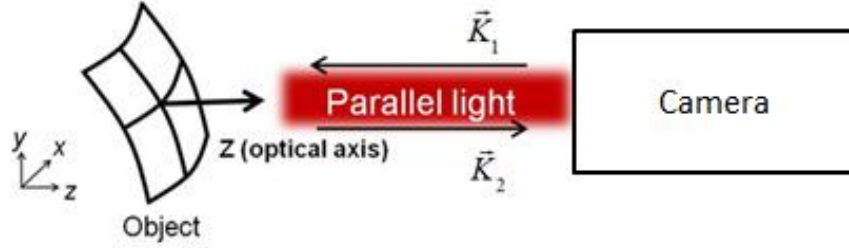


Figure 2.7. Parallel illumination and observation conditions.

As a result, Equation 2.14 simplifies to

$$\Omega(x, y) = \frac{4\pi}{\lambda} D_z(x, y). \quad (2.15)$$

If a Michelson interferometer is used to measure the phase difference, and the wavelength of a monochromatic light source is known, then Equation 2.15 can be solved for the optical path length difference  $D_z$  as

$$D_z(x, y) = \frac{\Omega(x, y)\lambda}{4\pi}. \quad (2.16)$$

The Michelson interferometer can then be used to measure relative out of plane height differences at all points  $(x, y)$  on a surface of interest. The theoretical limit of height resolution is determined by the cameras discretization of intensity into grayscale and the diffraction limit of the optics.

Double exposure is a holographic technique used to measure temporal changes in phase or height as a result of loading rather than relative height differences spatially across a surface. Two or more height maps are recorded. The first recorded height map is the reference. Loading occurs in the subsequent exposures. No other disturbances can occur during recording and the relative  $(x, y)$  positions need to stay consistent between

frames. The height value at time  $t$  at each  $(x,y)$  point can be subtracted from the reference value at that same position to calculate a change in height  $D_{z\Delta}$ ,

$$D_{z\Delta}(x, y, t) = D_{z0}(x, y, t_0) - D_{zt}(x, y, t). \quad (2.17)$$

For the case of the photomechanical array, this calculated change in height corresponds to a change in temperature.

### 2.1.2 Phase Stepping to Improve Interferometry

The phase is needed to calculate the height. The term  $I(x,y)$  as measured by the camera is the only known in Equation 2.7. The equation has three unknowns, with only the fringe-locus  $\Omega(x,y)$  needed. A minimum of three equations is needed to solve a system of equations. These equations can be created by taking a series of additional images with known additional phase offsets at each image. The four-step algorithm uses the following four equations taken at equal phase offsets of  $\pi/2$  as (Cloud, 1995)

$$I_1(x, y) = I_o(x, y) + I_r(x, y) + 2\sqrt{I_o(x, y)I_r(x, y)} \cos[\Omega(x, y) + 0], \quad (2.18)$$

$$I_2(x, y) = I_o(x, y) + I_r(x, y) + 2\sqrt{I_o(x, y)I_r(x, y)} \cos[\Omega(x, y) + \frac{\pi}{2}], \quad (2.19)$$

$$I_3(x, y) = I_o(x, y) + I_r(x, y) + 2\sqrt{I_o(x, y)I_r(x, y)} \cos[\Omega(x, y) + \pi], \quad (2.20)$$

and

$$I_4(x, y) = I_o(x, y) + I_r(x, y) + 2\sqrt{I_o(x, y)I_r(x, y)} \cos[\Omega(x, y) + \frac{3\pi}{2}]. \quad (2.21)$$

The four-step technique requires more image acquisition time, but is also more reliable than the three-step technique. There is no limit to the number of phase steps that can be used. Four-phase steps will allow for near real-time measurements. This is limited

by the camera frame rate and image processing time. The solution for  $\Omega(x,y)$  from this system of equations is (Cloud, 1995)

$$\Omega(x, y) = \tan^{-1} \frac{I_4(x, y) - I_2(x, y)}{I_1(x, y) - I_3(x, y)}. \quad (2.22)$$

In this case, the inverse tangent is modified to take into account diametrically opposite directions.

The modulation image provides a time-averaged representation of the phase-stepped images to show the regions with peak fringe contrast. Bright sections of the modulation image have strong fringe contrast while dark regions have low fringe contrast. The modulation  $\gamma$  at position  $(x,y)$  is

$$\gamma(x, y) = \frac{\sqrt{[I_4(x, y) - I_2(x, y)]^2 + [I_1(x, y) - I_3(x, y)]^2}}{2I_o}. \quad (2.23)$$

Once the phase difference is calculated, Equation 2.16 can be solved for height. This technique is known as phase-stepping interferometry (PSI) (Cloud, 1995).

Because of the nature of the inverse tangent function, the solutions for phase in Equation 2.22 are constrained between values of  $-\pi$  and  $\pi$ . As a result, two consecutive points in the  $(x,y)$  space can have a sharp discontinuity in height, even when logically the difference should be small. This phenomenon is known as phase wrapping. The development of phase unwrapping algorithms to remove these discontinuities is a major field of research in interferometry. Furthermore, if a real discontinuity on an object of interest has a height corresponding to a phase change greater than  $2\pi$  radians, the height difference is ambiguous.

Assuming the use of double exposure and a monochromatic light source with wavelength of 620nm, the reflector height change due to tilt needed for wrapping to occur coincides with a phase change of  $2\pi$ . From Equation 2.16, this corresponds to a change in height of 310nm. At a responsivity of 2.4nm/K, a temperature change of 129K is needed for wrapping to occur. The detector will not normally be exposed to such large temperature variations. As long as changes in height are measured using double-exposure, wrapping will not be a major concern.

The known phase-steps for the four step algorithm are introduced in either the object beam or the reference beam of the interferometer. Either the object or the reference is attached to a piezo-electric nanopositioner. These positioners are composed of ceramics with crystalline structures that exhibit the piezo-electric effect. The ceramics expand linearly as a function of applied voltage. When used as mechanical positioners, the ceramics provide near linear expansion controllable to sub-nanometer resolution. For the four-step algorithm, the positioner changes the optical path length difference by wrapped increments of  $\pi/2$ . From Equation 2.16, the linear displacement corresponding to the appropriate phase change is calculated. The corresponding voltage is determined by the displacement versus voltage curve of the positioner.

Image acquisition needs to be synced with the positioner so that one image is recorded at each of the four phase steps. If the two are not synced properly, the calculated optical phase map will be incorrect. A camera captures an image by opening a shutter and briefly exposing its focal plane array to visible light from the scene. The amount of time the shutter is open is known as the exposure time. Exposure time varies by application

and camera, but is often on the order of milliseconds. The frame rate of a camera is defined as the number of captured frames in a one second time interval or frames per second. The shutter is also controlled by a voltage signal. The two signals need to be synced so that positioning occurs in-between exposures as shown in Figure 2.8 for two phase-stepping cycles.

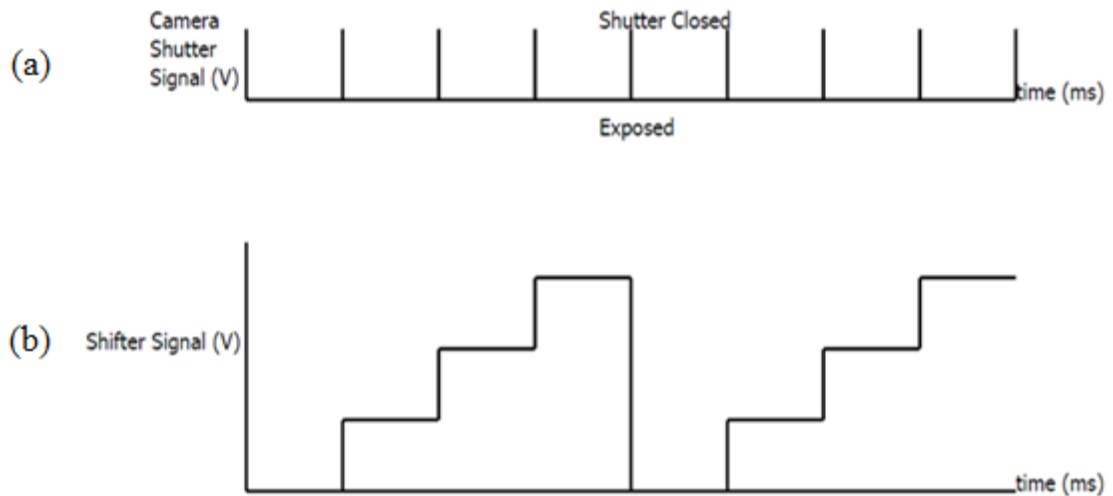


Figure 2.8. Synchronization in time between (a) camera shutter signal and (b) piezoelectric positioner signal.

The relationship between the components in a Michelson interferometer is shown in Figure 2.9. A monochromatic LED or laser illumination source is split into two beams at the beam splitter. The object beam is reflected off of the object of interest. The reference beam is reflected off of the reference mirror. The reference mirror is mounted

on a piezo-electric positioner that moves the reference path by the known phase steps. The two beams recombine at the beam splitter and the camera captures the resultant fringe pattern. Images from the camera are sent to a computer for post processing. The computer also syncs the camera's image acquisition with the motion of the phase stepper.

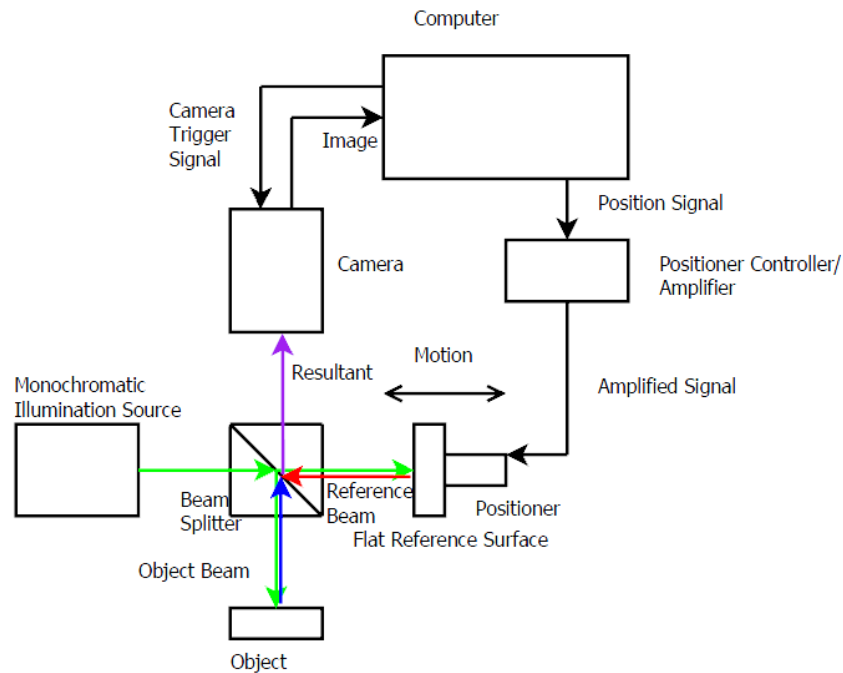


Figure 2.9. Phase-stepping interferometry system.

## 2.2 Vacuum Seal and Compensation

An optical window allows the object beam of the interferometer to reach the reflective portion of the array. The window of the vacuum sealed package in the object

path of the interferometer introduces additional optical path length difference between the object beam and reference beam because of the difference between the densities of air and the glass. The change in optical path length difference is likely to be greater than the coherence length of the illumination source and no modulation will occur as a result. To correct for this and allow for interferometric measurements of the MEMS device, a compensation glass of the same material and thickness must be placed in the reference path so that the optical path lengths will match. This technique has been demonstrated with interferometric measurements of vacuum sealed MEMS devices (Marinis, 2009).

### **2.3 Previous Work**

Holography techniques have been used in the past to correct for shape distortions of focal plane arrays. This involves two steps. The first is the recording of an uneven wavefront as reflect off of the array onto a holographic plate. The plate is exposed, developed, and used to correct for shape using the optical readout methods discussed previously. Although an infrared image of a soldering iron is demonstrated, the noise is high to produce images of cooler objects (Liu et al., 2009). This is similar to the double exposure method, but requires extra steps to produce the holographic plate.

The use of interferometry to measure real time deflections of an unpackaged MEMS focal plane array has also been demonstrated. A Linnik interferometer employing the four phase step method and custom extraction algorithms is used to measure deflections of an array heated by a known amount with a custom stage. Measurements are calculated in post processing. The measured responsivity of the array is 87nm/K (Dobrev

et al., 2011). This is verified through finite element modeling and analytical calculations. From Equation 1.4, this corresponds to responsivity on the order of 0.75nm/K based on the temperature change at the scene. The responsivity of this device is low. This increases the difficulty of achieving low NEDT values.

## **2.4 Goals**

The current detector is optimized and vacuum-packaged with an expected nominal responsivity of 2.4nm/K. The goals of the present research are as follows:

1. Verify the use of a compensation window to make measurements of the packaged MEMS device with interferometry.
2. Demonstrate that phase-stepping interferometry can achieve the needed accuracy and resolution.
3. Develop an interferometric optical readout system that can measure real-time displacements of the mirrors on the focal-plane array.
4. Develop a software algorithm that converts displacements into real-time infrared images.
5. Demonstrate that this optomechanical infrared imaging system can potentially achieve an NEDT of 100mK.

### **3 Verification of Compensation Window Effectiveness**

The MEMS detector is in a vacuum sealed package with an optical window to allow for optic measurements. As discussed in Section 2.2, a compensation window of the same material and thickness as the optical window is needed in the reference beam to compensate for the change in optical path length along the reference beam. Without compensation, interference will not occur and measurements cannot be made. The compensation window needs to be tested before further development of the optical readout system.

#### **3.1 Experimental Setup for Verification of the Compensation Window**

A Michelson interferometer is used to test the compensation window. Figure 3.1 is an image of the Michelson interferometer used to verify the use of the compensation window. Illumination is provided by a red monochromatic LED. The beam splitter divides the light from the LED to the object path with the MEMS detector and the reference path with the phase stepping reference mirror. The two reflected beams recombine at the beam splitter. Light is focused onto the focal plane array of the camera by a telecentric lens with 0.85X magnification. The telecentric lens makes all of the beams parallel so that constant magnification is provided throughout the image. The camera records intensity and the captured images are saved on a computer.

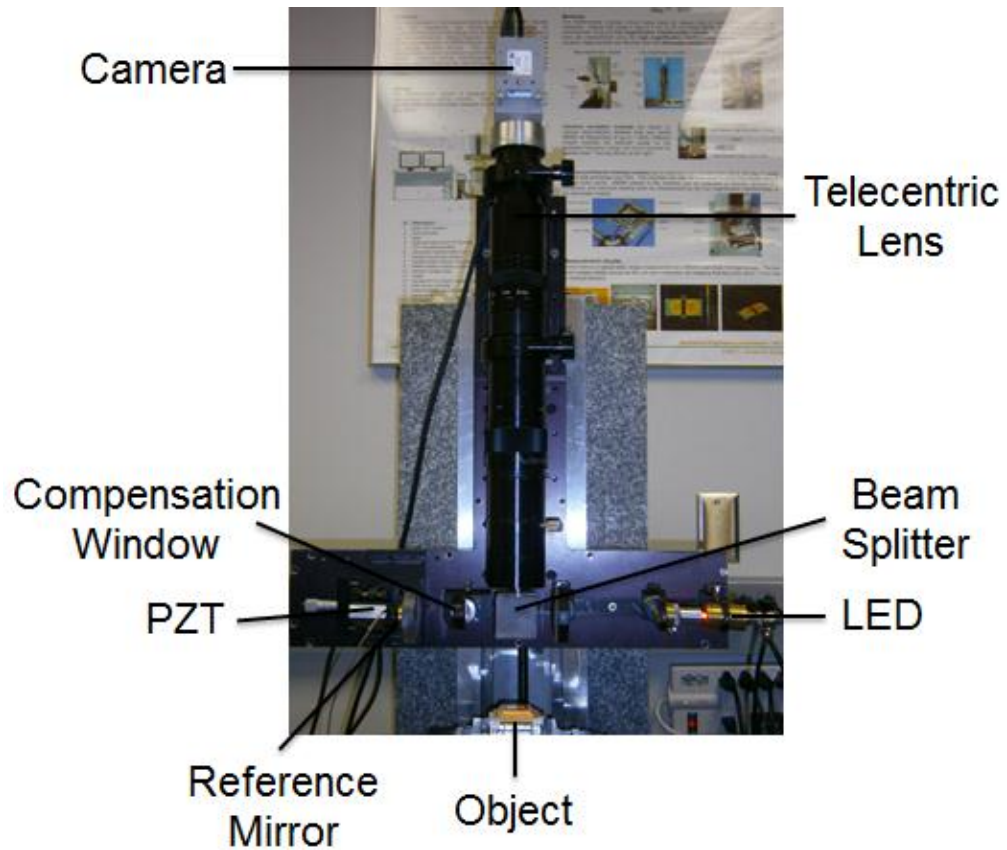


Figure 3.1. Michelson interferometer with compensation window.

The unique aspect of this system is the addition of the compensation window along the reference path. Figure 3.2 shows the mounted compensation window and the reference mirror. The glass is from the same stock as the optical window on the component. The compensation window is mounted on a holder and placed along the reference path to compensate for the change in optical phase difference introduced by the optical window in the object path.

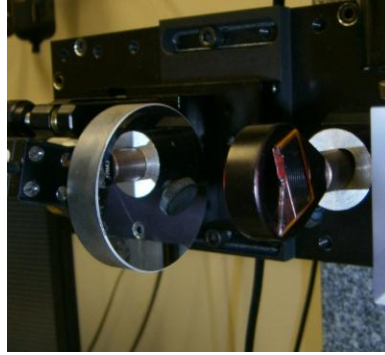


Figure 3.2. Compensation window and reference mirror.

### 3.2 Results for Compensation Window Effectiveness

The compensation window allows for the capture of interferograms on the focal plane array. Figure 3.3 is an example of one of these interferograms.

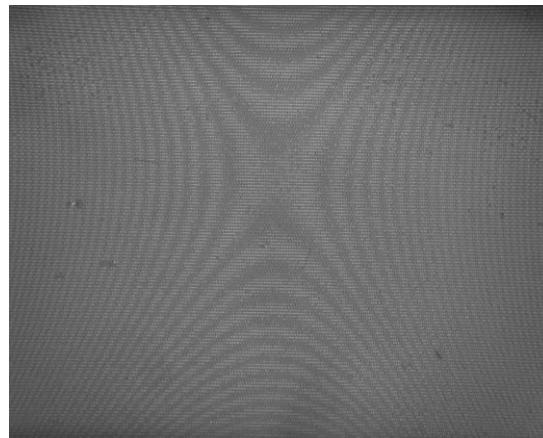


Figure 3.3. Interferogram of a  $10 \times 8 \text{mm}^2$  section of the array.

This leads to several significant observations. The images, captured at the center of the focal plane array, are  $10 \times 8 \text{ mm}^2$ . This is 40% of the entire array area. At this magnification, each mirror is represented by  $5 \times 2$  pixels. This spatial resolution of each mirror is not large enough to clearly define the tip, where height change is at a maximum.

The fringe pattern shows deformations in the array's substrate. The four phase step algorithm is used to calculate the relative heights. The unwrapped and filtered height map is provided in Figure 3.4. The substrate has a saddle-like shape. The maximum height difference is over  $10 \mu\text{m}$  in the viewable area alone. Height variations are even greater in a viewing area that encompasses the entire array. The central portion of the array is the flattest.

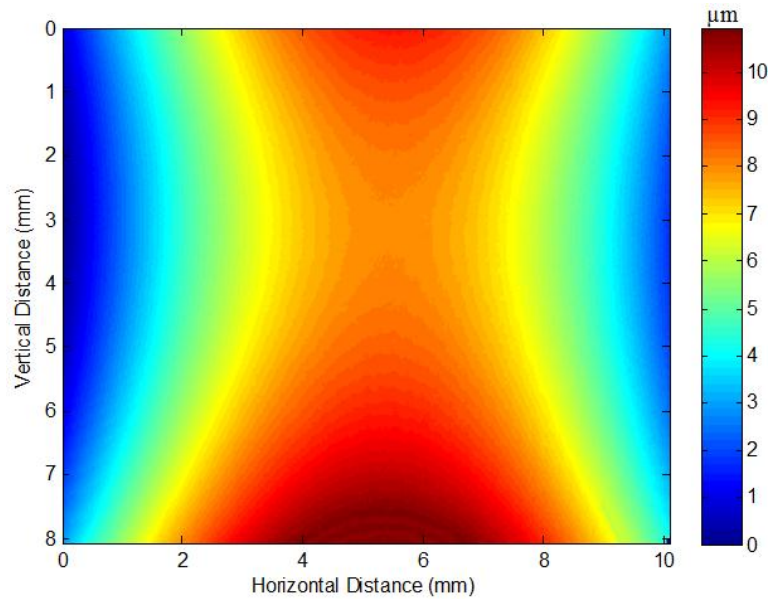


Figure 3.4. Height map of detector substrate showing the saddle-like shape .

### **3.3 Conclusions of Tests for Compensation Window Effectiveness**

Phase-stepping interferometry with a compensation window has been demonstrated as a valid technique to measure the focal plane array of the detector. The measurements lead to several additional conclusions. The magnification of this system is too low to resolve the needed detail to measure tip height change. Ideally, the array is flat. The actual array has a saddle shape and a maximum height difference in this region is 10 $\mu$ m. Double exposure will correct for the deviations from flatness. Nevertheless, interference will not occur for the entire detection area at once if the maximum height difference exceeds the coherence length. The coherence length of high powered LED illumination source is around 10-30 $\mu$ m depending on the wavelength and bandwidth. Furthermore, the depth of field needs to be greater than the maximum height difference of the viewable area so that the viewable area is in focus all at once. The center of the array is the flattest section. Measurements are made in this region.

## **4 Demonstration of Accuracy and Repeatability in PSI**

A phase shifting interferometer with a compensation window can measure heights across the vacuum sealed array of the IR detector. The accuracy and resolution of this technique also need to be verified. The characterization of accuracy and precision is needed to demonstrate the techniques reliability and applicability for measurements of micro mirror displacement. The beams deflect at a nominal rate of 2.4nm/K. To achieve the target NEDT of 100mK the system needs to have a measurement resolution of 0.24nm or below.

### **4.1 Parameters Affecting Accuracy and Repeatability in PSI**

A number of setup parameters can potentially impact the measurement accuracy and repeatability. These include the following (Furlong, 2007):

- Image acquisition system
- Phase step calibration
- Characterization of the light source
- Consistency of illumination and observation conditions

#### **4.1.1 Image Acquisition**

An appropriate image acquisition system needs to be selected. If the diffraction limit of the system is not reached first, then the theoretical limit of measurement resolution is based on the number of gray scale levels the camera can resolve. An 8-bit

camera will have 256 grayscale levels to discretize light intensity levels. Assuming 620nm monochromatic illumination, this translates to a minimum resolvable phase of 0.02 radians or 1.2nm. This does not provide a high enough resolution to measure displacements of 0.24nm. Alternatively, a 12-bit camera will have 4096 grayscale levels, a minimum resolvable phase of 0.0015 radians, and a minimum resolvable height of 0.076nm. This is adequate for the measurement of 0.24nm displacements.

The actual resolution will not be as fine as the resolution set by the bit depth. The resolution is also limited by camera repeatability, or noise. Every electronic device that sends a signal has noise. In a camera, noise is characterized as random variations in detected intensity. The random variations impact the repeatability of measurements. Because of noise, two otherwise identical images will have slight variations in intensity distributions. Low repeatability in intensity measurements directly impacts the repeatability of the height measurements with the phase shifting technique. The repeatability can be improved through averaging.

Spatial noise is a measure of these fluctuations in a single image independent of time. Two pixels in a region of an image that have the same intensity will vary slightly. Additionally, the camera can display outlier values for intensity measurements that do not match the surrounding pixels. Because the phase stepping algorithm depends on the measurement of bright and dark fringes of images, spatial noise reduces the accuracy and repeatability of phase measurements. 2D median filtering directly reduces spatial noise by replacing the value at each pixel in an image by the median of the  $n \times n$  surrounding pixels as shown in Figure 4.1 for a  $3 \times 3$  kernel size. In this case, the median filter

removed the outlier intensity value of 200 and replaced it with the median intensity value for the region of 50. This process is repeated for every pixel in an image. Processing time can be long for large images.

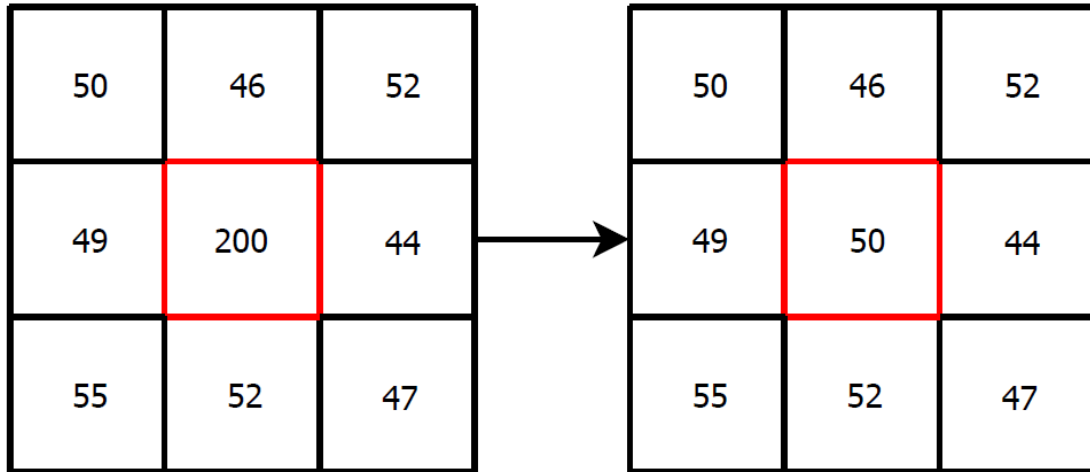


Figure 4.1. Spatial median filtering on a  $3 \times 3$  kernel, before and after the application of a low-pass filter.

Temporal noise is a measure of these fluctuations in time for individual pixels. With no uncertainty, the intensity measured by a camera at a single pixel will be constant for all time as long as the scene remains constant. Due to uncertainty, the intensity measured at a pixel varies in time and a flickering can be viewed in an image stream as the pixel intensities fluctuate. Because 4 frames taken at different times are used in the phase-stepping algorithm, temporal noise reduces the accuracy and repeatability of noise

measurements. Averaging the corresponding pixels of consecutive frames will reduce the uncertainty as shown in Figure 4.2. This temporal averaging improves temporal noise.

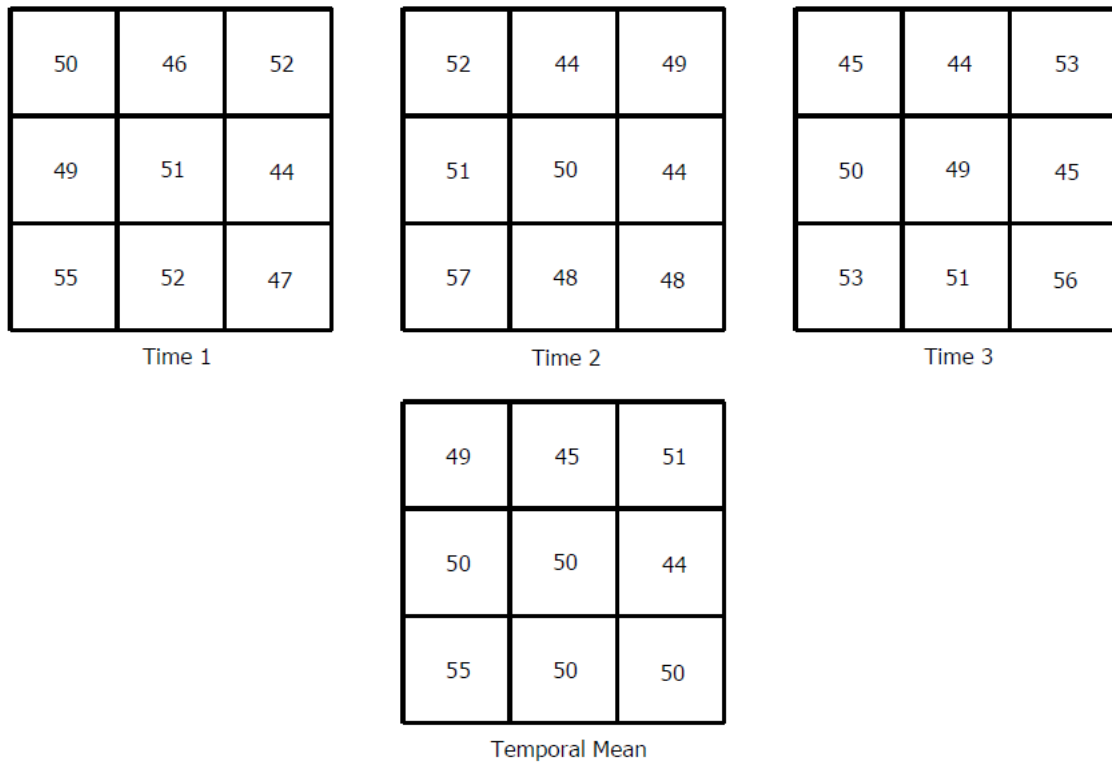


Figure 4.2. Three frame temporal averaging of pixel intensities in an image region; the resultant values for each pixel are the arithmetic averages of each of the corresponding pixels.

Spatial noise and temporal noise are not mutually exclusive. A reduction in spatial noise through median filtering can improve temporal uncertainty. A reduction in temporal noise through temporal averaging can improve spatial uncertainty. Spatial filtering of large images slows down the image acquisition rate and prevents real-time phase

measurements. The camera needs to capture additional images at each phase step so that frames can be temporally averaged. As long as the camera frame rate is fast enough, frame averaging can be applied while still allowing for near real-time measurements of phase. For all measurements temporal averaging is applied to the real time acquisition of images. The spatial median filter is only applied in post-processing.

A number of factors contribute to noise in cameras. Brighter regions of an image will have a stronger signal to noise ratio than darker regions due to the higher intensity of the captured light. A short exposure can also negatively impact the noise by not allowing enough light to be captured. A long exposure, however, will allow too much light to reach the array and the pixels will become saturated. A saturated pixel holds the maximum number of photons. Thus, all saturated pixels will always be represented with the greatest gray scale level for intensity. Finally, a larger pixel size will allow more photons to be captured at a given exposure. This also improves the signal to noise ratio, but at the expense of resolution. A larger pixel size reduces the available number of pixels.

#### **4.1.2 Phase-Step Calibration**

The four phase step algorithm assumes that the images are acquired at 4 equal steps separated by a phase of  $\pi/2$ . If this is not the case, the calculated phase map will be inaccurate. Nevertheless, some amount of non-linearity always exists in the nanopositioner, leading to uncertainty in the measurement. This deviation from the ideal response is known as hysteresis error and is demonstrated in Figure 4.3. The ideal

response is a linear relationship between voltage and displacement for loading and unloading. In an actual system, the response is not linear, nor is it repeatable for loading and unloading. The amount of hysteresis depends upon the quality of the positioning system. Many positioning controllers accept closed-loop position feedback from the positioner so that hysteresis can be corrected. Vibrations from the environment can also introduce random unintentional variations in phase. Interferometers are often mounted on optical air tables to dampen these vibrations.

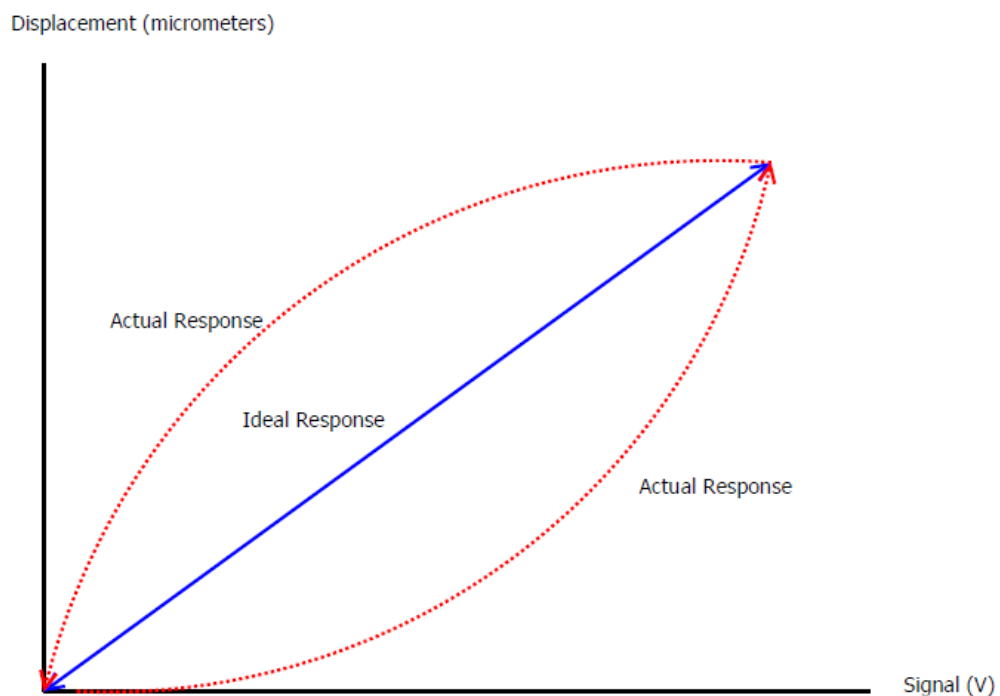


Figure 4.3. Hysteresis error in the positioner as shown by the difference between the ideal and actual response in the displacement versus signal curve.

Hysteresis errors can lead to shifter miscalibration. Many algorithms have been developed to improve the accuracy of phase stepping interferometry. These can be complex. To ensure real-time measurements, the four-step algorithm is still employed here. Calibration techniques can be used to ensure that the voltage applied to the positioner will introduce nearly the correct phase.

Calibration can be performed iteratively. A driving voltage with generating phase  $\phi$  is chosen so that intensities are measured at 5 known phase steps

$$I_1(x, y) = I_o(x, y) + I_r(x, y) + 2\sqrt{I_o(x, y)I_r(x, y)} \cos[\Omega(x, y) - 2\phi], \quad (4.1)$$

$$I_2(x, y) = I_o(x, y) + I_r(x, y) + 2\sqrt{I_o(x, y)I_r(x, y)} \cos[\Omega(x, y) - \phi], \quad (4.2)$$

$$I_3(x, y) = I_o(x, y) + I_r(x, y) + 2\sqrt{I_o(x, y)I_r(x, y)} \cos[\Omega(x, y)], \quad (4.3)$$

$$I_4(x, y) = I_o(x, y) + I_r(x, y) + 2\sqrt{I_o(x, y)I_r(x, y)} \cos[\Omega(x, y) + \phi], \quad (4.4)$$

and

$$I_5(x, y) = I_o(x, y) + I_r(x, y) + 2\sqrt{I_o(x, y)I_r(x, y)} \cos[\Omega(x, y) + 2\phi]. \quad (4.5)$$

The calibration can then be carried out using four of the five equations with (Hariharan et al., 1987)

$$\cos(\alpha) = \frac{I_5(x, y) - I_1(x, y)}{2(I_2(x, y) - I_4(x, y))}, \quad (4.6)$$

where  $\alpha$  is the calculated phase step with the specified voltage. The unused equation is used to check the error of the calculated phase step. The procedure is iterated until the error is minimized and the phase step  $\alpha$  for an applied voltage is approximately equal to  $\pi/2$  radians. This helps to ensure accuracy in the phase calculations.

### **4.1.3 Illumination Characteristics**

Equation 2.16 for the calculation of height from phase assumes that the illumination is monochromatic. This means that the light has only one wavelength. In actuality, all light encompasses a range of wavelengths. The specified wavelength is dominant. The bandwidth describes the range of wavelengths. LEDs have wider bandwidths and shorter coherence lengths than lasers. Fringes will only appear when the two path lengths are within the coherence length. The wavelength of an LED is not as well defined because of the wider bandwidth. If the characterization of the illumination source's wavelength is not correct, the height calculation from optical phase will be inaccurate.

### **4.1.4 Consistency of Illumination and Observation Conditions**

The calculations for fringe-locus function described in 2.1.1 assume parallel illumination and observation conditions. If the setup is not carefully controlled, the beams can diverge from parallel. For instance, the surface of either the object or reference can be unevenly illuminated. In this situation, even if two locations in the  $x$ - $y$  space are at the same height, the measured intensity at one location will be greater. Thus, the calculated phase and height difference is inaccurate. The same will occur if a significant tilt is present between the object and reference. The tilt can be partially removed by adjusting a tilt stage until less than a single fringe appears across a flat surface. Double exposure measurements also correct uneven illumination conditions and tilt.

## **4.2 Detector Noise**

The previous discussion only includes noise from the optical readout system. The detector also contributes to system level noise of the imager. The additional noise contributors at the detector include three sources. Heat exchange between the pixel and environment causes background fluctuations. The exchange of energy between the pixel and substrate causes thermal fluctuations. The exchange of mechanical and thermal energy at the photomechanical pixels causes thermomechanical noise. Image shot noise has been shown to be the dominant contributor to system level noise in infrared imagers with optical readout (Erdtmann et al., 2008). Phase measurement uncertainty will be the most major contributor to noise in an infrared imaging system with an interferometric optical readout.

## **4.3 Experimental Procedure for Verification of Accuracy in PSI**

Accuracy and repeatability are gauged using National Institute of Standards and Technology (NIST) traceable calibration standards as shown in Figure 4.4. These gauges are specifically designed to characterize height measurements. The measured standard has a thin gold layer with step height of  $100\text{nm} \pm 2.5\text{nm}$ . The uncertainty is greater than the needed resolution. The step is small enough so that phase between the top and bottom will not wrap.



Figure 4.4. NIST traceable calibration standard as used to verify the accuracy and uncertainty of measurements made with PSI .

The measurement system is a modified microscope with a 5X magnification Michelson interferometric objective shown in Figure 4.5. The objective is mounted on a P-725.CDD PIFOC. This is a nanopositioner produced by the company Physik Instrumente specifically for microscope objectives. The piezo-electric transducer has a maximum expansion of  $18\mu\text{m}$  at a rate of  $5\text{V}/\mu\text{m}$ . Response time can be as low as 5ms. This sets a limit on camera exposure time. The positioner's controller corrects for hysteresis with closed loop feedback. From manufacturer's specifications, travel remains linear to below  $\pm 0.1\%$  for the full range (Physik Instrumente, 2012a). The object is mounted on a tilt stage to correct for any tilt between the two beams. Illumination is provided by a monochromatic LED and images are captured with CCD or CMOS cameras.

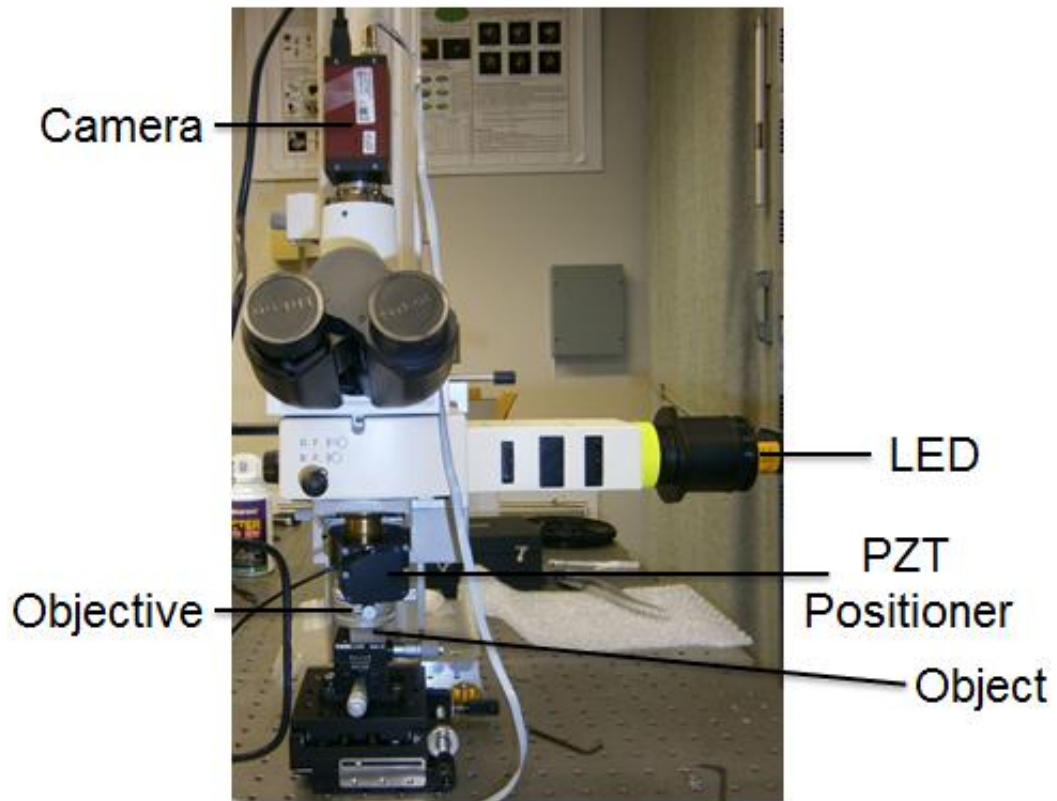


Figure 4.5. Microscope modified for phase-stepping interferometry.

Four different cameras and LEDs are used in these measurements. Table 4.1 provides a comparison of selected specifications for these cameras. The LEDs have the following wavelengths: 455nm, 530nm, 617nm, and 780nm. The Hariharan algorithm is used to determine the correct voltage input to the positioner for each of the illumination sources.

Table 4.1. Cameras utilized for verification of accuracy and uncertainty in PSI

Camera	Pixelink PLA741	AVT Pike F100B	AVT Pike F505B	AVT Stingray F033B
Sensor	CMOS	CCD	CCD	CCD
Resolution	1280×1024	1000×1000	2452×2054	696×494
Pixel Size	6.7×6.7 $\mu\text{m}^2$	7.4×7.4 $\mu\text{m}^2$	3.45×3.45 $\mu\text{m}^2$	9.8×9.8 $\mu\text{m}^2$
Bit Depth	10 Bits	14 Bits	14 Bits	14 Bits
Peak Sensitivity	675nm	515nm	475nm	515nm
Frame Rate	27 FPS	60 FPS	15 FPS	84 FPS

In all experiments, an exposure time of 35ms is used for the measurements. In addition, the intensity of the illumination is adjusted until the brightest portion of the image is nearly saturated.

#### 4.4 Accuracy Results

Accuracy measurements are performed with the 617nm illumination source. The step of the calibration standard is a thin gold layer. The reflectivity of gold is efficient for visible wavelengths greater than approximately 530nm so that 617nm is an effective choice for accurate height measurements. The tilt stage is adjusted to remove tilt between the object path and the reference path. Any remaining tilt is removed in post-processing so that the height map is flat. A height map of the calibration standard step as measured with the system, with out-of-plane displacements in nm, is shown in Figure 4.6.

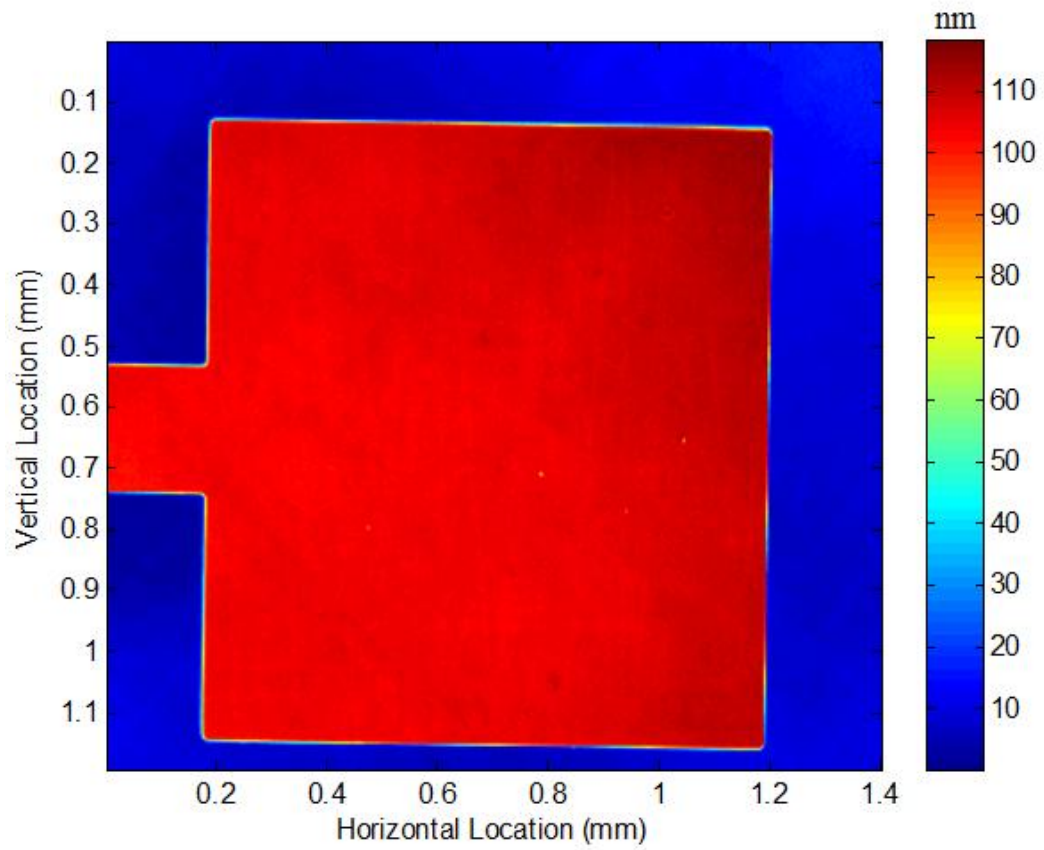


Figure 4.6. Height map of the 100nm calibration standard step with out-of-plane height in nm.

The image histogram of this height map is shown in Figure 4.7. The histogram has two normally distributed peaks. The mean of the lower height distribution is 8.3nm with standard deviation of 0.6nm. The mean of the high distribution is 107.1 with standard deviation of 0.6nm. This corresponds to a step size of  $98.8\text{nm} \pm 1.2\text{nm}$ . This is within the specified step of  $100\text{nm} \pm 2.5\text{nm}$ .

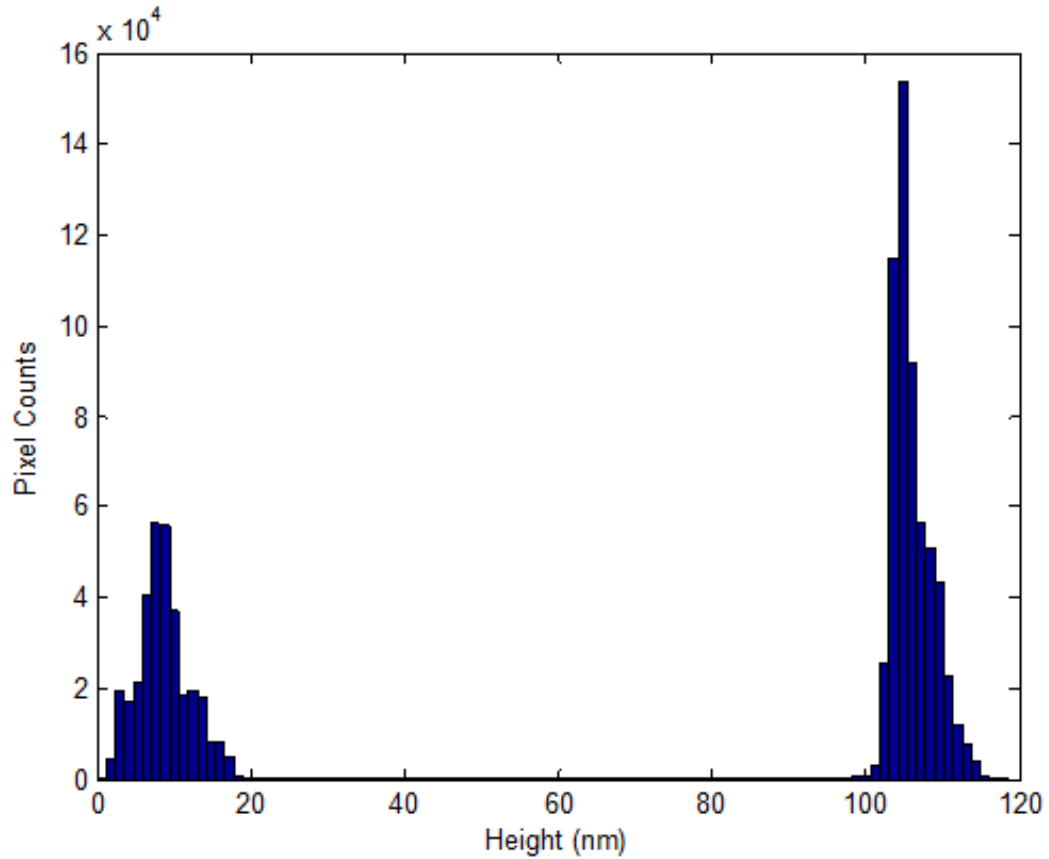


Figure 4.7. Histogram of the height map of the 100nm calibration standard showing a step height of  $98.8\text{nm} \pm 1.2\text{nm}$ .

## 4.5 Repeatability Results

The surface of the calibration standard is flat to within 2.5nm. The calibration standard is thus used as a flat surface to test measurement repeatability. The results of one of these measurements as made with 530nm illumination and the PLA741 camera are shown in Figure 4.8.

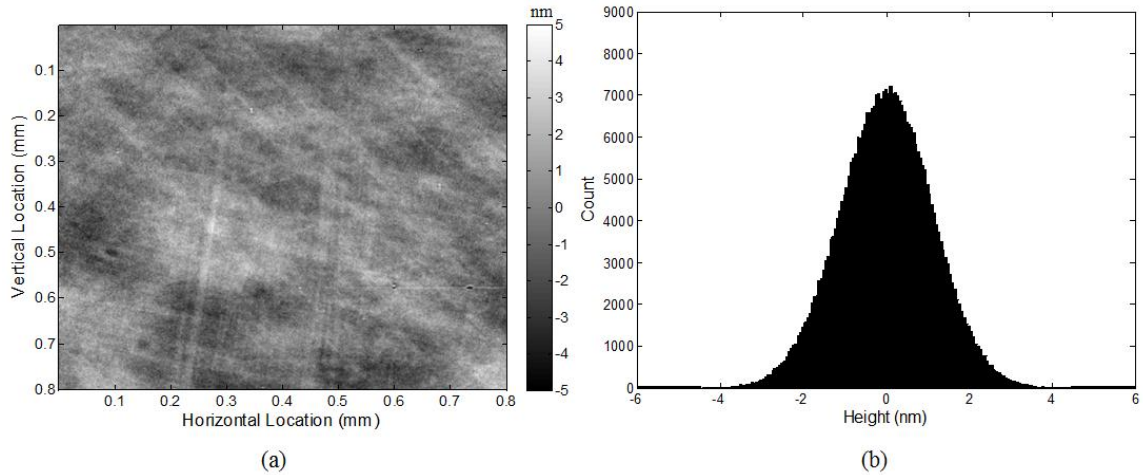


Figure 4.8. Results of a height measurement of a flat section of the calibration standard with no averaging (a) height map; and (b) the image histogram with standard deviation of 1.22nm.

First, the PSI measures a height map of a flat section of the optical flat as shown in Figure 4.8a. The corresponding image histogram is shown in Figure 4.8b. If the uncertainty of the measurement is below the theoretical limit of the camera, then all pixels will have the same height. From the image histogram, this is not the case. The pixel values are normally distributed about a mean value. The standard deviation of the normal distribution quantifies the pixel to pixel spatial uncertainty in the measurement. The uncertainty of the measurement determined as the standard deviation of the flat section is 1.22nm. This corresponds to the total uncertainty of the accuracy measurement and the uncertainty in the flatness of the calibration standard surface.

As previously discussed, the averaging of consecutive frames can reduce noise. Height maps are produced by averaging 1-5 consecutive frames at each stepper position. The averaged image at each phase step is then used to calculate the height map. An

example as measured under the same conditions but with 5 averages per phase step is shown in Figure 4.9. The reduction in spatial noise of the height map after 5 such averages is discernible in Figure 4.9a. The image histogram as shown in Figure 4.9b is narrower and the uncertainty of the measurement is reduced to 1.19nm.

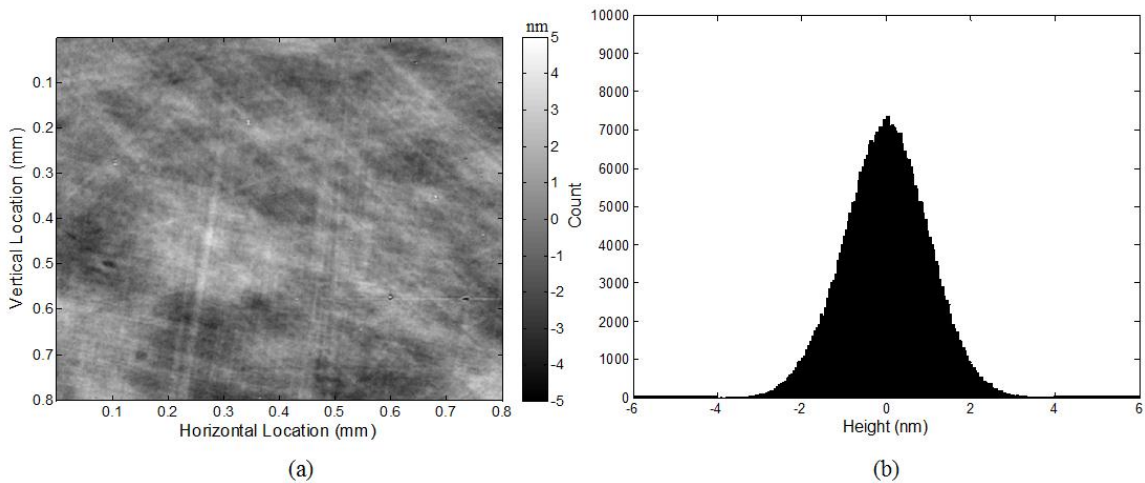


Figure 4.9. Results of a height measurement of a flat section of the calibration standard with 5 averages per phase step (a) height map; and (b) the image histogram with standard deviation of 1.19nm.

Despite the relative flatness of the surface, the height of aberrations on the surface are still of greater magnitude than the uncertainty of the height measurements. A low-pass spatial filter removes the high frequency noise from the image. The low-pass data is subtracted from the original measurement. The result is the high frequency noise due to measurement uncertainty, independent of the shape of the surface. The low frequency aberrations are filtered out to remove the height variations due to the unflat surface and

isolate measurement uncertainty. Only the high frequency aberrations due to the uncertainty of the height measurement remain. Figure 4.10 shows the results under the same conditions as the previous two examples.

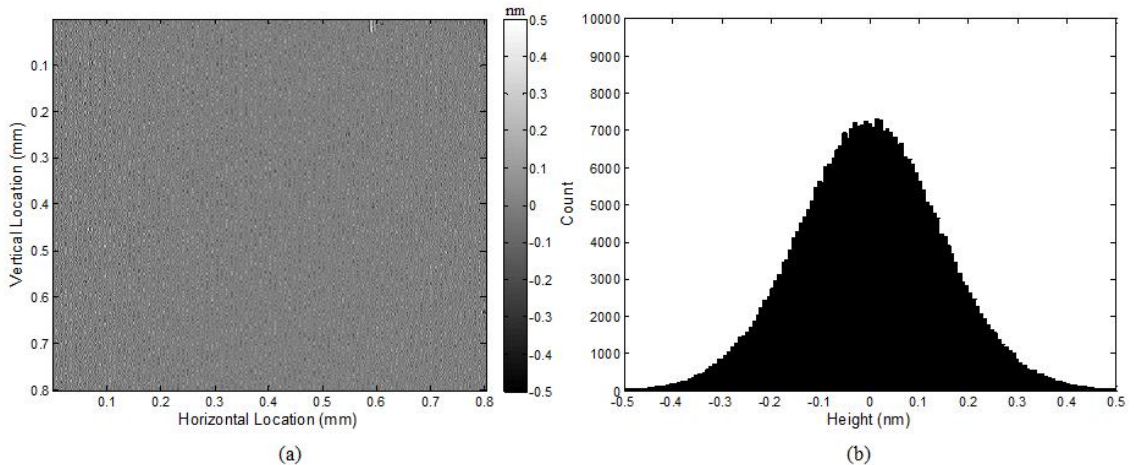


Figure 4.10. Results of a height measurement of a flat section of the calibration standard with 5 averages per phase step and the shape of the surface filtered out; (a) height map; and (b) the image histogram with standard deviation of 0.16nm.

The height map, shown in Figure 4.10a shows the high frequency aberrations due to uncertainty in the measurement. The image histogram is shown in Figure 4.10b. The standard deviation of the histogram is 0.16nm. The spatial uncertainty of the measurement is thus 0.16nm. This is below the target uncertainty of 0.24nm.

The uncertainty, quantified as the standard deviation of filtered height maps, is measured with each of the cameras and illumination sources for comparison. Exposure time is kept to 35ms and illumination is adjusted for consistency between measurements

so that these factors will not contribute to variations in uncertainty. The cameras are adjusted so that the same spatial area of  $0.8 \times 0.8 \text{mm}^2$  of the calibration standard is viewed. The reported values are averages of three trials. Tables 4.2 to 4.4 summarize the results for the uncertainty measurements for each of the cameras and LEDs.

Table 4.2. Uncertainty results from PSI measurements with PLA741 camera.

Number of Averages	455nm Illumination	530nm Illumination	617nm Illumination	780nm Illumination
1	0.36nm	0.32nm	0.33nm	0.30nm
2	0.26nm	0.23nm	0.24nm	0.22nm
3	0.21nm	0.19nm	0.20nm	0.18nm
4	0.19nm	0.17nm	0.16nm	0.15nm
5	0.17nm	0.15nm	0.14nm	0.14nm

Table 4.3. Uncertainty results from PSI measurements with F100B camera.

Number of Averages	455nm Illumination	530nm Illumination	617nm Illumination	780nm Illumination
1	0.27nm	0.27nm	0.28nm	0.32nm
2	0.19nm	0.19nm	0.19nm	0.23nm
3	0.16nm	0.16nm	0.16nm	0.19nm
4	0.14nm	0.13nm	0.14nm	0.18nm
5	0.13nm	0.12nm	0.13nm	0.15nm

Table 4.4. Uncertainty results from PSI measurements with F505B camera.

Number of Averages	455nm Illumination	530nm Illumination	617nm Illumination	780nm Illumination
1	0.53nm	0.47nm	0.70nm	0.52nm
2	0.37nm	0.32nm	0.49nm	0.40nm
3	0.30nm	0.30nm	0.39nm	0.30nm
4	0.27nm	0.28nm	0.35nm	0.26nm
5	0.23nm	0.24nm	0.31nm	0.23nm

For each of the cameras, the uncertainty is lower for measurements made using LEDs with wavelength close to the camera's sensitivity. Temporal averaging reduces the

uncertainty for all trials. Median spatial filtering can reduce the uncertainty further. The reduction in uncertainty decreases with each additional average. The F505B has the smallest pixel size of 3.45 $\mu\text{m}$  and has the greatest amount of uncertainty for all trials. The F100B has the largest pixel size of 7.4 $\mu\text{m}$  and has the smallest amount of uncertainty for all trials. This is expected. An increased pixel size improves the pixel's ability to capture photons and improves signal to noise ratio. An additional test is conducted with the Stingray F033B. This camera has a pixel size of 9.8 $\mu\text{m}$ . The results are presented in Table 4.5. These are the lowest measured values for uncertainty.

Table 4.5. Uncertainty results for PSI measurements with the F033B camera.

Number of Averages	617nm Illumination
1	0.24nm
2	0.18nm
3	0.15nm
4	0.13nm
5	0.11nm

#### 4.6 Conclusions of the accuracy and repeatability measurements

Through measurements of the calibration standard's step height, the phase shifting interferometer has demonstrated accuracy on the nm scale. Proper calibration of the nanopositioner voltage is critical for accurate measurements. The Hariharan algorithm is used for all further calibrations.

Uncertainty is dependent on the camera characteristics. Comparison between the cameras shows that a larger pixel size will reduce spatial uncertainty. Additionally,

averaging of consecutive frames can also reduce uncertainty. The reduction decreases with each consecutive average. No more than 5 averages are needed. The Stingray F033B has the largest pixel size and demonstrated the lowest measured uncertainty. The camera also has a high frame rate of 84 frames per second at full resolution. Therefore, frame averaging can be implemented while still maintaining real-time display rates. The camera however has a low resolution of 696×494 pixels. All of the cameras except for the PikeF505B demonstrated the ability to make measurements with uncertainty below 0.24nm for all trial wavelengths. The Pike F100 is used for future trials because of its low noise, high frame rate, and pixel resolution.

The noise results for the interferometric system only take into account spatial effects. Temporal noise will also contribute to measurement uncertainty. The hypothesis of the current research is to minimize spatial noise through the use of double exposure measurements. With temporal filtering through averaging and no direct spatial filtering, the spatial noise of the measurements made using phase stepping techniques is adequately low to achieve the 0.24nm target noise level.

## 5 The Interferometric Optical Readout System

The MEMS detector is mounted in a long wave infrared (LWIR) lens shown in Figure 5.1. The lens focuses radiation onto the absorptive side of the detector. The germanium lens and the filters allow only long wave infrared radiation to pass onto the array. The lens has adjustable f-number and working distance. The f-number is kept at the smallest value of 0.75 with the aperture fully open to maximize the radiation reaching the array. The working distance is focused as needed for the distance of the object to the array. The optical window of the detector is exposed so that the optical readout system can measure the array. Phase stepping interferometry with a compensation window is an appropriate technique for measuring the displacements of the micromirrors.



Figure 5.1. MEMS detector installed in a custom LWIR lens

## 5.1 Experimental Setup Constraints

A number of constraints define the optical readout system. The magnification needs to be adequate so that enough pixels are visible on each mirror so that the tip can be differentiated from the rest of the mirror. An area of  $20 \times 11$  pixels per mirror is sufficient enough to allow for a up to a  $5 \times 5$  median to be calculated at the tip of the mirror. The working distance of the optical system needs to be greater than the distance from the surface of the optical window to the focal plane array. This distance is around 5mm. The depth of field needs to be greater than maximum height difference in a viewable area. From previous measurements, the maximum height difference in a  $10 \times 8$  section of the array is around  $10 \mu\text{m}$ .

Because of the optical glass on the vacuum sealed package, the setup needs to be able to hold a compensation window on the reference path. The interferometric microscope objective from the accuracy and repeatability tests does not provide means to insert the compensation window into the reference path. The coherence length of the light source needs to also be greater than the maximum height difference so that modulation will occur across the entire viewable area. Additionally, the reflective surface is gold and thus the wavelength of the illumination source needs to have good reflectivity on gold surfaces. Ideally, the camera will have peak sensitivity at the selected wavelength. The cameras need bit depth greater than 8-bits so that measurement resolution is below  $0.24 \text{nm}$ .

## 5.2 Interferometer

The optical readout employs a Linnik configuration interferometer. The configuration is nearly identical to a Michelson interferometer. The difference is that the same measurement optics in the object path is duplicated in the reference path. In this case, identical objectives and windows appear in both the reference and objective paths. The interferometer is mounted on an optical table to dampen vibrations from the environment. The interferometer is assembled using a cage system. This modular system has rigid steel rods on which optical components can be mounted along the same axis. This allows for increased flexibility in component selection and adjustment. The assembled system is shown in Figure 5.2.

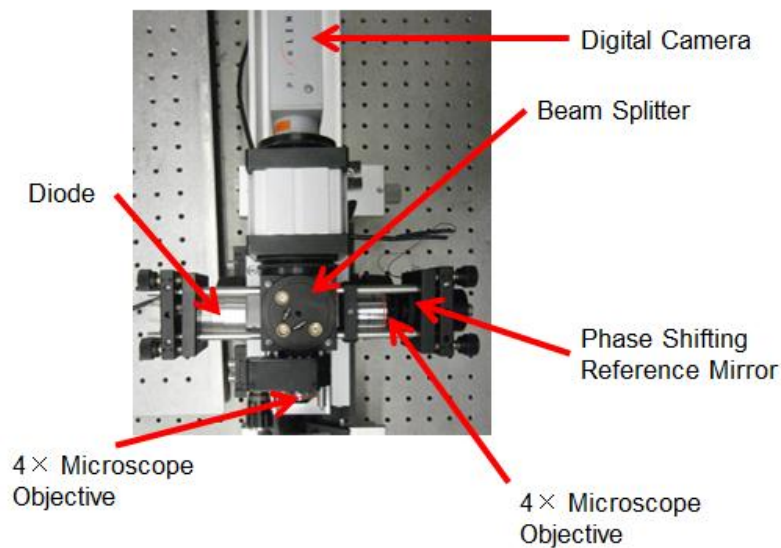


Figure 5.2. The Linnik interferometer used in the optical readout system.

### **5.2.1 Microscope Objectives**

A 4X microscope objective is located in both the reference and object beams of the interferometer so that that same magnification is applied to both paths. These objectives have a working distance of 30mm. This allows for the focusing of the object beam on the array while maintaining a gap between the objective and the optical window. The working distance also leaves sufficient space between the reference mirror and the other object so that the compensation window can be inserted. The depth of field is 55.5 $\mu$ m. This is greater than the maximum height difference of 10 $\mu$ m. The entire in view portion of the array can appear in focus at the same time.

### **5.2.2 Illumination Source**

The illumination source is a monochromatic LED with specified wavelength of 620nm. The reflective surface of the array is gold. Reflectivity of gold is over 98% in the visible spectrum for wavelengths greater than 550nm. The wavelength of 620nm takes advantage of this high reflectivity so that the majority of the light that hits the array will be reflected back to the camera.

### **5.2.3 Piezo-Electric Transducer**

The reference mirror is mounted on a Physik Instrumente P-830.10 piezo-electric transducer. The travel range is 15 $\mu$ m (Physik Instrumente, 2012b). The transducer receives a signal from the computer through a National Instruments data acquisition

device (DAQ). With no closed loop feedback to correct for hysteresis, the careful voltage calibration through the Hariharan algorithm is critical.

### 5.2.4 Compensation Window

The compensation window is exactly the same material and thickness as the optical window of the vacuum sealed package. The compensation window needs to be located on the same side of the microscope objective as the optical window. Otherwise, the optical path length difference introduced by the optical window will not be corrected. The window is mounted on a custom machined plate shown in Figure 5.3a and inserted into the reference path of the interferometer as shown in Figure 5.3b.

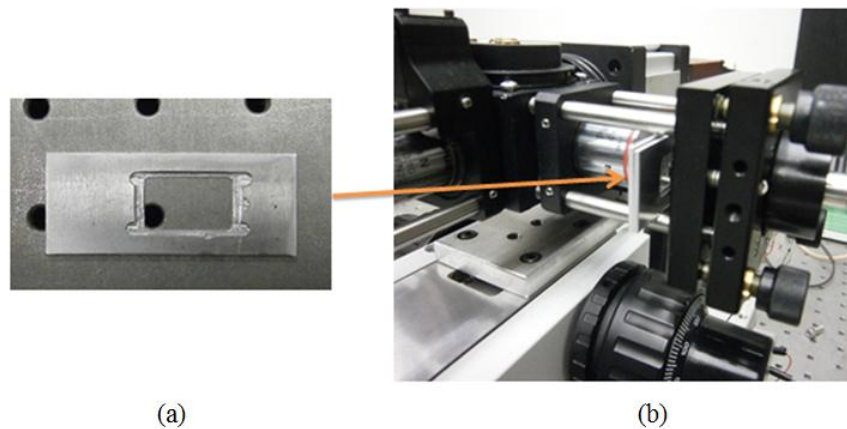


Figure 5.3. The compensation window mount: (a) the custom machined mount; and (b) the mount inserted between the objective and reference mirror.

### **5.2.5 Cameras**

The Pike F100B is used with the optical readout system. It has peak sensitivity at 515nm. Although the peak sensitivity does not match the illumination source of 620nm, the large pixel size and high frame rate will keep noise low. Additionally, from Table 4.3, spatial measurement uncertainty does not change by more than 1nm between measurements taken at 530nm and 617nm.

The Pike F100B has a spatial resolution of 1000×1000 pixels. The viewable area with 4X magnification is 1.9×1.9mm<sup>2</sup> or 40×40 mirrors. This is on the order of 2% of the entire array. Each mirror is comprised of 22×10 pixels. For comparison, the PLA741 has a spatial resolution of 1280×1024 pixels. The viewable area with 4X magnification is 2.1×1.7mm<sup>2</sup> or 75×60 mirrors. The F033B has a spatial resolution of 656×492 pixels. The viewable area with 4X magnification is 1.6×1.2mm<sup>2</sup> or 35×25 mirrors.

### **5.3 Assembled Infrared Imaging System**

The assembled infrared imaging system with interferometric optical readout is shown in Figure 5.4. The system is mounted horizontally so that the full range of the LWIR lens depths of field will be available. The aperture is kept fully open with numerical aperture value of 0.75. The LWIR lens is mounted along the object path of the interferometer. It is on a tilt stage so that tilt can be corrected. The interferometer is mounted on a rail so that the focus of the object path can be adjusted.

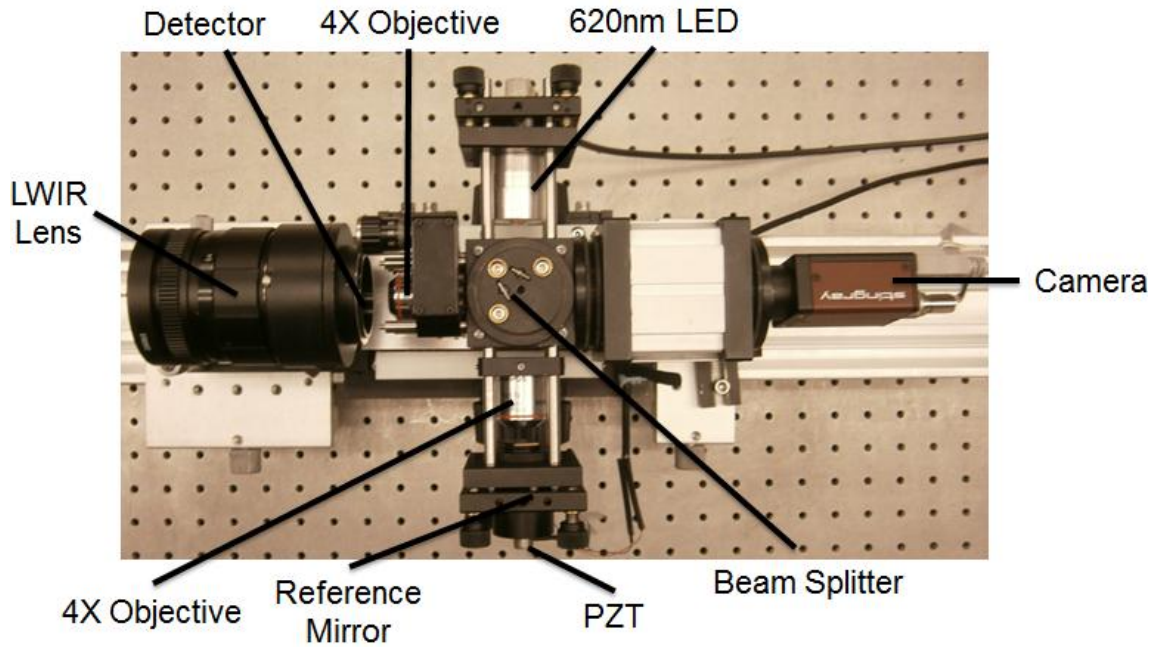


Figure 5.4. The complete infrared imaging system showing the configuration of the individual components.

## 5.4 LaserView Software

LaserView is an in-house developed software package designed specifically for real-time interferometric measurements. The software is versatile enough to integrate with shearography and fringe projection measurements in addition to microscopy (Harrington, 2009). A brief description of relevant features follows. Figure 5.5 shows the view selection portion of the LaserView user interface. Live view is the direct video stream from the digital camera.



Figure 5.5. View selection window in LaserView.

Figure 5.6 shows an interferogram as viewed in LaserView of a  $1.9 \times 1.9 \text{ mm}^2$  section of the MEMS array captured with the setup described in section 5.3 with fringes appearing only on the mirror surface

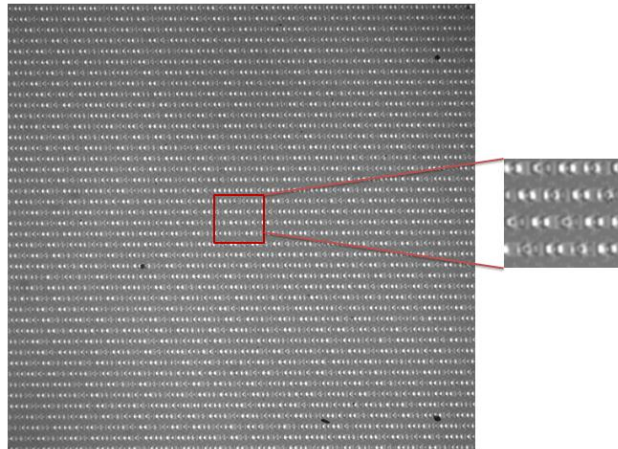


Figure 5.6. Interferogram of a  $1.9 \times 1.9 \text{ mm}^2$  section of the MEMS array as displayed in LaserView with a close-up view to show the formation of fringes only on the mirror surfaces.

LaserView employs the four-step phase stepping algorithm discussed in Section 2.1.2. If one of the paths is phase stepping, the fringes will appear to flow across the interferogram in a looping pattern. The Time Averaged view displays the calculated modulation from phase-stepped interferograms in real time. A modulation image of the micromirror array as calculated by LaserView is shown in Figure 5.7. The sections of the modulation image with high fringe contrast between frames have a high value and appear white. The sections of the image with low or no modulation have low values and appear dark. In this case, the mirrors appear bright while the substrate is dark.

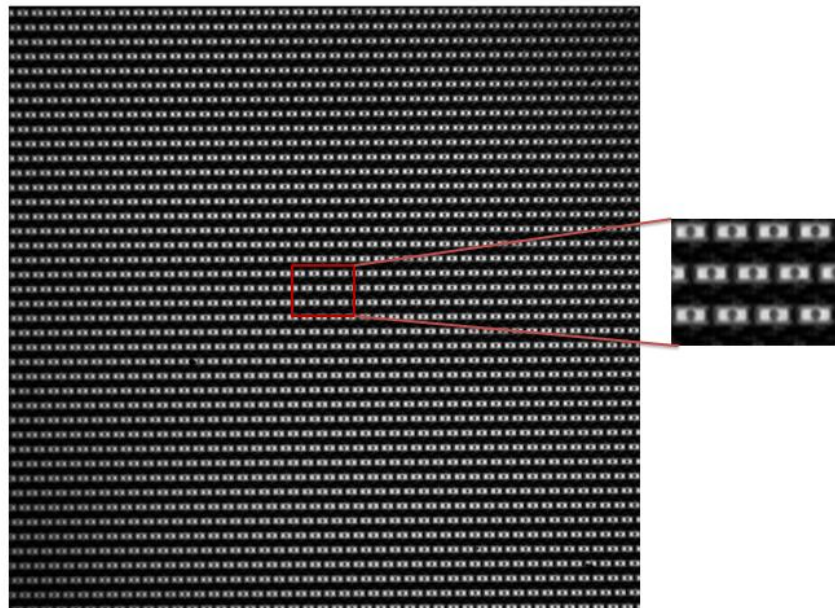


Figure 5.7. Modulation image of a  $1.9 \times 1.9 \text{ mm}^2$  section of the MEMS array as displayed in LaserView with a close-up view to show the peak modulation occurring only on the mirror surfaces.

Double Exposure View displays the calculated optical phase map in real-time. In double exposure, all subsequent images are subtracted from a reference image so that changes from the reference image can be measured. A new reference can be taken at any time and the reference can be turned on and off. Figure 5.8 is an example of a phase map of a  $1.9 \times 1.9 \text{ mm}^2$  section of the MEMS array without the reference image. The substrate shape is visible across the array and the optical phase wraps across individual mirrors.

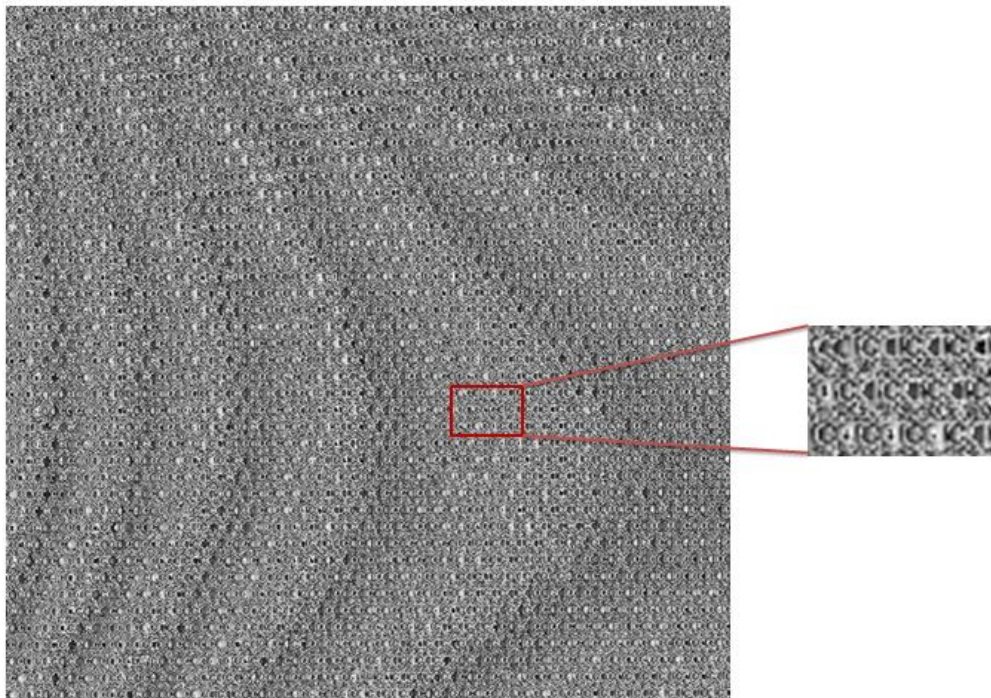


Figure 5.8. Phase map of a  $1.9 \times 1.9 \text{ mm}^2$  section of the MEMS array as displayed in LaserView with the deformation of the substrate visible. The close-up shown the optical phase patterns across individual mirrors

Figure 5.9 is the double exposed phase map with the current image subtracted from a reference image. Because no loading of the array has occurred since the capture of the reference, the double exposed phase map is flat at modulating sections of the field-of-view. The sections of the array with low modulation do not have a consistent calculated optical phase and have random values. Only changes from the reference will be measured. The shape of the substrate and the wrapping across mirrors will not impact the measurements. The double exposed phase map will show changes in phase in comparison to the reference image.

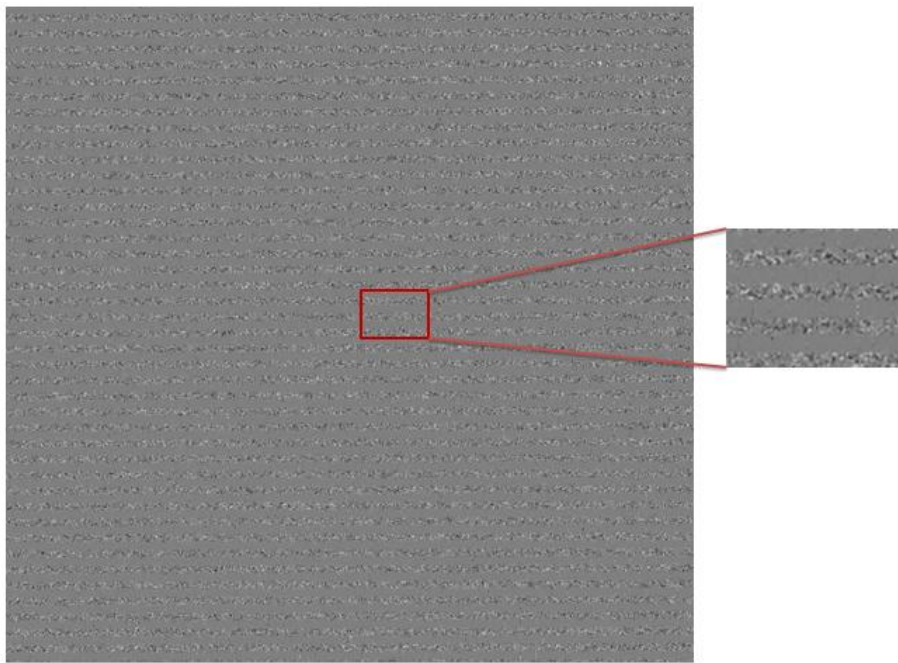


Figure 5.9. Double exposed phase map of a  $1.9 \times 1.9 \text{mm}^2$  section of the MEMS array as displayed in LaserView with a reference phase map and no loading. The close-up shows the flat phase of the mirrors and the random phase on sections with no modulation

Figure 5.10 shows LaserView's image export options into RTI format. RTI is a nonstandard, bitmap based image format that can store the four phase-stepped images, so that the calculated phase and modulation images can be displayed. Lvvid files are composed of a user-defined number of frames of consecutive RTI images. RTI and Lvvid files are openable in HoloStudio. HoloStudio allows for post-processing of these files with techniques including filtering, unwrapping, and scaling. Any of the view types can also be exported in several different standard image formats

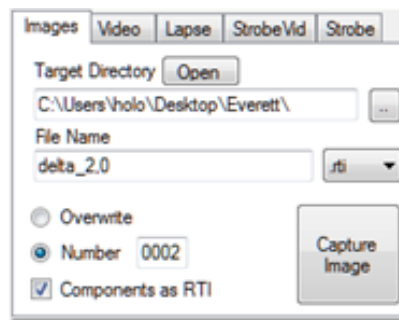


Figure 5.10. Image export in LaserView with RTI as the selected image format.

Figure 5.11 shows LaserView's camera and shifter control options in the user interface. From here the user can specify exposure time and shifter voltage. Additionally, LaserView can carry out shifter calibration and calculate an appropriate exposure time based on the desired framerate.

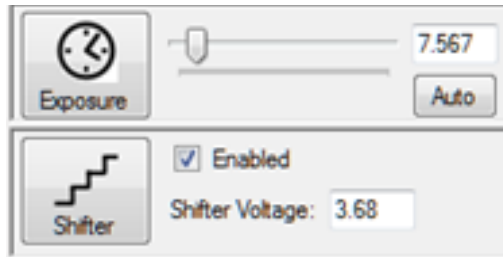


Figure 5.11. LaserView camera and phase-shifter control.

The camera exposure time can be adjusted directly or the user can define a desired frame rate and the exposure time will be automatically adjusted. The shifter voltage specifies the needed voltage to produce the  $\pi/2$  phase step.

LaserView can expedite voltage calibration through the use of the Hariharan algorithm. This feature allows the user to specify a range of voltages to run the Hariharan algorithm. The software then gathers the 5 needed images and calculates the phase. This is repeated for each voltage as specified and the results are exported to a spreadsheet. From this spreadsheet, the user can see which voltage produces most nearly the correct phase-step.

## 5.5 Demonstration of Real-Time Displacement Measurements

Heat from soldering-iron is used to create a response on the array. The iron has an at the scene temperature over 470K. One of the resulting phase maps is shown in Figure 5.12. The shape of the iron is visible in the deformations. A phase difference can be observed between the hotter and cooler sections of the iron. This response is large enough

to be visible by observation of the phase map. A number of unresponsive pixels can also be observed. The phase map updates in real-time based on the current location of the soldering iron. Because response reaches a maximum at one end of the mirror, a response corresponding to a temperature change of 100mK will not be visible in the double exposed phase map. Because of the double exposure method, the height variations in the mirrors are independent of spatial characteristics of the detector.

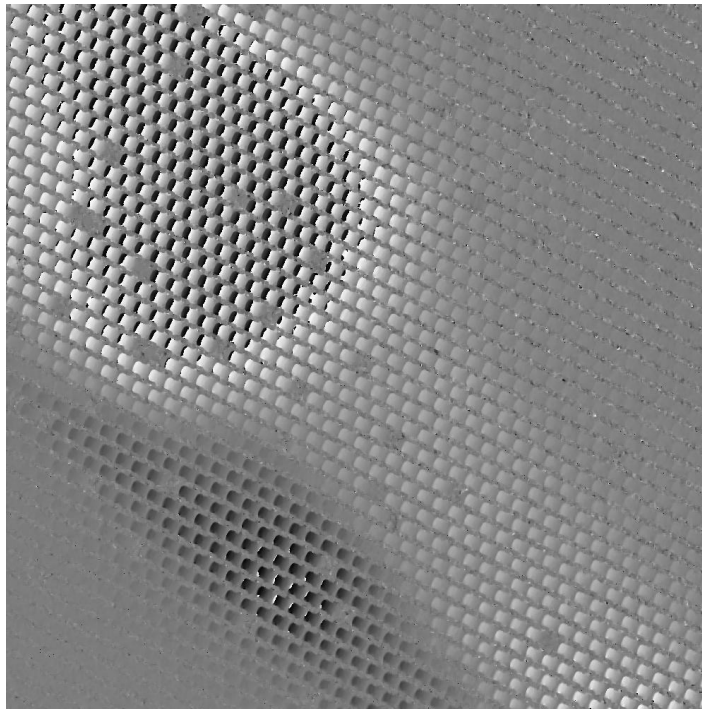


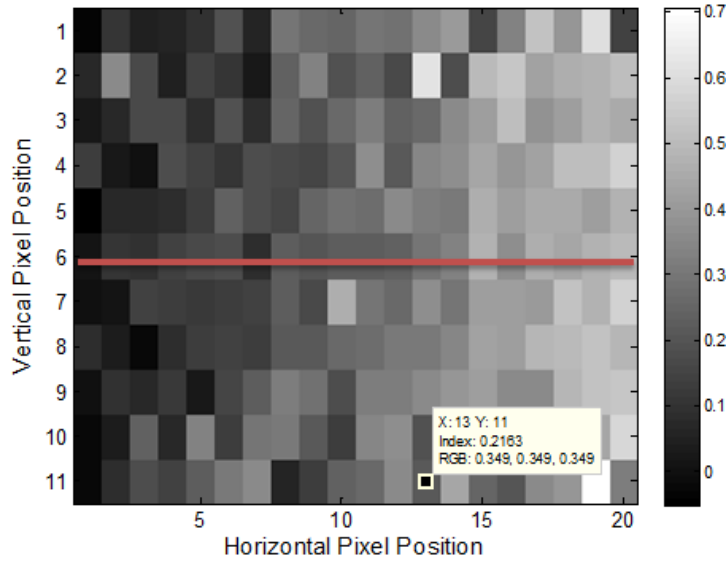
Figure 5.12. Double exposed phase map showing mirror displacements from soldering iron heat input.

## **6 Algorithm for Real-Time Infrared Imaging**

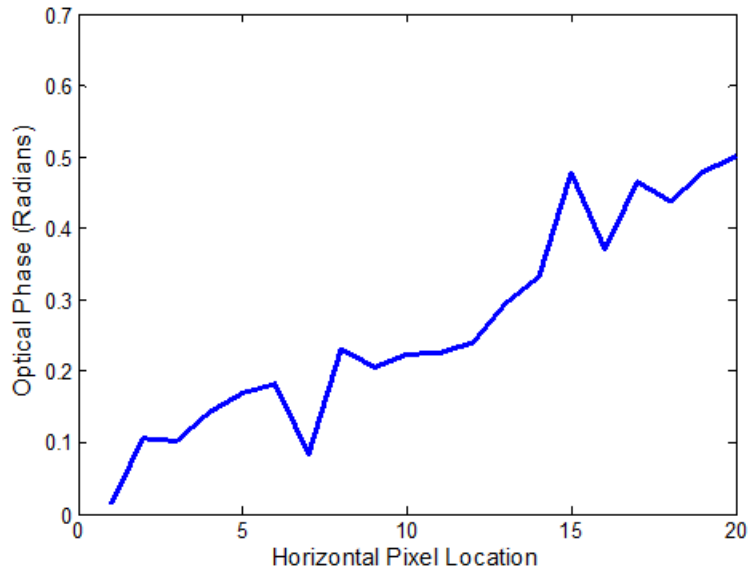
The optical readout system has demonstrated its ability to display real-time response of the detector. An algorithm is now needed to measure the change in tip displacement and display these values as a thermogram.

### **6.1 Algorithm Description**

The mirrors in the focal plane array tilt as a function of scene temperature. As a result, the out of plane phase change is not consistent across an entire mirror. This is demonstrated in Figure 6.1. Figure 6.1 (a) is an optical phase map of a single mirror in the array experiencing a thermal loading corresponding to an increase in temperature at the scene of approximately 15K from the temperature corresponding to the reference phase map. The mirror tilts as a function of the change in temperature at the scene. Responsivity in terms of height change is at a maximum at one tip of the mirror. The minimum height change is located to the left side of the mirror centroid. The height change increases linearly across the x-direction of the mirror and reaches a maximum at the right-most tip. The plot of height changes across a cross section of the mirror, as shown in Figure 6.1 (b), is not smooth as a result of the spatial uncertainty in the optical phase measurements. To maximize the detector responsivity, an algorithm is needed to extract the maximum height change of each mirror in the array.



(a)



(b)

Figure 6.1. Response of a single mirror: (a) Optical phase map of a single mirror from a change in thermal load corresponding to approximately 15K; and (b) a plot of the optical phase values of a cross-section of the phase map showing the tilt of the mirror. The base of the mirror is on the right and the tip of the mirror is on the left where maximum displacement is observed

The algorithm has been developed as an addition to LaserView's existing capabilities. Figure 6.2 provides a flow chart of the infrared imaging algorithm from image acquisition through thermogram display. A description of each step follows and corresponding MATLAB code is included in Appendix A.

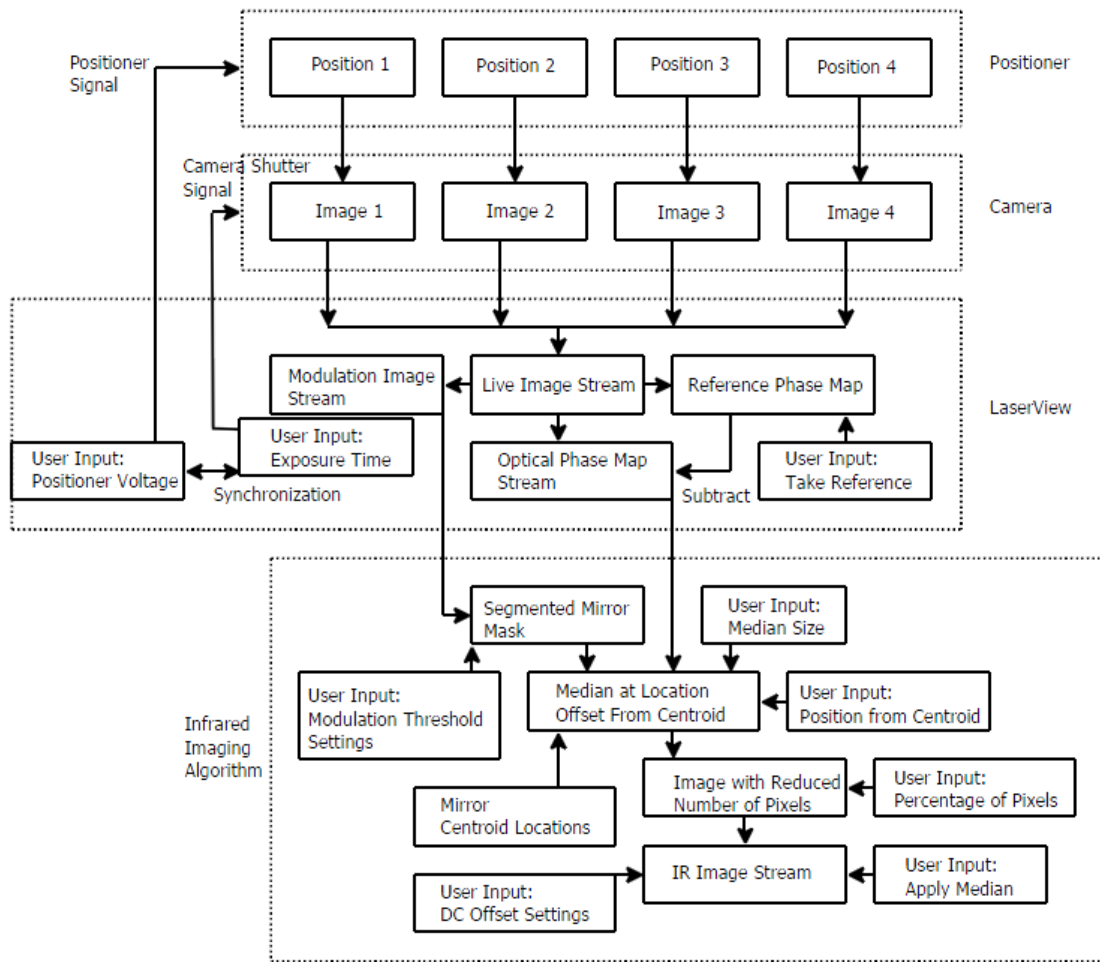


Figure 6.2. Flow diagram of image processing starting with image acquisition of 4 phase-stepped interferograms, to the calculation of the phase map and modulation image through LaserView and finally through the creation of real-time infrared images based on data calculated in LaserView.

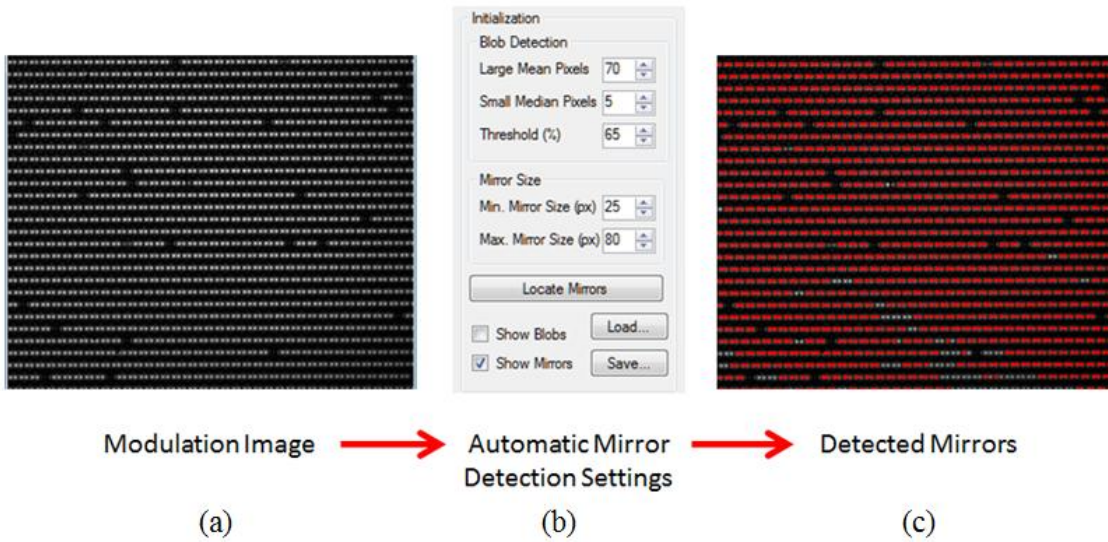


Figure 6.3. Automatic mirror detection with algorithm: (a) modulation of the mirror array as calculated by LaserView; (b) the modulation threshold parameters as set in LaserView; and (c) the location of the mirrors as determined by the algorithm.

LaserView controls piezo and camera signals to collect Phase-stepped interferograms. From the interferograms, modulation and optical phase maps can be displayed in real-time. The algorithm identifies the locations of each of the modulating mirrors through image segmentation. This is based on the time average or modulation view shown in Figure 6.3a. Parts of the image with the best fringe contrast will display the greatest modulation values. Areas of the image with reduced or no fringe contrast between phase-stepped frames have low values. The algorithm identifies regions with a user defined thresholds of modulation as shown in Figure 6.3b. From the modulation image, a mask is created with pixels above the threshold assigned a value of 1 and pixels below the threshold assigned a value of 0. An image segmentation algorithm identifies the continuous regions in the mask image that have a value of 1. The algorithm records

the size of each region and the centroid of each region. Each region corresponds to the location of a mirror. The user can specify a region size so that regions that are too small or too large to represent a mirror are excluded. Figure 6.3c visually shows the locations of regions corresponding to mirrors as determined by the algorithm.

Figure 6.4 represents a mirror encompassing  $17 \times 6$  pixels. Each pixel, represented as a square, has a corresponding height change value calculated from the double exposed phase map. As shown in Figure 6.1, the phase change values will be greatest at the tip. The centroid is marked in the center of the diagram. The user then inputs the number of pixels away from the centroid at which mirror tilt will be calculated. This location is marked to the left of the diagram. The value for the pixel is then a user defined median around that pixel. The median value reduces the probability of an outlier value being selected to represent the pixel. The pixels for a  $3 \times 3$  median are marked on the diagram. Only a small number of the total pixels on the mirror are used in the calculation.

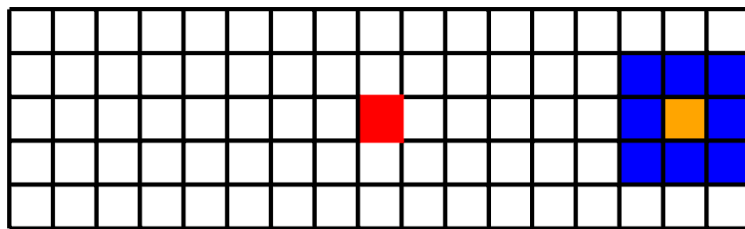


Figure 6.4. Measurements of a mirror with  $17 \times 6$  pixels; the value associated with the mirror is the median value of a  $3 \times 3$  section located a distance of 7 pixels to the right of the centroid. The number of pixels used in the measurement is set by the optical magnification of the system

Each mirror has a single value associated with it from this median. The value is displayed at the corresponding mirror centroid location as determined from the image segmentation of the modulation image. All other pixels have no value. This is shown in Figure 6.5.

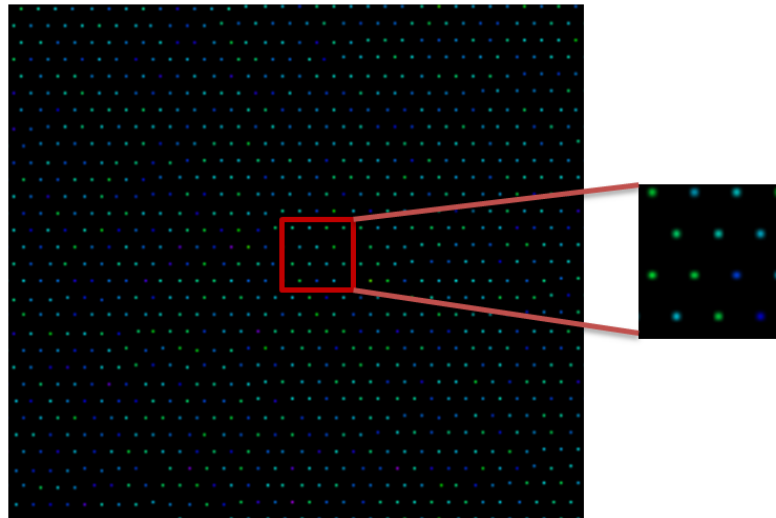


Figure 6.5. The single median value calculated for each mirror is placed at a position corresponding to that mirror's calculated centroid.

For display and calculation purposes, the total number of pixels is reduced by a user-specified percentage to reduce the gap between pixels as shown in Figure 6.6. This improves the clarity of the image by increasing the number of useful pixels in comparison to the number of empty pixels.

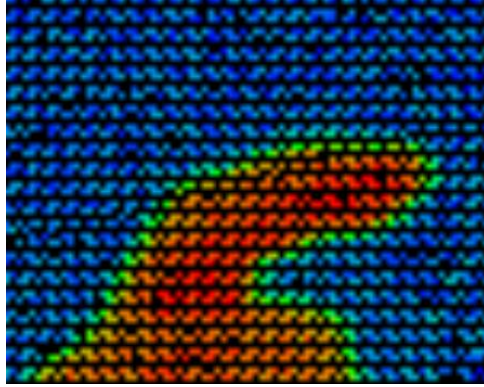


Figure 6.6. A representative thermogram of a finger as produced by the imaging algorithm with the total number of pixels reduced to remove the gaps between known pixels.

The algorithm can interpolate to fill in the missing pixels and apply a median filter to smooth out the final image. Figure 6.7 shows a smoothed thermogram of a finger.

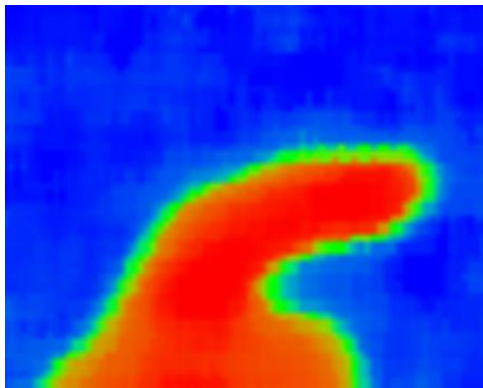


Figure 6.7. A representative thermogram of a finger as produced by the imaging algorithm that has been filtered to remove all gaps.

The warmest regions of the image, the finger, are one shade. The cooler background with little to no phase change is a different color. Pixels on the border of the image are partially on the finger and partially on the background. This leads to the border having a value between the two regions. Thus, the border appears as an intermediate shade.

Computed thermograms only display relative phase values. The MEMS detector does not include an absolute reference surface. All of the modulating areas deform with temperature. The optical readout system can only measure a relative change in phase and thus temperature. Because of positioner hysteresis and environmental instability, the image drifts temporally leading to a flickering effect in the thermogram video stream. The user has the option to define the location of a DC offset. The phase at this location is set to zero and subtracted from all other locations. This helps to correct temporal variations not related to camera uncertainty. The algorithm is robust enough to calculate and display the thermograms at nearly the same rate that LaserView displays the corresponding phase map. The algorithm can also correct for unequal illumination in the thermogram images and save files or videos of the thermograms in the RTI format. The color scale can be manually adjusted or set to auto adjust so that the full range of colors is displayed in each frame. The color map for the scale can be changed between one of several options depending on user preference. The user interface for the infrared imaging functions in LaserView is shown in Figure 6.8.

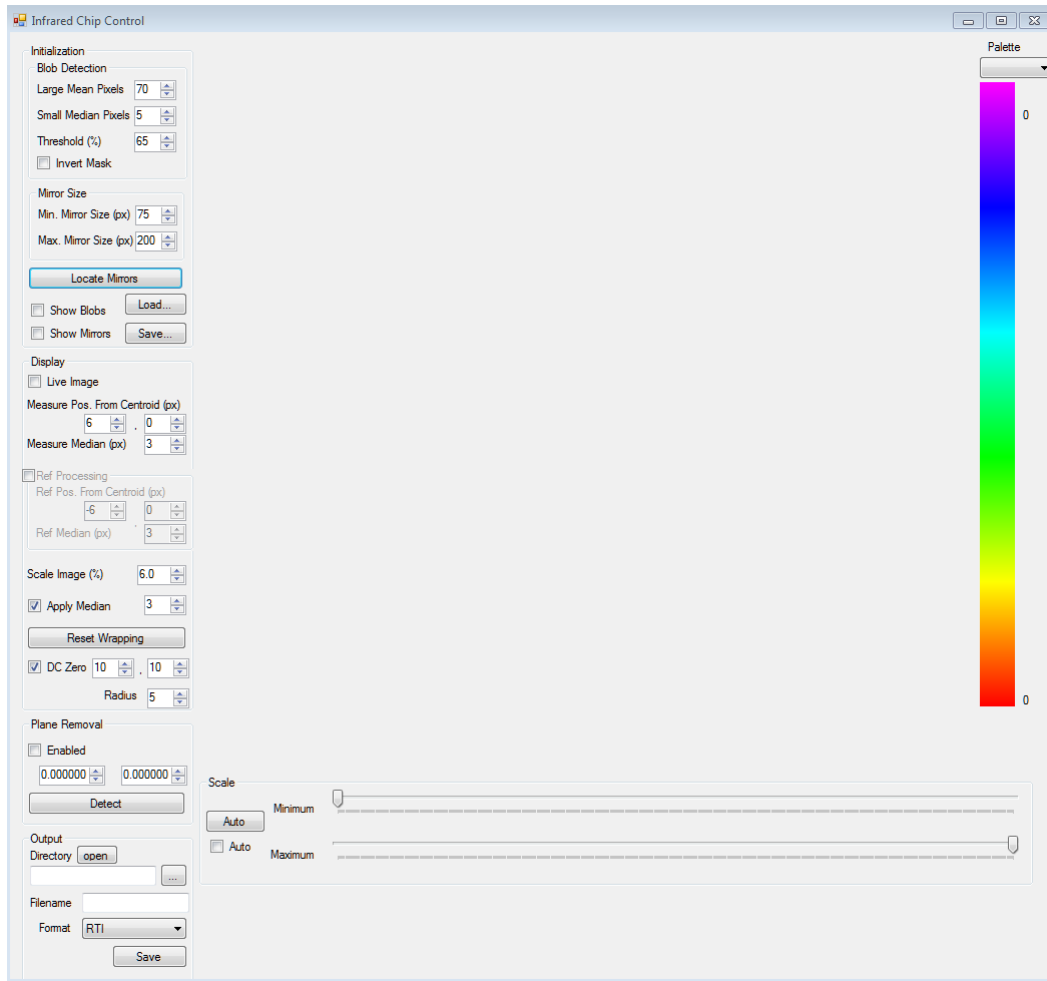


Figure 6.8. The complete LaserView infrared imaging user interface; the thermogram displays at the center of the window.

## 6.2 Demonstration of Real-Time Infrared Imaging Abilities

The imaging system with Pike F100B camera is compared to the commercially available FLIR A225. Relevant figures of merit of each are presented in Table 6.1. In the case of the optical readout, the pixel resolution, bit depth and connection are dependent on the camera and can change depending on the camera type. Both systems operate in the

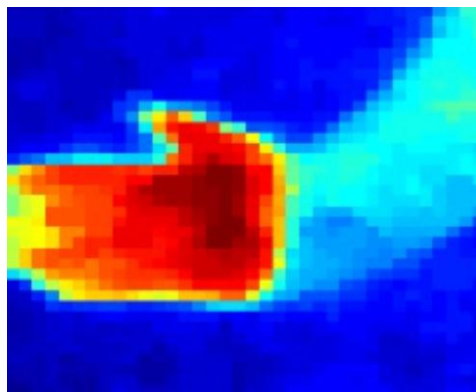
long wave infrared range. Because of the small number of pixels viewed by the optical readout system, the thermograms from the interferometric optical readout appear pixelated in comparison to the images produced by the FLIR system. The field-of-view is also much smaller and objects need to be viewed from a greater distance to fit onto the display. The NEDT of the FLIR system is even lower than the target NEDT and can thus provide visualizations for judging the quality of images produced with the optical readout system.

Table 6.1. Comparison of the FLIR A325 to the imaging system with Pike F100.

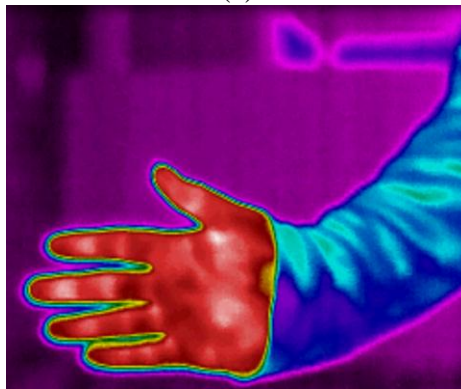
IR Imaging System	FLIR A325	Interferometric Readout
Detector Type	Uncooled Micro-Bolometer	Uncooled Opto-Mechanical Array
Connection	Gig-E	Firewire B
Bit Depth	14 Bits	14 Bits
Pixel Resolution	320×240	38×38
Spectral Range	8-13μm	8-13μm
NEDT	70mK	-

Figure 6.9 provides an example of a thermogram of the same subject at the same time produced by the FLIR and by the system with interferometric optical readout. The interferometric system is located 5m away from the subject while the FLIR camera is 1m for a field-of-view of approximately  $0.3 \times 0.3 \text{m}^2$ . Because of the low pixel resolution, the system with interferometric readout needs to be placed at a greater distance to maintain a field-of-view comparable with the FLIR camera. Each image is set to use the full dynamic range of colors for the measured heat distributions. The FLIR has greater spatial resolution. Despite the reduced spatial resolution due to the pixelation, the interferometric system as shown in Figure 6.9a detects similar relative heat distributions across the hand

and shirt as the FLIR camera, as shown in Figure 6.9b. Additionally, both systems generate these images in near-real time. The temperature difference between the skin and hands is on the order 20K as measured by the FLIR camera. This shows that the temperature resolution of the interferometric readout system can reliably measure temperature distributions with differentials lower than 20K.



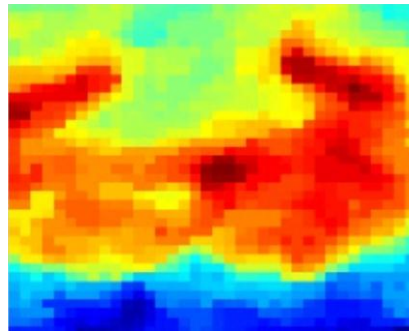
(a)



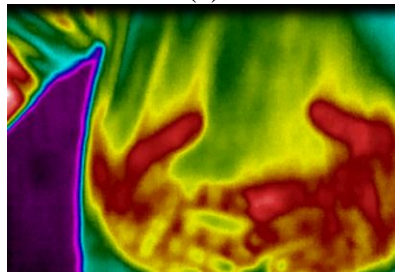
(b)

Figure 6.9. Real-time thermograms of an arm showing similar relative temperature distributions (a) as produced by the interferometric readout; and (b) the FLIR camera with a temperature difference of around 20K between the skin and sleeve as measured by the FLIR camera.

Figure 6.10 (a) displays a thermogram of a shirt as produced by the interferometric readout system and Figure 6.10 (b) displays a thermogram as produced by the FLIR camera. The field-of-view is the same as the previous example. Prior to this scene, the subject's hands are resting across the surface of the shirt. For several seconds after the hands are removed, the shapes of the hands are still clearly visible in the heat distribution. The temperature difference between the shirt and hand pattern as measured by the FLIR camera is around 5K. This demonstrates the interferometric readout systems ability to measure temperature distributions with differentials lower than 5K.



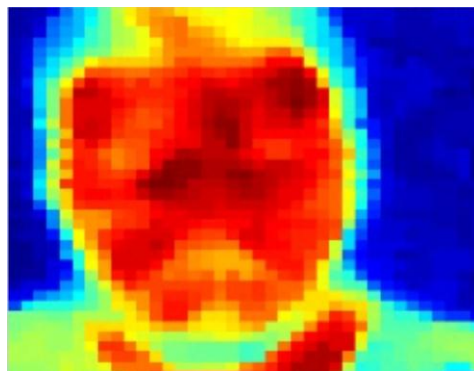
(a)



(b)

Figure 6.10. Real-time thermograms of a shirt (a) as produced by the interferometric readout and (b) the FLIR camera with temperature difference of 5K between the shirt and the hand prints.

Figure 6.11 (a) shows thermograms of a portrait as produced with the interferometric readout. Again, although spatial resolution is low, the image produced with the interferometric readout detects temperature variations across the face from facial hair, eyes, nose, haircut and skin that are also visible in the thermogram produced by the FLIR system shown in Figure 6.11 (b).



(a)



(b)

Figure 6.11. Real-time thermograms of portraits (a) as produced by the interferometric readout; and (b) the FLIR Camera with temperature difference of around 0.6K between the skin and eyes as measured by the FLIR.

Because of the limited spatial resolution, shape details are not defined. Although spatial resolution between the two systems is not similar, the capabilities of detecting temperature variations are comparable. As a point of reference, the temperature differential between the skin and warm area of the eyes is around 0.6K as measured by the FLIR system. This temperature difference is visible in both images. This demonstrates the interferometric readout system's ability to measure temperatures with resolution below 1K.

The spatial quality of the thermograms produced by the interferometric optical readout system improves for objects viewed closer to the lens. As shown in Figure 6.12, the shape of a wrist watch in this thermogram is well defined.

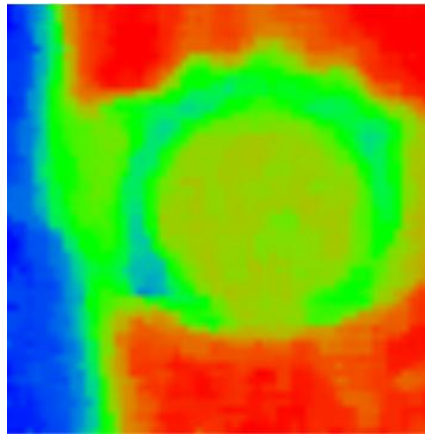


Figure 6.12. Thermogram of wrist watch as produced by the interferometric readout system demonstrating its ability to show small details through measured temperature distributions

Temperature variations between different components of the watch such as the band, rim, and face, as well as between the watch and the wrist are clearly visible. The subject is 2m away from the imaging system and the field-of-view is approximately  $0.1 \times 0.1 \text{m}^2$ .

Figure 6.13 is a thermogram of three fingers with a field-of-view of approximately  $0.1 \times 0.1 \text{m}^2$ . The small temperature variation between the skin of the finger and the fingernail is visible. A different color map is used so that the temperature difference is more easily observed. The temperature difference between the skin and nails is approximately 0.4K as determined from observations with the FLIR system. This demonstrates the system's ability to measure temperature distributions with differentials lower than 0.5K.

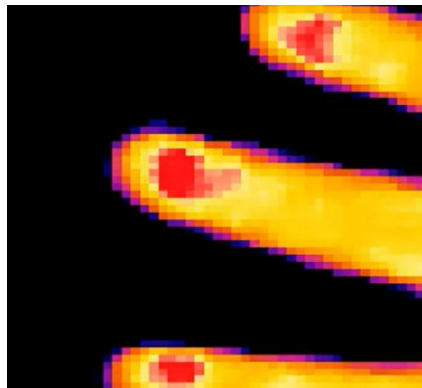


Figure 6.13. Thermogram of three fingers and fingernails with temperature differential of on the order of 0.4K between the skin and nails.

### **6.3 Conclusions of the Real-Time Imaging Demonstrations**

Because of the low spatial resolution of the system with interferometric optical readout and the resulting loss of details, comparisons with the FLIR are difficult to make. This can be improved by increasing the field-of-view of the interferometric readout system so that more mirrors are used in the calculation of thermograms. Despite this, temperature differentials as small as 0.4K as measured with the FLIR are visible in the thermograms produced by the optical readout system. The system has demonstrated the ability to produce real time infrared images with temperature resolution comparable to the FLIR camera. Comparisons of thermograms produced with the optical readout system to thermograms produced with the FLIR system only provide estimated values of the NEDT.

## **7 Evaluation of System Performance**

The ability of the system to produce real-time infrared images has been demonstrated. The next step is to characterize the quality of these images by calculating NEDT. The target NEDT is 100mK.

### **7.1 The Blackbody Target Projector**

Differential blackbodies are used to test thermal imaging systems that are sensitive to small changes in temperature at the scene. A Santa Barbara Infrared 14000Z differential blackbody projector is used to test NEDT. The blackbody produces a differential temperature between an ambient surface and the blackbody emitting surface. A temperature probe measures the ambient surface temperature so that the temperature differential remains constant. The target feature maintains the temperature of the blackbody while the target body maintains the ambient temperature. A target is a solid disk of copper with slots or holes machined out to form the shape of the target feature. The target has a black coating that provides an emissivity that is nearly equal to 1.0. The 14000Z has a target wheel with 12 selectable targets. The target created by the projector has temperature controllable to 0.001K and displays as either a half circle or full circle. The collimator projects an image of the target to the infrared imager as shown in Figure 7.1 (Santa Barbara Infrared, 1999).

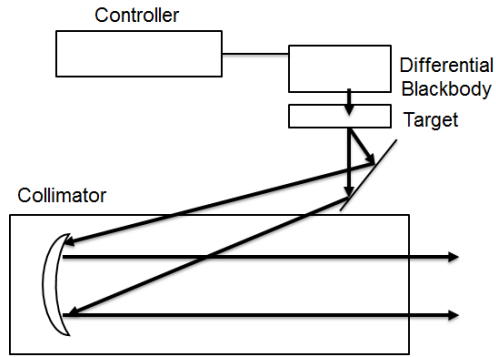


Figure 7.1. Diagram of the blackbody projector components (Santa Barbara Infrared, 1999).

Because the image is collimated, the target will appear as the same size no matter how far the imager is positioned. These targets are designed to provide uniform background with high thermal stability. The infrared imaging system with the thermal imager is shown in Figure 7.2.

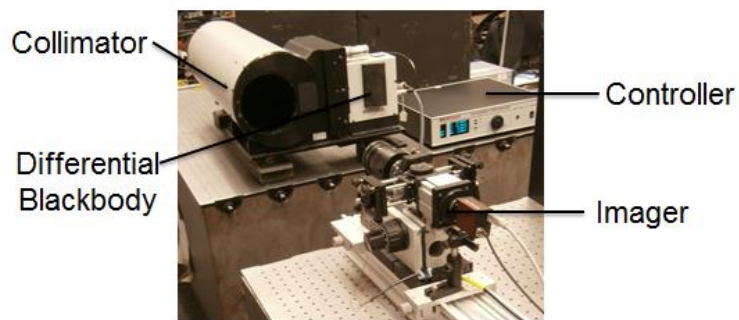


Figure 7.2. The imaging system focused on the blackbody target.

For accurate testing, the collimator needs to be accurately aligned with the thermal imaging device. Because the object is an artificial black body, the emissivity is nearly 1.0 and radiated temperature will be nearly identical to contact temperature. No correction for emissivity is needed in the measurements.

The FLIR A325 measures the blackbody first. An image of the target is shown in Figure 7.3. The FLIR is set to display the measured temperature at the center of the target. The blackbody controller and the FLIR camera both measure a temperature of 25.00°C at this time. This temperature is valid only at the center of the target. The temperature, as measured by the imager, decreases around the target until it matches the background. When aligned properly, the blackbody projector provides an accurate means of determining the NEDT of the optical readout system.

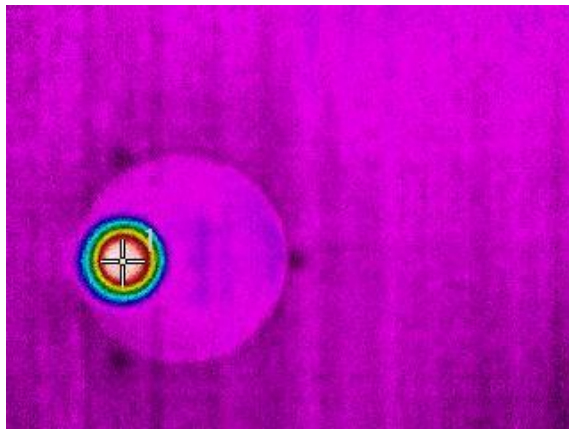


Figure 7.3. The blackbody target at 25.00°C as viewed with the FLIR A325 showing consistency between the value measured by the FLIR and the blackbody controller.

The blackbody is next measured with the optical readout system. Because the detector has no fixed reference position, only relative temperature changes, and not absolute temperature changes, are measured. Figure 7.4 shows two thermograms of the half circle blackbody target. These are obtained by first taking a reference image so that the temperature distribution appears uniform. The blackbody temperature is then increased by 1K. This is repeated for a temperature change of 0.3K. The value for each mirror is the median of a  $3 \times 3$  section offset 6 pixels from the centroid. For a temperature differential of 1K, the target shape is well-defined as shown in Figure 7.4 a. For a 0.3K temperature differential, the target shape is poorly defined as shown in Figure 7.4 b. These results are subjective. A quantifiable method is needed to determine the NEDT value of the thermal imaging system.

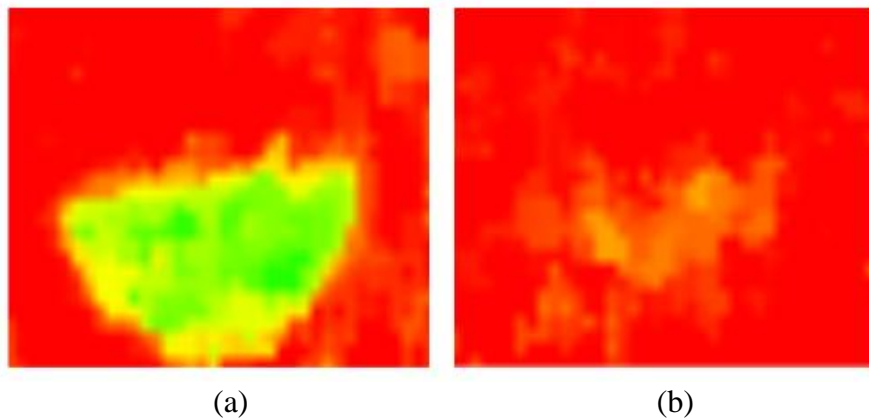


Figure 7.4. Thermograms of blackbody target at known temperature differentials to characterize the measurement resolution: (a) the target is well defined with temperature change of 1K; and (b) the target is visible but more difficult to discern from the background with a temperature change of 0.3K

## 7.2 Procedure for Calculating Noise and NEDT

The noise and NEDT of the system can be quantifiably calculated using the following technique. A data cube of 128 temporal thermograms is captured in succession as represented in Figure 7.5. A single frame has only the vertical and horizontal spatial components. The temporal dimension is added by stacking consecutive frames. The procedure assumes that the scene is uniform spatially and temporally and that the frames are taken in a short period of time. Because the scene is assumed to be uniform, a section of thermogram on the blackbody target is selected.

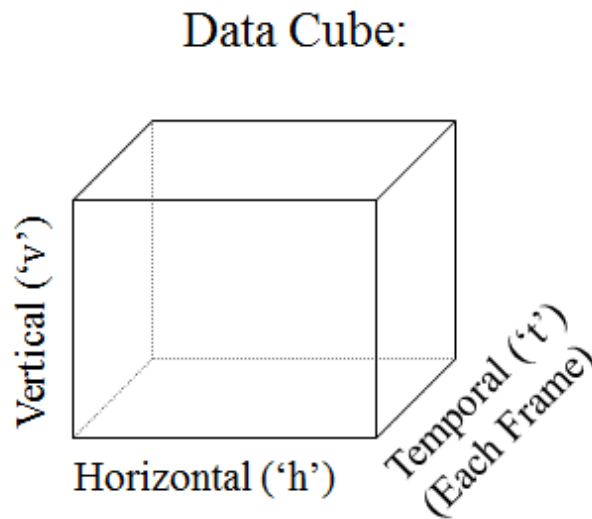


Figure 7.5. Image data cube with vertical and horizontal spatial dimensions and a temporal dimension.

There are two primary components of noise: temporal and spatial. These noise values are measured in the same units as detector output. In the case of the optomechanical sensor, noise is in units of nm for the height changes. Temporal noise is a measure of the variance in time independent of position. It is calculated by finding the standard deviation at each  $x$ - $y$  position for all time  $t$ . The temporal noise is the median of all the standard deviations. This is shown in Figure 7.6.

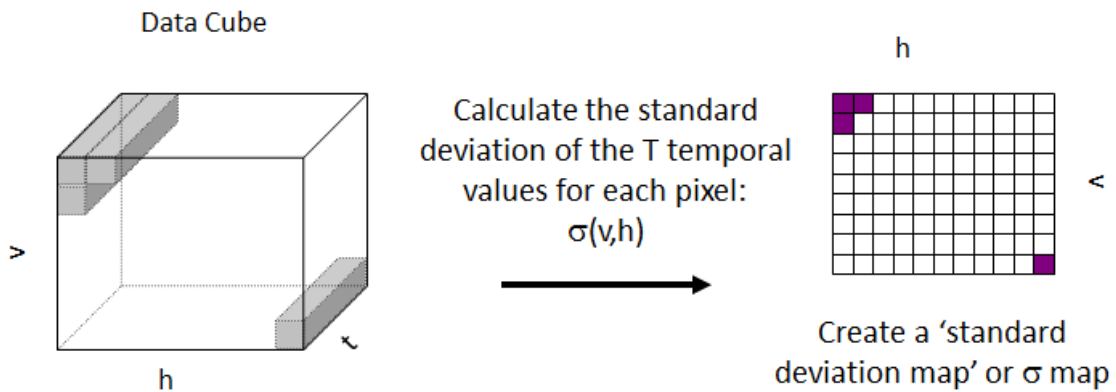


Figure 7.6. Temporal noise as calculated from a data cube by taking the standard deviation at each spatial location across time.

Spatial noise is a measure of the variance in position independent of time. The standard deviation of each frame is calculated. The spatial noise is then the median of the standard deviations for all the frames. This is described visually in Figure 7.7.

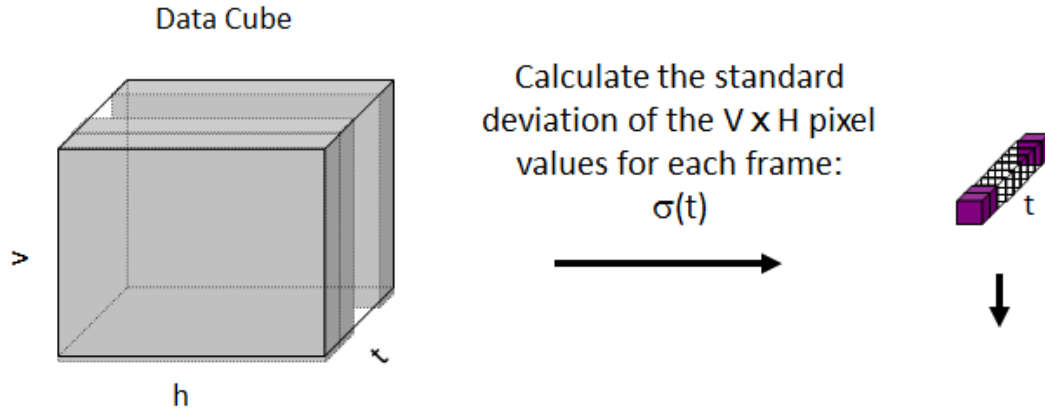


Figure 7.7. Spatial noise as calculated from a data cube by taking the standard deviation of each spatially uniform frame in time.

The total noise is equal to the sum of the squares of temporal and spatial noise or

$$Total\ Noise = \sqrt{Temporal\ Noise^2 + Spatial\ Noise^2}. \quad (7.1)$$

Noise can be broken down even further into base components using a 3D noise procedure. 3D noise is a method of measuring noise that captures all the spatial-temporal behavior of sensor noise (Holst, 1993). The 3D noise method is used to identify which factors contribute most to noise so corrections can be made if possible. The specifics of these calculations are described in Appendix B. Descriptions of these components and possible causes are presented in Table 7.1. The spatial noise is also equal to the sum of the squares of the individual spatial components of the 3D noise. The temporal noise is equal to the sum of the squares of the individual temporal components of the 3D noise. Total noise is calculated as the sum of the squares of the 3D temporal and spatial noise.

Table 7.1. 3D noise components of a data cube used to identify potential sources of noise.

Noise	Component	Potential Source
S	Mean of all components	-
$\sigma_v$	Fixed row noise (horizontal lines)	Detector nonuniformity, 1/f noise
$\sigma_h$	Fixed column noise (vertical lines)	Detector nonuniformity, scan effects
$\sigma_t$	Frame to frame noise or bounce ("flicker")	Frame processing
$\sigma_{th}$	Temporal column bounce ("rain")	Scan effects, read out electronics
$\sigma_{tv}$	Temporal row bounce ("streaking")	Line processing, 1/f noise, readout noise
$\sigma_{vh}$	Random temporal independent spatial noise, FPN	Pixel processing, detector nonuniformity, fixed pattern noise
$\sigma_{tvh}$	Random spatio-temporal noise	Detector temporal noise

The Responsivity is equal to the measured phase difference between the two cubes divided by the known temperature difference, or

$$\text{Responsivity} = \frac{\text{median of warmer cube} - \text{median of cooler cube}}{\text{temperature of warmer cube} - \text{temperature of cooler cube}} \quad (7.2)$$

The temperature associated with each cube is determined by the blackbody temperature. The median value of each cube quantifies the response at the temperature. The expected responsivity is 2.4nm/K. NEDT in units of mK is equal to the total noise divided by the responsivity or

$$NEDT = \frac{\text{Total Noise}}{\text{Responsivity}} \quad (7.3)$$

### 7.3 Noise Results from Optical Flat Measurements

The optical readout is first tested with an optical flat. This will determine the noise introduced by the optical readout system independent of the detector and processing. The system with the optical flat in place of the LWIR lens is shown in Figure 7.8.

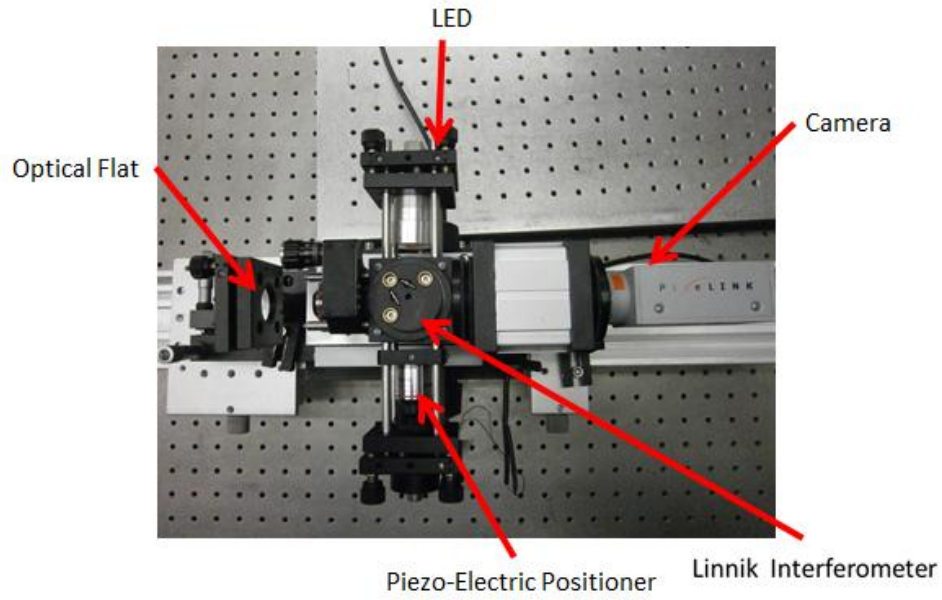


Figure 7.8. Readout system with optical flat in place of the MEMS detector for characterization of temporal and spatial noise of the optical readout system

128 double exposed phase maps are gathered in rapid succession with 1-5 averages per phase step for temporal noise reduction. Each measurement frame is spatially filtered with a  $3 \times 3$  median algorithm and normalized to zero.

The 3D noise results are shown in Table 7.2. All noise components improve with an increasing number of averages. The benefits of averaging are reduced with each additional average. The spatial noise is comparable to the results in Table 4.3 with each displaying a spatial noise of 0.13nm with 5 averages per phase step. Fixed row noise and fixed column noise are consistently low. The random temporal independent spatial noise term is consistently the greatest contributor to spatial noise. This is due to the uncertainty from the camera and piezo in the phase stepping technique.

Table 7.2. 3D noise components of the optical readout system as calculated from holographic measurements of an optical flat.

Number of Averages	1	2	3	4	5
Fixed Column Noise (nm)	0.09	0.06	0.08	0.03	0.02
Frame to Frame Bounce (nm)	0.21	0.15	0.10	0.08	0.07
Temporal Column Bounce (nm)	0.16	0.09	0.09	0.06	0.04
Random Temporal (nm)	1.17	0.26	0.20	0.17	0.15
Temporal Row Bounce (nm)	0.44	0.08	0.07	0.05	0.05
Fixed Row Noise (nm)	0.10	0.04	0.05	0.03	0.03
Random Spatial (nm)	0.33	0.21	0.20	0.15	0.13
Spatial Noise (nm)	0.36	0.22	0.22	0.15	0.13
Temporal Noise (nm)	1.28	0.32	0.25	0.20	0.17
Total Noise (nm)	1.33	0.40	0.33	0.25	0.22

The temporal noise effects contribute more to the overall noise levels. The frame to frame temporal noise is artificially reduced by the normalization of each frame to zero. Temporal column bounce and temporal row bounce are consistently low after averaging. The random temporal noise component is the greatest contributor to total noise and is again due to the limits on uncertainty of the phase stepping technique. Based on the presented results, 4-5 averages are needed to achieve the target noise value of 0.24nm. Additional spatial and temporal filtering will reduce noise further.

#### 7.4 Noise Results for Measurements without Thermal Loading

The detector is measured by the interferometric optical readout system with no thermal loading to characterize the uncertainty introduced by the imaging algorithm. The mirror centroids are first located using the image segmentation algorithm. The reference image is taken on a flat surface at room temperature. No thermal loading is applied at the

scene after the reference image has been captured. The optical phase change at each mirror is measured as a median 6 pixels away from the centroid. 128 thermograms are collected and normalized to zero. Each thermogram has 38×38 pixels.

The first trial is conducted by extracting a single point offset by 6 pixels from the median on each mirror in the array. The results are provided in Table 7.3.

Table 7.3. 3D noise measurements as calculated from a data cube of thermograms produced by the algorithm with a single value offset 6 pixels from the centroid representing each mirror and no thermal-loading after the capture of the reference phase map.

Number of Averages	1	2	3	4
Fixed Column Noise (nm)	0.14	0.14	0.10	0.10
Frame to Frame Bounce (nm)	0.02	0.02	0.02	0.01
Temporal Column Bounce (nm)	0.19	0.19	0.15	0.13
Random Temporal (nm)	0.82	0.83	0.64	0.42
Temporal Row Bounce (nm)	0.22	0.19	0.14	0.10
Fixed Row Noise (nm)	0.18	0.13	0.09	0.07
Random Spatial (nm)	0.70	0.64	0.53	0.36
Spatial Noise (nm)	0.74	0.67	0.54	0.38
Temporal Noise (nm)	0.88	0.87	0.67	0.45
Total Noise (nm)	1.14	1.10	0.86	0.59

Without a median, the height measurement is vulnerable to outliers. As a result, both spatial noise and temporal noise are high. Because temporal averaging reduces noise in the optical phase measurement, each additional average significantly reduces total noise of the algorithm output. A large number of averages can potentially reduce noise to a low enough value without a median, but at the expense of frame rate.

The next trial is conducted under the same conditions but with the 3×3 median offset 6 pixels from the centroid representing each mirror. The results are provided in Table 7.4.

Table 7.4. 3D noise measurements as calculated from a data cube of thermograms produced by the imaging algorithm with the median value of a 3×3 region offset 6 pixels from the centroid representing each mirror and no thermal loading after the capture of the reference phase map.

Number of Averages	1	2	3	4
Fixed Column Noise (nm)	0.05	0.05	0.05	0.04
Frame to Frame Bounce (nm)	0.01	0.01	0.01	0.01
Temporal Column Bounce (nm)	0.10	0.10	0.09	0.07
Random Temporal (nm)	0.45	0.33	0.35	0.29
Temporal Row Bounce (nm)	0.13	0.10	0.09	0.11
Fixed Row Noise (nm)	0.10	0.04	0.05	0.08
Random Spatial (nm)	0.34	0.25	0.26	0.22
Spatial Noise (nm)	0.36	0.26	0.27	0.23
Temporal Noise (nm)	0.48	0.36	0.37	0.32
Total Noise (nm)	0.60	0.44	0.46	0.40

The median significantly lowers spatial noise and temporal noise. Spatial noise factors are lower than the temporal noise factors. This is due to the double exposure holography correcting for spatial non-uniformities of the array. Temporal noise remains high partially due to the temporal uncertainty of the phase-stepper. The averaging does not provide significant reduction in noise beyond two averages per phase step.

The detector is also measured as the result of a 5×5 median offset 6 pixels from the centroid. The results are presented in Table 7.5.

Table 7.5. 3D noise measurements as calculated from a data cube of thermograms produced by the imaging algorithm with the median of a 5×5 region offset 6 pixels from the centroid representing each mirror in the array and no thermal loading after the capture of the reference image.

Number of Averages	1	2	3	4
Fixed Column Noise (nm)	0.05	0.07	0.04	0.06
Frame to Frame Bounce (nm)	0.01	0.01	0.01	0.01
Temporal Column Bounce (nm)	0.10	0.09	0.08	0.08
Random Temporal (nm)	0.33	0.25	0.26	0.18
Temporal Row Bounce (nm)	0.12	0.12	0.11	0.10
Fixed Row Noise (nm)	0.08	0.10	0.08	0.09
Random Spatial (nm)	0.26	0.20	0.20	0.15
Spatial Noise (nm)	0.28	0.23	0.22	0.18
Temporal Noise (nm)	0.37	0.29	0.30	0.22
Total Noise (nm)	0.46	0.37	0.37	0.29

This group of measurements provides the best noise results with 0.29nm total noise after 4 averages. This is still greater than the target noise of 0.24nm. Temporal noise is still a larger contributor to total noise than spatial noise. Increasing the median size will reduce noise even further. A larger median area, however, will decrease responsivity by including the less responsive pixels of each mirror that are located further away from the tip.

Spatial and temporal noise increases from the optical flat measurements to the measurements of the detector. This suggests that the selection of a single median value to represent each pixel propagates the uncertainty of the phase-stepping interferometer's holographic measurements.

## 7.5 NEDT Results

The NEDT is calculated by first measuring the blackbody projector target at three temperatures and then employing the data cube method. The data cubes measured at the highest and lowest temperatures are used to calculate the responsivity of the detector. Noise is calculated with the data cube measured at the intermediate temperature using the methods discussed previously. Each thermogram is an 18×14 section that includes only a uniform section of the blackbody target. The median of a 5×5 region located 6 pixels from the centroid is the mirror response value.

The first set thermograms are measured at uniform blackbody temperatures of 20°C, 21°C, and 22°C. Results are presented in Table 7.6.

Table 7.6. NEDT results as calculated from data cubes of thermograms produced by the imaging algorithm for uniform thermal loading of 20°C, 21°C and 22°C.

Number of Averages	1	2	3	4
Fixed Column Noise (nm)	0.06	0.09	0.05	0.05
Frame to Frame Bounce (nm)	0.12	0.12	0.12	0.14
Temporal Column Bounce (nm)	0.10	0.12	0.12	0.09
Random Temporal (nm)	0.29	0.28	0.23	0.20
Temporal Row Bounce (nm)	0.10	0.09	0.07	0.08
Fixed Row Noise (nm)	0.07	0.05	0.05	0.06
Random Spatial (nm)	0.24	0.21	0.18	0.16
Spatial Noise (nm)	0.25	0.24	0.20	0.18
Temporal Noise (nm)	0.34	0.34	0.28	0.27
Total Noise (nm)	0.43	0.42	0.34	0.33
Responsivity (nm/K)	1.25	1.40	1.43	1.50
NEDT (K)	0.34	0.30	0.24	0.22

Responsivity varies with the number of averages from 1.25nm/K to 1.50nm/K and generally increases with the number of averages. The largest calculated responsivity of 1.50nm/K is 0.9nm/K less than the expected responsivity of 2.40nm/K. Measured spatial noise is consistent with the results presented in Table 7.5. Spatial noise is lower than temporal noise because of the double exposure holography correcting for the spatial uncertainties in the array. Holography reduced the spatial noise in comparison to the temporal noise, but also introduces some uncertainty as demonstrated in the optical flat tests. Temporal noise remains greater than the spatial noise even after temporal averaging.. The responsivity is lower than expected and noise is above the target, so that the lowest calculated NEDT of 0.22K The frame averaging both reduces noise and increases responsivity. Based on these results, further averaging will not lead to significant improvements.

The next set of thermograms is measured at uniform blackbody temperatures of 25°C, 30°C, and 35°C. All other parameters and procedures are the same as the previous tests. Results are presented in Table 7.7. Responsivity is more consistent and remains at a value on the order of 1.6nm/K for all 4 trials. Spatial noise for all trials is greater than the previous set of experiments. Unlike the previous trials, spatial noise is shown to be a larger contributor to total noise than the temporal noise. The lowest calculated NEDT is 0.27K.

The spatial noise and temporal noise results in both sets of measurements are greater than those presented in Table 7.5 for measurements of mirrors with no thermal loading. The spatial and temporal noise increases at higher temperature differentials. This

shows that the algorithm is not robust enough to provide consistent results as the mirrors of the array tilt with temperature variations. Additionally, random spatial noise and temporal noise are consistently the largest contributors to total noise in all tests. These contributions are high due to the noise in the optical phase measurement negatively impacting the algorithms ability to calculate a consistent value spatially and temporally for uniform temperature excitation.

Table 7.7. NEDT results as calculated from data cubes of thermograms produced by imaging algorithm for uniform thermal loading of 25°C, 30°C and 35°C.

Number of Averages	1	2	3	4
Fixed Column Noise (nm)	0.13	0.09	0.09	0.09
Frame to Frame Bounce (nm)	0.13	0.19	0.12	0.11
Temporal Column Bounce (nm)	0.16	0.12	0.12	0.11
Random Temporal (nm)	0.31	0.24	0.25	0.13
Temporal Row Bounce (nm)	0.14	0.12	0.11	0.09
Fixed Row Noise (nm)	0.12	0.10	0.10	0.07
Random Spatial (nm)	0.35	0.26	0.30	0.30
Spatial Noise (nm)	0.39	0.30	0.33	0.32
Temporal Noise (nm)	0.40	0.35	0.33	0.29
Total Noise (nm)	0.56	0.46	0.46	0.43
Responsivity (nm/K)	1.62	1.64	1.65	1.58
NEDT (K)	0.35	0.28	0.28	0.27

## 7.6 Conclusions from Noise and NEDT Characterizations of the System

Mirror response determined as the  $5 \times 5$  median of a region located 6 pixels from the centroid provided the most spatially and temporally consistent measurements of the array. The lowest NEDT achieved from temperature measurements made with the imaging algorithm is 0.22K. As demonstrated in measurements of the optical flat, the noise in height measurements is 0.25nm when 4 averages are taken per phase step. Total noise is greater when the array is as high as 0.43nm when the array is measured. The use of a single median value limits the quality of the images. The median is not consistent temporally or spatially for all pixels experiencing uniform excitation from the scene. This random temporal and spatial noise is due to the noise in the optical phase measurement being propagated when the algorithm selects a value for the mirror. The increase in temporal noise from the use of the algorithm is greater. The double exposure compensates for mirror nonuniformity and as a result, spatial noise is consistently lower than temporal noise.

For all trials, responsivity is lower than the nominal. The responsivity is lowest for the low temperature measurements. The median value of a section of the mirror will not return the maximum response value for that mirror. Alternatively, mirror response determined by the maximum value of a region on the mirror leaves the results vulnerable to outliers and increases noise. Because the mirrors tilt, the  $(x,y)$  location of the mirror tip changes with the temperature differential. The offset from the centroid that is appropriate at one temperature is not appropriate at a different temperature. For this

reason, responsivity, spatial noise, and temporal noise for measurements of mirror response are inconsistent at different temperatures. A new algorithm is needed that will not be impacted as heavily by changing conditions of the mirrors. The responsivity measurements suggest that the detector does not exhibit the nominal responsivity. With responsivity closer to the nominal value of 2.4nm/K or greater, the NEDT of the system will improve. Improvements to the detector that increase responsivity and improvements to the holographic system that reduce noise will lower the NEDT.

## **8 Alternative Imaging Algorithm**

The original algorithm is limited due to the use of a single median value to determine the response of each mirror in the array. As a result, total noise increases and responsivity decreases. This prevents the algorithm from achieving the target NEDT of 100mK. The revised algorithm measures change in slope instead of change in height to improve upon the issues of the original algorithm.

### **8.1 Description of the Alternative Imaging Algorithm**

The revised algorithm is based on the measurement of mirror tilt from the double exposed optical phase map information. This is accomplished by first taking a median value of each column across a pixel to create a 1-dimensional vector of the phase changes across the center of the mirror. The slope of the linear regression through the points of the vector is then calculated. The calculated values of the array are slopes in terms of radians/pixel. Responsivity is in terms of change in slope per change in K. MATLAB code for the new algorithm is presented in Appendix C. The code has not been implemented into LaserView. Currently image acquisition is performed with LaserView and the algorithm is applied in post processing rather than in real-time as the previous algorithm.

The measurement of slope for the determination of individual mirror response has several benefits. Due to piezo non-linearity and environmental effects, the mean value of the entire optical phase map drifts temporally while the spatial relationship between

pixels remains constant. In the original algorithm, the temporal drift is partially corrected in post processing by establishing a dc offset. The slope of each mirror is independent of the temporal drift. As a result, the flickering observed in the original thermogram streams is no longer present.

The measurement of mirror response with the new algorithm is not dependent upon a single pixel. Instead, a slope is fit through the median of pixels across the mirror. Because mirror response is measured across the entire mirror instead of at the tip, the change in mirror tip location corresponding to tilt will not impact the results. Measured responsivity is independent of temperature change. Additionally, the measurement does not drift temporally and a DC offset does not need to be specified.

## **8.2 Alternative Algorithm Results**

The new algorithm is tested on an array with uniform temperature excitation so that the response of each pixel will be uniform both temporally and spatially. Figure 8.1 shows the linear fit to the optical phase data of a single mirror with a correlation coefficient of 0.97. Although the data is not smooth, the correlation coefficients for most mirror fits in the array are consistently lower than 0.95, as demonstrated in Figure 8.2. Values closest to 1.00 signify the highest quality linear fits. The mean of the histogram is 0.97 with standard deviation of 0.13. This signifies that the regressions across the mirrors are consistently linear.

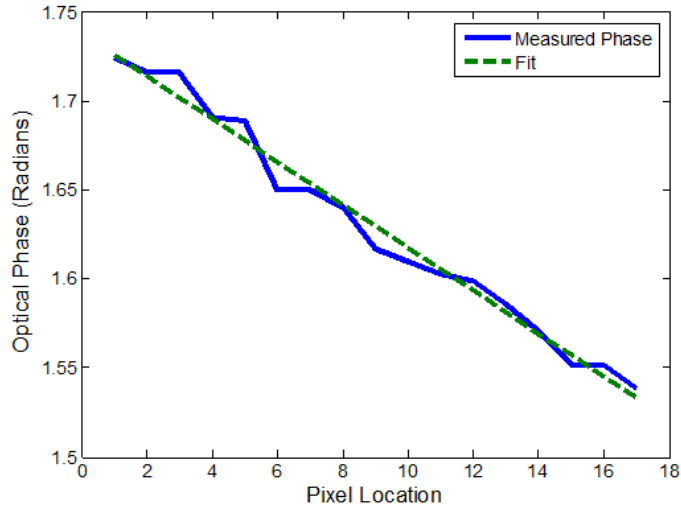


Figure 8.1. The linear fit of the measured double exposed optical phase values across a tilted mirror with a slope of 0.011 rad/pixel and a correlation coefficient of 0.97 demonstrating the linearity

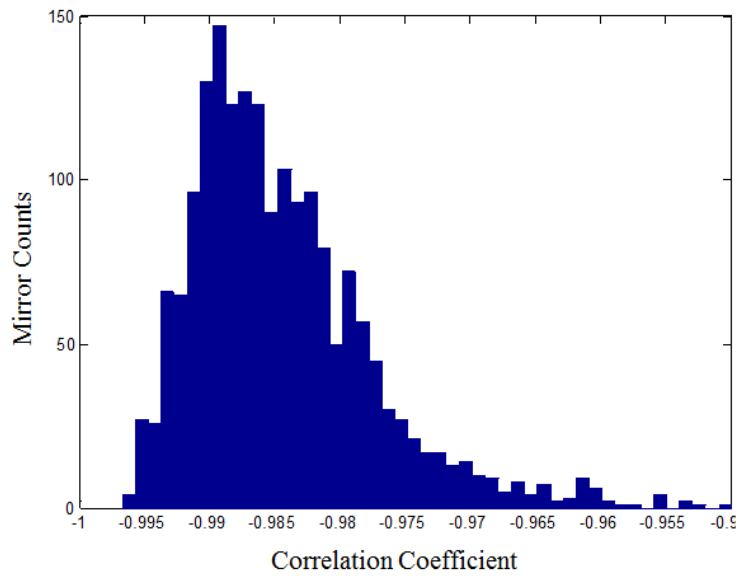


Figure 8.2. Histogram showing the distribution of correlation coefficients for linear regressions of slope of each mirror in the array demonstrating that the slope of the mirrors is consistently linear.

Figure 8.3 is an example of a mirror phase map with outliers. The slope of this fit is 0.010 rad/pixel while the slope of the fit in Figure 8.1 is 0.011 rad/pixel. The difference in slope corresponds to a difference in height change at the tip of 0.84nm, a value much greater than the target uncertainty of 0.24nm. This example demonstrates that even with a correlation coefficient better than 0.95, because of the small number of pixels, deviations from linearity in measurements of mirror tilt heavily impact the slope values associated with each mirror.

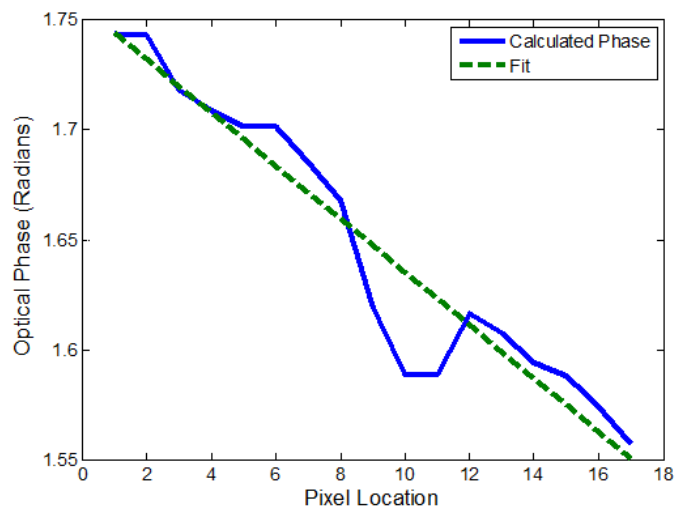


Figure 8.3. Linear fit to measured phase across a mirror with outlier phase values that skew the linear regression so that the slope is 0.010 rad/pixel instead of 0.011 rad/pixel

3D noise is calculated from a data cube of the same uniform scene of a human hand to quantify the spatial and temporal variations in measured slope. For each mirror,

the noise in slope, or phase per pixel, is multiplied by the number of pixels so that the results are in terms of phase. The phase is then converted to height so that the results can be compared directly with the noise results of the original algorithm. The results are presented in Table 8.1. Because the slope is independent of the temporal drift, temporal noise from frame to frame bounce is the lowest contributor to noise even with no DC offset. Like the results with the original algorithm, random spatial noise and random temporal noise are the largest contributors to total noise. These contributions are high due to the noise in the optical phase measurement negatively impacting the algorithms ability to calculate a consistent value spatially and temporally for uniform temperature excitation.

Table 8.1. 3D noise results as calculated from a data cube of thermograms of a uniform scene of a human hand using the mirror slope algorithm

<b>3D Noise Component</b>	
<b>Fixed Column Noise</b>	0.06nm
<b>Frame to Frame Bounce</b>	0.02nm
<b>Temporal Column Bounce</b>	0.09nm
<b>Random Temporal</b>	0.27nm
<b>Temporal Row Bounce</b>	0.18nm
<b>Fixed Row Noise</b>	0.18nm
<b>Random Spatial</b>	0.23nm
<b>Spatial Noise</b>	0.29nm
<b>Temporal Noise</b>	0.34nm
<b>Total Noise</b>	0.43nm

The noise values for a uniform high response are compared to the noise values from the detector measured with a uniform room temperature response. The results are presented in Table 8.2. The noise contributions of each 3D noise component are

consistent with the results presented in Table 8.1. Unlike the original algorithm, the noise of measurements made with the new algorithm is independent of temperature change.

Table 8.2. 3D noise results as calculated from a data cube of thermograms of a uniform scene at room temperature using the mirror slope algorithm.

3D Noise Component	
Fixed Column Noise	0.03nm
Frame to Frame Bounce	0.01nm
Temporal Column Bounce	0.06nm
Random Temporal	0.26nm
Temporal Row Bounce	0.15nm
Fixed Row Noise	0.14nm
Random Spatial	0.20nm
Spatial Noise	0.24nm
Temporal Noise	0.31nm
Total Noise	0.39nm

The algorithm is tested on data cubes measured with known temperature response from the blackbody so that responsivity and NEDT can be calculated. The data cubes are measured at uniform blackbody temperatures of 25°C, 30°C, and 35°C. Figure 8.4 shows the slope of the mirror tilt for 25°C excitation. The slope of the mirror at 25°C is 0.0047 rad/pixel. Figure 8.5 shows the slope of the mirror tilt at 35°C excitation for the same mirror. Both the slope and intercept of the linear fit shift with the temperature change. The slope of the mirror at 35°C is 0.0136 rad/pixel. This corresponds to a height change at the mirror tip of 0.7nm/K. This is significantly less than the responsivity of 1.5nm/K as measured with the original algorithm and the nominal responsivity of 2.4nm/K.

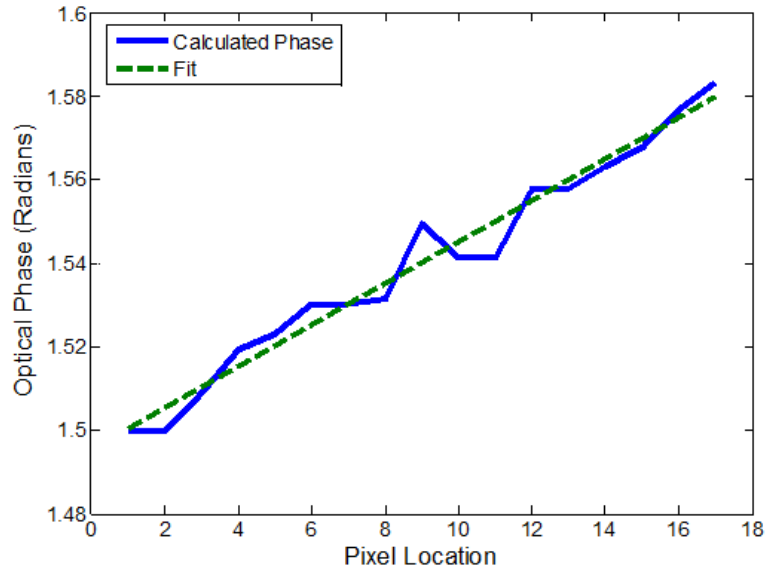


Figure 8.4. The optical phase across a single pixel for uniform scene temperature of 25°C with a slope of 0.0047rad/pixel.

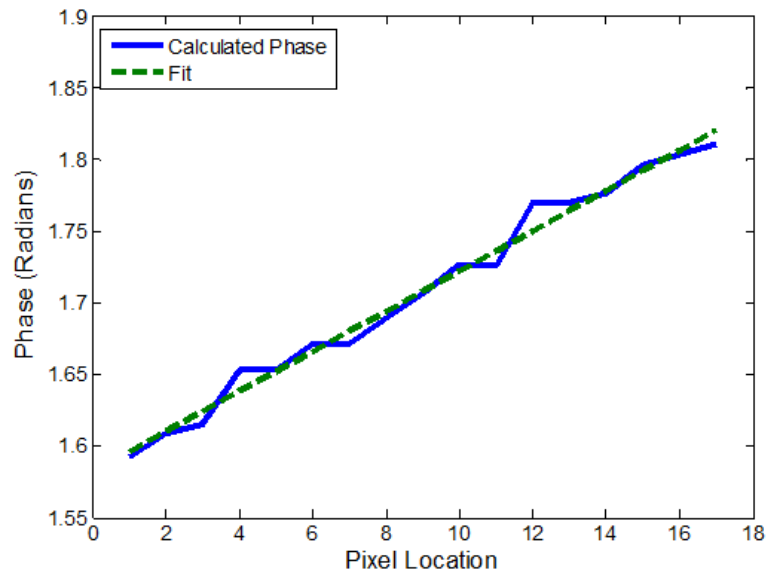


Figure 8.5. The optical phase across a single mirror for uniform scene temperature of 35°C with a slope of 0.0136rad/pixel.

Results of the NEDT calculation are presented in Table 8.3. Each contributor to 3D noise is consistent with the results for other uniform responses. This further establishes the independence of noise and temperature with this algorithm. Additionally, responsivity between 25°C and 30°C, between 30°C and 35°C, and between 25°C and 35°C are all equal to 0.77nm/K. Responsivity is also independent of temperature. With the calculated responsivity and noise values, however, NEDT is 0.55K. The responsivity of the array as measured with the new algorithm is half that of the original algorithm and a quarter of the expected value of 2.4nm/K. No temporal averaging or spatial filtering has been applied to the results. Further optimizations of the phase stepping measurements can potentially reduce noise further while improvements to the MEMS detector can increase responsivity.

Table 8.3. NEDT results for data cubes of thermograms of uniform scenes at 25°C, 30°C, and 35°C using the mirror slope algorithm and no temporal averaging.

<b>3D Noise Component</b>	
<b>Fixed Column Noise</b>	0.10nm
<b>Frame to Frame Bounce</b>	0.08nm
<b>Temporal Column Bounce</b>	0.14nm
<b>Random Temporal</b>	0.27nm
<b>Temporal Row Bounce</b>	0.11nm
<b>Fixed Row Noise</b>	0.09nm
<b>Random Spatial</b>	0.24nm
<b>Spatial Noise</b>	0.28nm
<b>Temporal Noise</b>	0.32nm
<b>Total Noise</b>	0.43nm
<b>Responsivity</b>	0.77nm/K
<b>NEDT</b>	0.56K

The experiment is repeated with temporal averaging of 4 frames per phase step to verify that reduction in measured phase map noise will improve the noise of the alternative infrared imaging algorithm. The results are presented in Table 8.4. As a result of the temporal averaging, the magnitude of all noise contributors drops. The drop in total noise from 0.43nm to 0.21nm is a reduction of more than half from the results with no temporal averaging. Measured responsivity is lower so that the NEDT is reduced to only 0.35K. This still does not surpass the NEDT of the original algorithm.

Table 8.4. NEDT results for data cubes of thermograms of uniform scenes at 25°C, 30°C, and 35°C using the mirror slope algorithm and 4 frames average per phase step.

3D Noise Component	
Fixed Column Noise	0.03nm
Frame to Frame Bounce	0.07nm
Temporal Column Bounce	0.05nm
Random Temporal	0.13nm
Temporal Row Bounce	0.05nm
Fixed Row Noise	0.04nm
Random Spatial	0.10nm
Spatial Noise	0.13nm
Temporal Noise	0.18nm
Total Noise	0.21nm
Responsivity	0.60nm/K
NEDT	0.35K

### 8.3 Alternative Algorithm Conclusions

A new algorithm has been tested for the determination of each mirror's response with temperature. This involves the calculation of mirror tilt through a linear regression. This removes temporal frame drifting due to environmental conditions. Noise and

responsivity as measured by this algorithm are independent of changing conditions as the mirror tilts with temperature.

Measurements of the detector through the algorithm have an NEDT value of 0.35K. The accurate linear fit to mirror tilt is heavily dependent upon the ability to achieve low noise double exposed optical phase measurements of each mirror's surface. Because of the small number of points that characterize the cross section of the mirror's surface, the linear regression is vulnerable to even small outliers. As demonstrated, phase values that deviate from linearity will significantly impact the calculated slope. Temporal averaging at each phase step reduces the number of values on the mirror that deviate from linearity. Further noise reduction in the optical phase measurements will significantly improve the noise results of the algorithm and lower the NEDT.

## 9 Conclusions and Recommendations for Future Work

An interferometric optical readout system has been developed for real-time holographic measurements of the response of a MEMS infrared imaging detector. The use of a compensation window is needed to overcome the optical path length difference introduced by the optical window of the vacuum sealed package.

The MEMS detector is comprised of an array of micro mirrors that tilt as a function of temperature from the scene. The nominal rate of tilt is 2.4nm/K. To achieve an NEDT of 100mK, noise in height measurements needs to be below 0.24nm. Measurements of a NIST traceable calibration standard with 100nm step demonstrate the ability of phase stepping interferometry to make accurate, low-noise, and real-time measurements with repeatability below 0.13nm after temporal averaging of frames. 4-5 temporal averages per phase step provide nearly the maximum benefit at the expense of frame rate.

The MEMS detector is held at the focal point of a long wave infrared imaging lens so that the mirrors in the array will respond to temperatures at the scene. The developed interferometric optical readout system is a Linnik phase stepping interferometer. The interferometer measures height maps of the detector's focal plane array. The LaserView software developed internally by WPI's CHSLT lab is used to control image acquisition and phase stepping. It also calculates double exposed optical phase maps from the interferogram stream. The use of double exposure creates a uniform scene so that only changes in mirror height are displayed. The mirror response is visible

in the optical phase map. While the phase maps remain constant spatially, piezo-non-linearity leads to temporal floating.

Two different algorithms have been developed to extract a value for each mirror from the optical phase map. The first extracts a median value offset from the mirror centroid. This algorithm has been used to create real-time thermograms. These thermograms are pixelated due to the small field-of-view of the optical readout system. Nevertheless, the measured temperature distributions are comparable to a commercially available FLIR infrared imaging camera with NEDT of 0.07K and display at near real-time rates.

A differential blackbody projector is used to measure uniform scenes at known temperatures. Temporal and spatial noise contributions are calculated with the data cube technique. The responsivity of the array as measured with the algorithm with 4 temporal averages per phase step is 1.5nm/K and the lowest NEDT is 0.22K. The algorithm does not adapt to changes in mirror pixel distribution as the mirror tilts with temperature change. As a result, noise, responsivity, and NEDT for the same algorithm input parameters vary with scene temperatures.

Furthermore, a second algorithm measures mirror response as the slope of a linear fit corresponding to the tilt of each mirror. Measurements from this algorithm are not impacted by the temporal drift. Additionally, the results for noise, responsivity, and NEDT are independent of temperature. Because of the small number of data points measured on each mirror, the slope of the linear fit changes significantly with values that deviate from linearity. The responsivity of the array as measured with this algorithm is

0.75nm/K and the NEDT is 0.35K. Despite the performance, the algorithm is more robust and results will not vary with conditions at the scene.

Although double exposure lowers spatial noise in comparison to temporal noise, the temporal and spatial uncertainty in the measured optical phase maps propagates when either of the two algorithms is applied to extract a value for each mirror. The propagation is more substantial with the slope measurement algorithm. Results from both algorithms will improve if uncertainty in the height measurements can be reduced. The uncertainty can be improved in a number of ways including the use of piezo-electric transducer with closed loop feedback and higher repeatability and the use of a camera with larger pixel well size. In addition, the development of alternative algorithms for height map calculations can also potentially reduce noise. Phase stepping algorithms that use more than 4 phase steps have greater repeatability but at the expense of frame rate. Alternative real-time holographic microscopy techniques need to also be considered. Because responsivity is lower than expected, the noise of the holographic measurements needs to be even lower to compensate. A MEMS detector with higher responsivity will improve the system's NEDT by increasing the gap between the interferometer's measurement resolution and the height change of the mirrors in the array.

A new MEMS detector is in development specifically for use with the first algorithm. The mirrors in the array only appear to move out of plane instead of tilting. As a result, the response is uniform across the entire mirror. A height change value can then be extracted reliably at the mirror centroid regardless of the response. The mirrors in every other column of the array act as fixed reference surfaces. If the height change of a

mirror is always compared to the height of a fixed mirror, absolute measurements of height change can be made and temporal drifting will be eliminated. The responsivity of the first packaged version of this detector needs to be improved in order to provide meaningful results. Additionally, because the mirror displacement is only out-of-plane, the revised algorithm that measures slope is not valid.

A phase-stepping interferometer can measure real-time holographic changes across the mirror array of the MEMS detector. Double-exposure holography eliminates the noise due to spatial inconsistencies in the array construction. Uncertainty in the holographic measurements made with the phase shifting interferometer propagates when the algorithms extract a value for each mirror. The noise combined with the low responsivity of the detector limits the NEDT results. If noise in the holographic measurement system is reduced below noise introduced by spatial inconsistencies in the array and if the responsivity of the array is increased, then an NEDT of 100mK or better can be achieved.

Future work involving the optimization of the new detector and the first algorithm has more potential than the development of the slope algorithm in conjunction with the existing detector. An increase in detector responsivity will lead to a proportional improvement in NEDT without impacting the measurement noise. Thus, future detector designs should have a larger mirror displacement per change in temperature. Although thermograms produced by the slope algorithm are temporally consistent, the measurement noise is greater. Additionally, the calculation is computationally more intensive and requires more pixels per mirror. To improve spatial resolution of the

thermograms, a larger field of view of the interferometric system is needed. The larger field of view will decrease the number of pixels per mirror so that the slope algorithm will not be able to produce a valid regression. On the other hand, if the pixel motion is strictly out-of-plane, then only a small number of pixels are needed to calculate the median displacement for a mirror. The field of view can be increased while still allowing for accurate height measurements with the algorithm. Temporal consistency can be improved with the new detector design by adjusting the original algorithm to track the relative height differentials between fixed reference pixels and the pixels that respond to temperature change. With these changes to the algorithm and detector, along with noise reduction in the measurement system, it will be possible to achieve improved NEDT values in future iterations of the interferometric readout system.

## 10 References

- Bogue, R., 2003, "US company launches first MEMS based IR detector array," *Sens. Rev.*, 23(4): 299-301, 2003.
- Choi, J., Yamaguchi, J., Morales, S., Horowitz, R., Zhao, Y., and Majurndar, A., "Design and control of a thermal stabilizing system for a MEMS optomechanical uncooled infrared imaging cameras," *Sens. and Act.*, 104:132-142, 2003.
- Cloud, G., *Optical Methods of Engineering Analysis*, Cambridge University Press, 1995.
- Dobrev, I., Balboa, M., and Fossett, R. "MEMS for Real-Time Imaging," Major Qualifying Project, Mechanical Engineering Department, Worcester Polytechnic Institute, 2009.
- Dobrev, I., Balboa, M., Fossett, R., Furlong C., and Harrington, E., "MEMS for real-time infrared imaging," *Proc. SEM, MEMS and nanotechnology*, 4:119-125, 2011.
- Dong, D., Qingchuan, Z., Dapeng, C., Liang, P., Zheyang, G., Weibing, W., Zhihui, D., and Xiaoping, W., "An uncooled optically readable infrared imaging detector," *Sens. and Act.*, 133: 236-242, 2007.
- Duan, Z., Zhang, Q., Wu, X., Pan, L., Chen, D., Wang, W., and Guo, Z., "Uncooled optically readable bimaterial micro-cantilever infrared imaging device," *Chin. Phys. Lett.*, 20(12): 2130-2132, 2003.
- Dushkina, N., "Light Sources." Yoshizawa, T., *Handbook of Optical Metrology.*, CRC Press, 3-85, 2009.
- Erdtmann, M., Radhakrishnan, S., Zhang, L., Liu, Y., Emelie, P., and Salerno, J., "Photomechanical imager FPA design for manufacturability," *Proc. SPIE, Infrared technology and applications XXXVI*, Vol. 7660, 2010.
- Erdtmann, M., L. Zhang and G. Jin., "Uncooled dual-band MWIR/LWIR optical readout imager," *Proc. SPIE 6940, 694012*, 2008.
- Furlong, C., "Optoelectronic Holography for Testing Electronic Packaging and MEMS," Osten, W., *Optical Inspection of Microsystems*, CRC Press, 325-350, 2007.
- Furlong, C., and Pryputniewicz, R., "Optoelectronic characterization of shape and deformation of MEMS accelerometers used in transportation applications," *Opt. Eng.*, 42(5): 1223-1231, 2003.

- Hall, P., "Lenses, Prisms, and Mirrors." Yoshizawa, T., *Handbook of Optical Metrology*., CRC Press, 3-85, 2009.
- Hariharan, P., B. Oreb and T. Eiju., "Digital phase-shifting interferometry: a simple error-compensating phase calculation algorithm," *App. Opt.* 26(13): 2504-2506, 1987.
- Harrington, E., *Development of an Optoelectronic Holographic Platform for Otolaryngology Applications*, MS Thesis, Computer Science Department, Worcester Polytechnic Institute, 2009.
- Holst, G., *Testing and Evaluation of Infrared Imaging Systems*, JCD Publishing Co., 1993.
- Hsu, T., *MEMS and Microsystems*, John Wiley and Sons Inc., 2008.
- Incropera, F., Dewitt, D., Bergman, T., and Lavine, A., *Fundamentals of Heat and Mass Transfer Sixth Edition*, John Wiley & Sons, 2007.
- Li, C., Jiao, B., Shi, S., Ye, T., Chen, D., Zhang, Q., Guo, Z., Dong, F., and Wu, X., "A novel MEMS-based focal plane array for infrared imaging," *Front. Electr. Electron. Eng. China*, 2(1): 83-87, 2007.
- Liu, M., Zhao, Y., Dong, L., Yu, X., Liu, X., Hui, M., You, J., and Yi, Y., "Holographic illumination in optical readout focal plane array infrared imaging system," *Opt. Lett.*, 34(22):3547-3549, 2009.
- Marinis, R., "Development and implementation of automated interferometric microscope for study of MEMS inertial sensors," PhD Dissertation, Mechanical Engineering Department, Worcester Polytechnic Institute, 2009.
- Marinis, T., Soucy, J., Lawrence, J., Marinis, R., and Pryputniewicz, R., "Vacuum sealed MEMS package with an optical window," *IEEE, Electronic Components and Technology Conference*, IEEE. 804-810, 2008.
- Miller, J., *Principles of Infrared Technology*, Van Nostrand Reinhold, 1994.
- Nezhadian, S., S. Khalilariya and G. Rezazadeh., "MEMS tuneeling wide range micro thermometer based on bimetallic *cantilever* beam," *Sens. and Trans.*, 91(4):14-23, 2008.
- Osten, W., *Optical Inspection of Microsystems*, CRC Press, 325-350, 2007.
- Hall, P., "Lenses, Prisms, and Mirrors," in Yoshizawa, T., *Handbook of Optical Metrology*, CRC Press, 85-104, 2009.

Page, D., "Interferometry," in Yoshizawa, T., *Handbook of Optical Metrology*, CRC Press, 191-217, 2009.

Physik Instrumente, "P-725.xDD PIFO High-Dynamics Piezo Scanner," On-Line: [http://www.physikinstrumente.com/en/pdf/P725\\_xDD\\_Datasheet.pdf](http://www.physikinstrumente.com/en/pdf/P725_xDD_Datasheet.pdf), 2012a.

Physik Instrumente, "P-810 · P-830 Piezo Actuators for Light and Medium Loads," On-Line: [http://www.physikinstrumente.com/en/pdf/P810\\_Datasheet.pdf](http://www.physikinstrumente.com/en/pdf/P810_Datasheet.pdf), 2012b.

Rodgers, M., *Phase Modulating Interferometry for the Stroboscopic Illumination for Characterization of MEMS*, MS Thesis, Mechanical Engineering Department, Worcester Polytechnic Institute, 2006.

Santa Barbara Infrared, INC., "Education on IR Testing: Test System Components," On-Line: [http://www.sbir.com/PDFs/Education-Technical-Application-Notes/Test\\_System\\_Components\\_1999.pdf](http://www.sbir.com/PDFs/Education-Technical-Application-Notes/Test_System_Components_1999.pdf), 1999.

Suyama, M., "Optoelectronic Sensors," in Yoshizawa, T., *Handbook of Optical Metrology*, CRC Press, 105-131, 2009.

Timoshenko, S., "Analysis of bi-metal thermostats," *J. Opt.Soc. Am.*, 11: 233-255, 1925.

Young, H. and R. Freedman, *University Physics 12th Edition*, Pearson Addison-Wesley, 2008.

## Appendix A: MATLAB code for Infrared Imaging Algorithm

```
function [mirrorvals] = irmask(modu, phase)
    % Inputs are a modulation image and optical phase map
    % Calculate modulation mean and median values
    mean_large = filter2(fspecial('average', [70 70]), modu);
    med_small = medfilt2(modu, [3 3]);
    % Identify pixels of the image that meet threshold requirement
    bw = (med_small * 0.8 > mean_large);
    % Segment image into regions from pixels that meet threshold
    reg = regionprops(bw);
    ims = size(modu);
    imsc = 0.06;
    mirrorvals = zeros(round(ims(1)*imsc), round(ims(2)*imsc));
    imscs = size(mirrorvals);
    mirrorvals(:) = nan;
    s = size(reg{:});
    phasemed = phase;
    s = size(reg{:});
    phasemed = phase;
    for i = 1:s(1)
        blob = reg(i);
        % Check if region size meets requirements
        if ((blob.Area > 75) && (blob.Area < 250))
            y = round(blob.Centroid(2));
            x = round(blob.Centroid(1));
            % Define area on mirror from which the median will be extracted

            region_size = 3;
            l=round((region_size-1)/2);
            p_x = 6;
            p_y = 0;
            ysc = round(y*imsc);
            xsc = round(x*imsc);
            if ((xsc > 0) && (xsc <= imscs(2)) && (ysc > 0) && ...
                (ysc <= imscs(1)) && (x > 0) && (x <= ims(2)) &&
                (y > 0) && (y <= ims(1)))

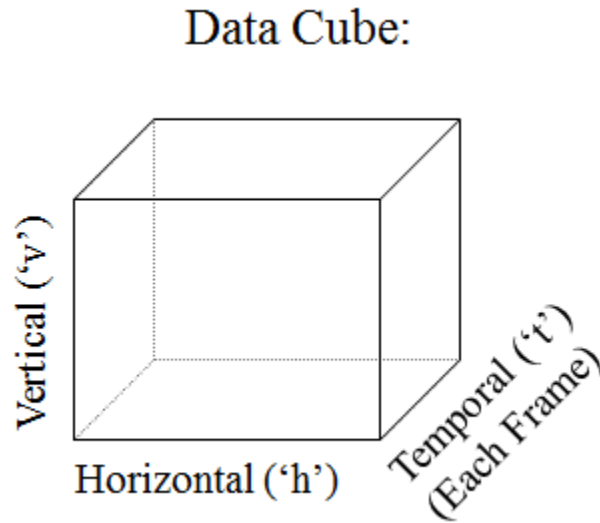
                mirror_area = phasemed((y+p_y)-l:(y+p_y)+l, ...
                    (x+p_x)-l:(x+p_x)+l);

                % Calculate mirror value from median
                val = median(mirror_area);

                % Place mirror value at the centroid location
                mirrorvals(ysc,xsc) = val;
            end
        end
    end
end
```

## Appendix B: 3D Noise Calculations

Create a data cube with  $t$  temporal uniform frames with vertical dimension  $v$  and horizontal dimension  $h$  acquired in a short period of time:

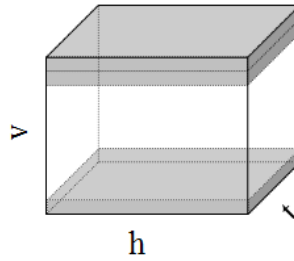


The components of 3D noise components as calculated with this procedure are listed in the following table:

Noise	Component	Potential Source
$S$	Mean of all components	-
$\sigma_v$	Fixed row noise (horizontal lines)	Detector nonuniformity, 1/f noise
$\sigma_h$	Fixed column noise (vertical lines)	Detector nonuniformity, scan effects
$\sigma_t$	Frame to frame noise or bounce ("flicker")	Frame processing
$\sigma_{th}$	Temporal column bounce ("rain")	Scan effects, read out electronics
$\sigma_{tv}$	Temporal row bounce ("streaking")	Line processing, 1/f noise, readout noise
$\sigma_{vh}$	Random temporal independent spatial noise, FPN	Pixel processing, detector nonuniformity, fixed pattern noise
$\sigma_{tvh}$	Random spatio-temporal noise	Detector temporal noise

Calculations must take place in the following order. First take the average value of the data cube  $S$  and subtract the mean from each value so that the new mean of the cube is 0.

Average all  $t \times h$  values in each vertical slice:

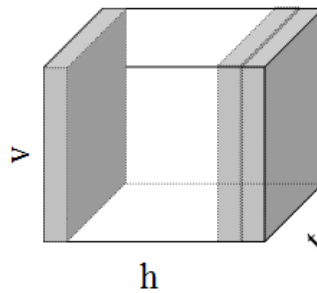


Take the standard deviations of the  $v$  averages for 3D noise component fixed row noise  $\sigma_v$ :

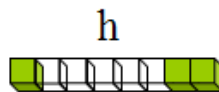


Once  $\sigma_v$  is recorded it is subtracted from every value in the  $t \times h$  vertical slices so that the mean of each slice is 0.

Average all  $t \times v$  values in each horizontal slice:

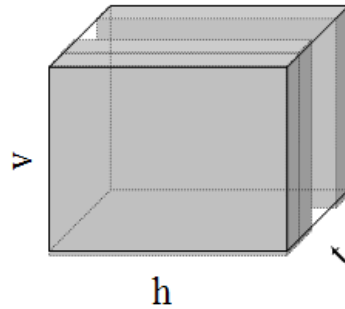


Take the standard deviations of the  $h$  averages for 3D noise component fixed column noise  $\sigma_h$ :

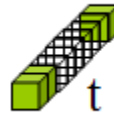


Once  $\sigma_h$  is recorded it is subtracted from every value in the  $t \times v$  horizontal slices so that the mean of each slice is 0.

Average all  $h \times v$  values in each temporal slice:

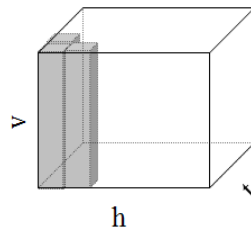


Take the standard deviations of the  $t$  averages for 3D noise component frame to frame bounce  $\sigma_t$ :

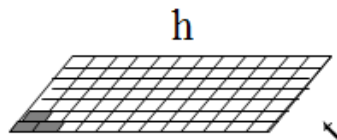


Once  $\sigma_t$  is recorded it is subtracted from every value in the  $h \times v$  temporal slices so that the mean of each slice is 0.

Average all  $v$  values in each vertical column in the  $h \times t$  plane:

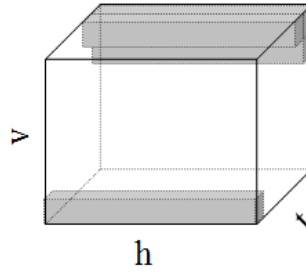


Take the standard deviations of the  $h \times t$  averages for 3D noise component temporal column bounce  $\sigma_{th}$ :

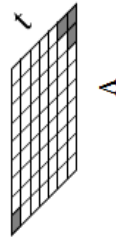


Once  $\sigma_{th}$  is recorded it is subtracted from every value in the  $h \times t$  columns so that the mean of each column is 0.

Average all  $h$  values in each horizontal column in the  $v \times t$  plane:

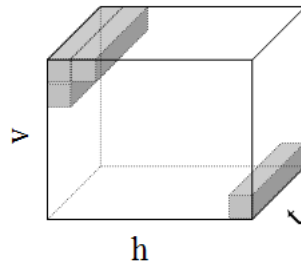


Take the standard deviations of the  $v \times t$  averages for 3D noise component temporal row bounce  $\sigma_{tv}$ :

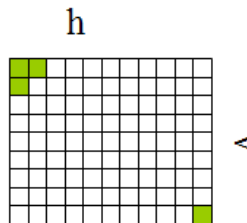


Once  $\sigma_{tv}$  is recorded it is subtracted from every value in the  $v \times t$  columns so that the mean of each column is 0.

Average all  $t$  values in each temporal column in the  $h \times v$  plane:

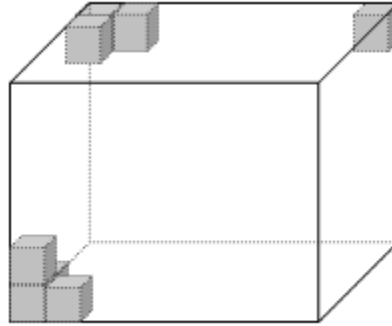


Take the standard deviations of the  $h \times v$  averages for 3D noise component random spatial noise  $\sigma_{vh}$ :



Once  $\sigma_{vh}$  is recorded it is subtracted from every value in the  $h \times v$  columns so that the mean of each column is 0.

The standard deviations of the entire cube is the random spatio-temporal noise  $\sigma_{thv}$ :



The mean value of any row, column, or slice is now 0.

## Appendix C: Alternative Algorithm MATLAB Code

```
function [mirrorvals] = irmask(modu, phase)
    % Inputs are modulation image and phase map
    % Calculate modulation mean and median values
    mean_large = filter2(fspecial('average', [70 70]),modu);
    med_small = medfilt2(modu, [3 3]);
    % Find regions of the image that meet threshold requirement
    bw = (med_small * 0.8 > mean_large);
    % Segment image into regions based on mirror modulation
    reg = regionprops(bw);
    ims = size(modu);
    imsc = 0.06;
    mirrorvals = zeros(round(ims(1)*imsc), round(ims(2)*imsc));
    imscs = size(mirrorvals);
    mirrorvals(:) = nan;
    s = size(reg(:));
    phasemed = phase;
    for i = 1:s(1)
        blob = reg(i);
        % Check if region size meets threshold requirements
        if ((blob.Area > 75) && (blob.Area < 250))
            y = round(blob.Centroid(2)); x = round(blob.Centroid(1));
            % Define area of the mirror
            p_left = 9; p_right = 9;
            p_top = 4;
            p_bottom = 4;
            ysc = round(y*imsc);
            xsc = round(x*imsc);
            if ((xsc > 0) && (xsc <= imscs(2)) && (ysc > 0) && ...
                (ysc <= imscs(1)) && (x > 0) && (x <= ims(2)) && ...
                (y > 0) && (y <= ims(1)))
                if ((y - p_top >= 1) && (y + p_bottom <= ims(1)) && ...
                    (x - p_left >= 1) && (x + p_right <= ims(2)))
                    %Extract area of interest from phase map
                    mirror_area = phasemed(max(1,y - p_top):...
                        min(ims(1), y + p_bottom), max(1,x -p_left):...
                        min(ims(2), x + p_right));
                    %Take median of each column in the mirror
                    twod_mirror_shape = nanmedian(mirror_area);
                    siz = size(twod_mirror_shape);
                    %Filter the vector of the median values
                    twod_mirror_shape_filt = ...
                        medfilt2(twod_mirror_shape,[2 2]);
                    twod_mirror_shape_filt = ...
                        twod_mirror_shape_filt(2:siz(2)-1);
                    % Calculate the components of the linear regression
                    [r,m,b] = ...
                        regression(1:(siz(2)2),twod_mirror_shape_filt);
                    % Set the mirror value to the slope
                    val = -m;
                    % Place mirror values at centroid location
                    mirrorvals(ysc,xsc) = val;
                end ; end; end; end; end;
    end
```